Modelling the effect of geometric uncertainties, clonogen distribution and IMRT interplay effect on tumour control probability

Thesis submitted in accordance with the requirements of the University of Liverpool for the degree of Doctor of Philosophy by

Jothybasu K Selvaraj

September 2013

Abstract

Geometric uncertainties are inevitable in radiotherapy. These uncertainties in tumour position are classified as systematic (Σ) and random (σ) errors. To account for these uncertainties, a margin is added to the clinical target volume (CTV) to create the planning target volume (PTV). The size of the PTV is critical for obtaining an optimal treatment plan. Dose-based (i.e., physical) margin recipes as a function of systematic and random errors based on coverage probability of a certain level of dose (90% or 95% of the prescription dose) have been published and widely used. However, with a TCP-based margin it is possible to consider fractionation and the radiobiological characteristics, especially the dose-response slope (γ_{50}) of the tumour. Studies have shown that the density of the clonogens decrease from the boundary of the gross tumour volume (GTV). In such a scenario, dose that is lower than in the GTV should be sufficient to eradicate these clonogens. Thus a smaller PTV margin with a gradual dose fall-off can be used if the clonogen density in the GTV-CTV region is found to be lower than in GTV. Studies have reported tiny tumour islets outside the CTV region. These tiny tumour islets can be eradicated in some cases by the incidental dose outside the PTV due to the nature of the photon beam irradiation, but if they are not in the beam path the treatment outcome is compromised.

In this thesis, a Monte Carlo approach is used to simulate the effect of geometric uncertainties, number of fractions and dose-response slope (γ_{50}) using the 'enhanced Marsden' TCP model on the treatment outcome. Systematic and random errors were drawn from a pseudo-random number generator.The dose variations caused by tumour displacements due to geometric uncertainties in the CTV are accumulated each fraction on a voxel-by-voxel basis. Required margins for $\leq 1\%$ mean population TCP ($\overline{TCP}_{pop}$) for four-field (4F) brick and a highly conformal spherical dose distribution for varying number of fractions, different γ_{50} and different combinations of Σ and σ are investigated. It is found that TCP-based margins are considerably smaller than dose-based recipes in most cases except for tumours with a steep dose-response slope (high γ_{50}) and a small number of fractions for both 4F and spherical dose distributions. For smaller geometric uncertainties ($\Sigma = \sigma$=1 mm) margins can be close to zero for the 4F technique due to high incidental dose outside the PTV. It is evident from the analyses that margins depend on the number of fractions, γ_{50}, the degree of dose conformality in addition to

Σ and σ. Ideally margins should be anisotropic and individualized, taking into account γ_{50}, number of fractions, and the dose distribution, as well as estimates of Σ and σ. No single "recipe" can adequately account for all these variables.

Using an exponential clonogen distribution in the GTV-CTV region, possible PTV margin reduction is demonstrated. Moreover, the effect of extra-CTV tumour islets is studied using a prostate IMRT plan. The islets were randomly distributed around the CTV with in a radius of 3 cm to represent different patients. The doses were rescaled up to 102 Gy to obtain the dose-response curve (DRC). Interestingly, the obtained DRC showed a biphasic response where 100% TCP could not be achieved just by escalating the dose.

Another potential problem encountered in intensity-modulated radiotherapy (IMRT) is the problems caused by the 'interplay' effect between the respiration-induced tumour motion and the multileaf collimator (MLC) leaves movement during treatment. Several dosimetric studies in the literature have shown that 'interplay' effects blur the dose distribution by producing 'hot' and 'cold' dose inside the tumour. Most of these studies were done in a phantom with ion chambers or films, which provide only 1D or 2D dose information. If 3D dose information is available, a TCP based analysis would provide a direct estimate of interplay on the clinical outcome. In this thesis, an in-house developed dose model enabled us to calculate the 3D time-resolved dose contribution to each voxel in the target volume considering the change in segment shapes and position of the target volume. Using the model, delivered dose is accumulated in a voxel-by-voxel basis inclusive of tumour motion over the course of treatment. The effect of interplay on dose and TCP is studied for conventionally and hypofractionated treatments using DICOM datasets. Moreover, the effect of dose rate on interplay is also studied for single-fraction treatments. Simulations were repeated several times to obtain mean population TCP ($\overline{TCP}_{pop}$) for each plan. The average variation observed in mean dose to the target volumes were $-0.76 \pm 0.36\%$ for the 20 fraction treatment and $-0.26 \pm 0.68\%$, $-1.05 \pm 0.98\%$ for the 3- and single-fraction treatments respectively. For the 20-fraction treatment, the drop in $\overline{TCP}_{pop}$ was $-1.05 \pm 0.39\%$, whereas for the 3 and single fraction treatments it was $-2.8 \pm 1.68\%$ and $-4.0 \pm 2.84\%$ respectively. By reducing the dose rate from 600 to 300 MU/min for the single-fraction treatments; the drop in $\overline{TCP}_{pop}$ was reduced by $\sim 1.5\%$. In summary, the effect of interplay on treatment outcome is negligible for conventionally fractionated treatments, whereas a considerable drop in TCP is observed for the 3- and single-fraction treatments. Where no motion management techniques such as tracking or gating are available for hypofractionated treatments, reduced dose rate could be used to reduce the interplay effect.

Acknowledgments

I would like to extend my sincere thanks my supervisors, Prof. Alan Nahum and Dr Colin Baker for their valuable guidance, support and encouragement through out my project. I appreciate their contributions of time, ideas and funding to make my PhD experience productive and stimulating. I am very grateful to Dr. Julien uzan for his time and very useful suggestions he has given in TCP modelling and reviewing the manuscripts and my thesis.

I thank the IT department of Clatterbridge Cancer Centre for providing extra computers for running the 'interplay' effect simulations which saved me quite a lot of time.

Many thanks to the members of the physics department of Clatterbridge Cancer Centre who made my working experience memorable.

Special thanks to the members of the vtk and gdcm users list who helped me solve problems encounterd in developing BioSim and also for enhancing my vtk knowledge.

My heartfelt thanks to all my friends in Liverpool who made my time enjoyable with interesting conversations, nice food they make and weekend activities.

Last but not the least, I grateful to my family members who have been encouraging and supportive through out my career.

Contents

List of Figures

List of Tables

Chapter 1

Introduction

1.1 Radiotherapy

Radiotherapy is a branch of medicine which uses high-energy ionizing radiation to treat cancer. The deposition of this energy in living tissues results in damage to the cells' DNA which make them incapable of dividing and reproducing themselves. Although radiation is received by normal and abnormal (tumor) cells, abnormal cells are more susceptible to radiation as they divide more rapidly than normal cells. Over a period of time with sufficient radiation dose the tumor cells die, whereas normal cells will repair more effectively than tumor cells. The goal of radiotherapy is to maximize the radiation dose to the tumor for an acceptably small damage to the normal tissues. This is referred to as *optimizing the therapeutic ratio*.

There are two main types of radiation therapy, namely external beam radiotherapy (EBRT) and brachytherapy, the former being more often used than latter. Both modalities can occasionally be used together. For instance, in localized prostate, cervix and breast cancer brachytherapy is commonly used to boost the dose to the gross tumor volume. EBRT is generally delivered using a linear accelerator with qualities in the range of 4-15 MV bremsstrahlung photons. The radiation beams are directed at the tumor with the patient precisely positioned on the treatment couch. The prescribed dose is then generally delivered using multiple beams from different orientations over many fractions. Delivering the prescribed radiation dose by multiple beams significantly reduces the volume of high dose delivered to the normal tissues by spreading the radiation energy over a large volume of normal tissues. Hence, more dose can be delivered to the tumor with fewer normal tissue complications. Figure 1.1 shows a typical prostate radiotherapy treatment with five beams or fields, each from a different direction.

Radiotherapy has evolved from simple square/rectangular field treatments into complex 3D conformal radiotherapy (3DCRT) and later into even more complex intensity-modulated radiotherapy (IMRT) treatments. With these advanced forms of radiother-

apy, it is possible to reduce the dose to normal tissues substantially and hence more dose can be delivered to the tumor for low normal tissue complication risk. Over the years, the accuracy in dose calculation and ability to optimize radiotherapy treatments with physical dose/biological cost functions have greatly improved due to significant advancements in computer technology. It is only recently, however that treatment delivery and patient positional accuracy been improved with image-guided radiotherapy (IGRT). Nevertheless, patient positional uncertainties, accuracy in target volume delineation, knowledge of clonogen density distribution inside and around the tumor volumes and their consequences for treatment outcome are still areas of intense research. In this thesis the effects of these factors on treatment outcome are investigated using a mechanistic tumor control probability (TCP) model. Some of the methodology and basic concepts used in radiotherapy planning and the problems associated with them are described in the following sections.

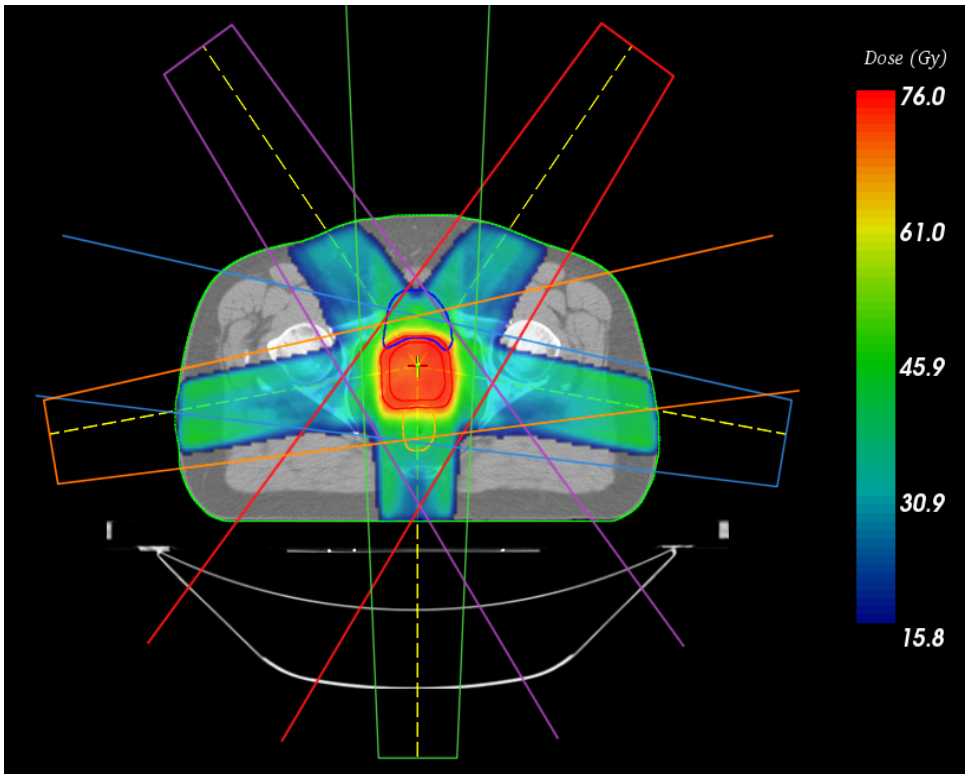

Figure 1.1: Prostate plan with multiple fields

1.2 ICRU62 volume definition in radiotherapy

To enable consistent clinical practice, the International Commission on Radiation Units and Measurements (ICRU) [1, 2] has defined volumes used in treatment planning and for evaluation purposes. Figure 1.2 shows the volumes defined by ICRU62, according to which

- *Gross tumor volume* (GTV) is gross palpable or visible/demonstrable extent and

location of malignant growth.

- *Clinical target volume* (CTV) is an anatomical concept which contains GTV and/or sub clinical microscopic disease which has to be eliminated in order to achieve the aim of therapy.

- *Planning target volume* (PTV) is a geometric concept which takes into account all the possible geometrical uncertainties and inaccuracies in the treatment so that the prescribed dose is absorbed in the CTV.

  PTV is comprised of internal target volume (ITV) and setup margin (SM), which takes care of internal motion of the CTV and setup errors respectively.

- *Treated volume* (TV) is the volume encompassed by the isodose surface selected by the radiation oncologist that is considered to achieve the purpose of treatment.

- *Irradiated volume* (IV) is the volume that receives a dose that is considered significant in relation to normal tissue tolerance.

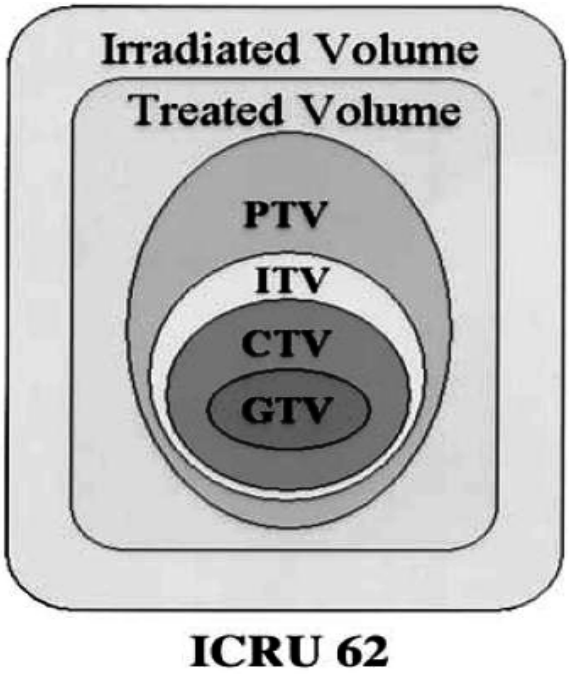

Figure 1.2: Volume definition in radiotherapy- ICRU62

1.3 Geometric uncertainties in radiotherapy

A course of radiotherapy is comprised of several procedures which are linked to others as illustrated in figure 1.3. The first procedure is patient immobilization, by which the patient is immobilized in the treatment position using a suitable immobilization device. The patient is then scanned generally using a CT scanner; which provides a 3D model of the patient along with physical characteristics of tissues to be used for

dose calculation. tumor and critical structures are then contoured on the image slices and 3D treatment planning is performed. At treatment time, the patient is positioned on the treatment couch and aligned with the isocentre, occasionally with the help of immobilization devices and the treatment is delivered. However due to inaccuracies in the procedures involved, targeting the tumor with a high degree of precision is difficult. Small errors will occur in each step of the process which will combine under the umbrella concept of "geometric uncertainties" [3].These geometric uncertainties are categorized as systematic (Σ) and random errors (σ). Systematic errors will have the same effect on all fractions of the treatment while the effect of random errors may vary from fraction to fraction. A schematic representation of the effect of geometric uncertainties on the day-to-day position of the target volume is shown in fig 1.4. Figure 1.5 shows the distribution of systematic and random errors drawn using a quasi-random number generator in eight patients over a ten fraction treatment and their corresponding vector sum of both (Σ & σ).

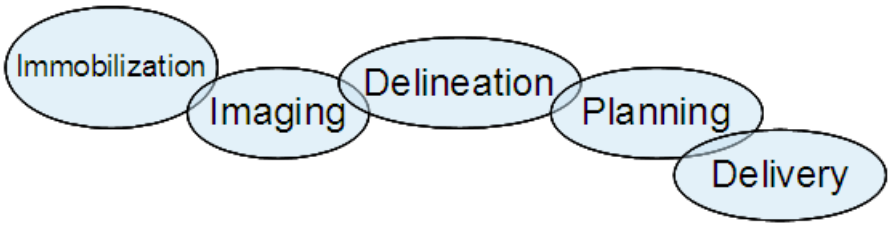

Figure 1.3: Radiotherapy process chain

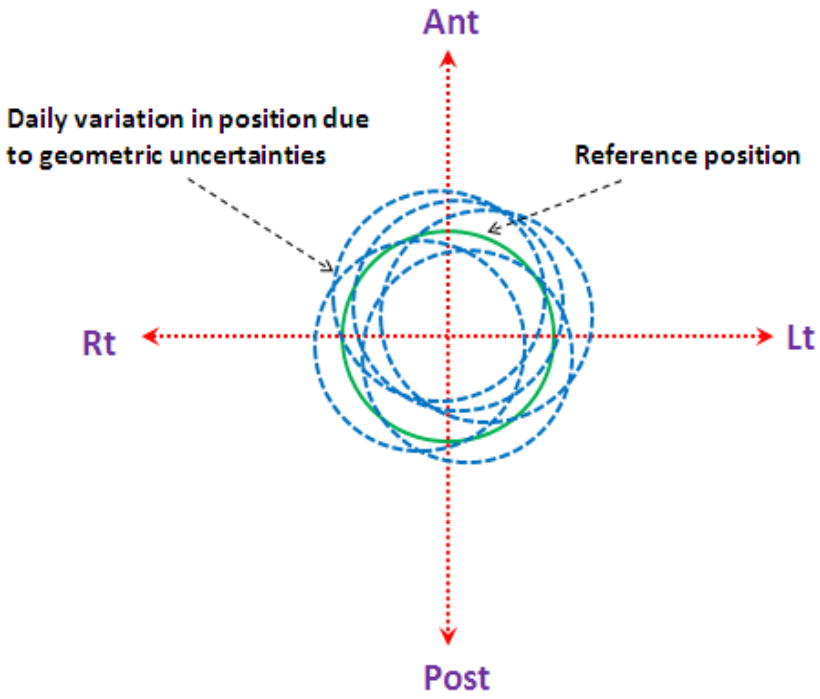

Figure 1.4: Day-to-day variation in target position due to geometric uncertainties shown relative to the reference position (solid circle).

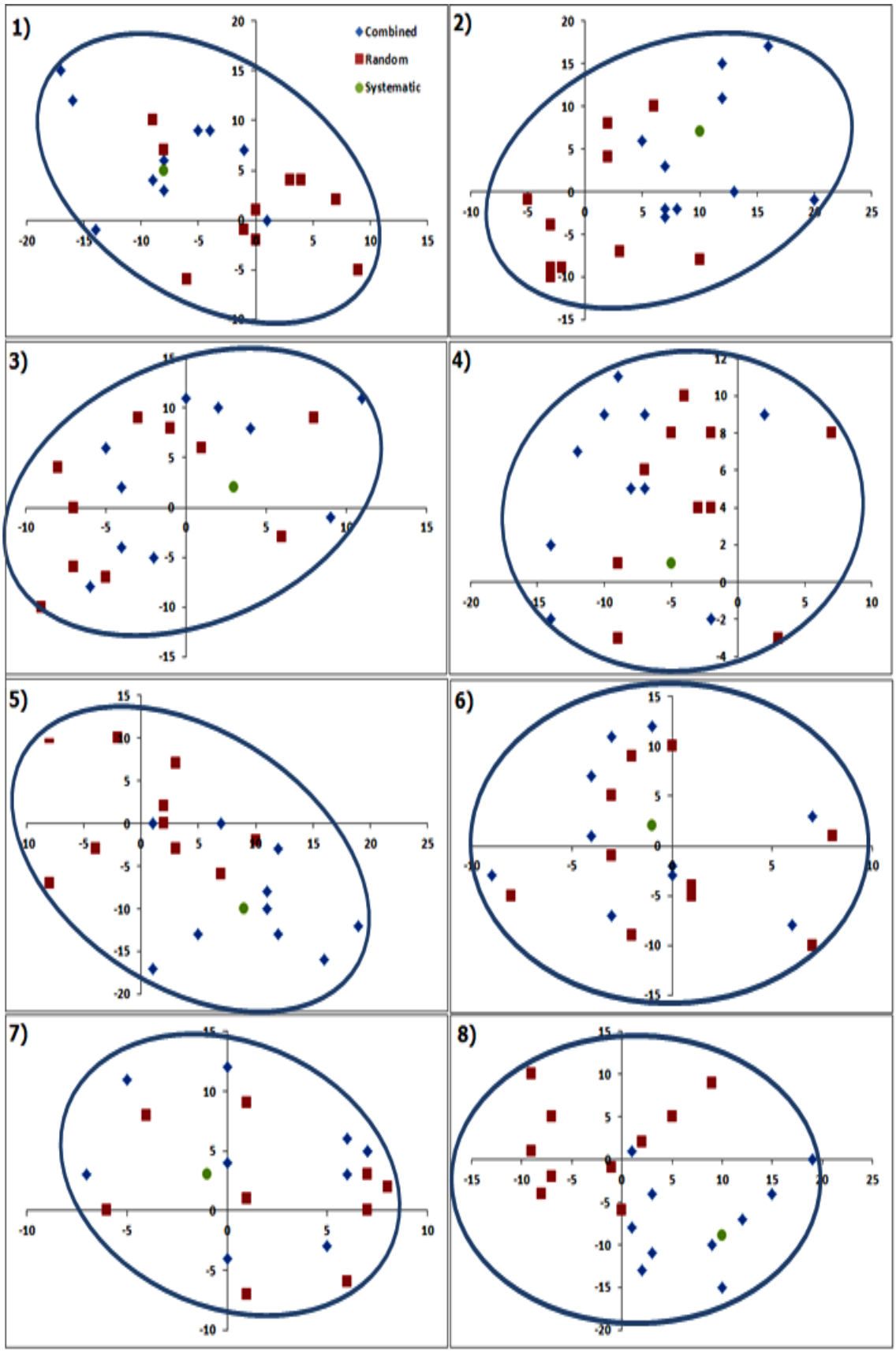

Figure 1.5: Randomly generated systematic and random errors and their vector sum for 8 different patients with 10 fractions each

The sources of uncertainties in radiotherapy include inaccuracies in the delineation of the gross tumor volume (GTV), determining the extent of microscopic tumor (CTV) which should be given the therapeutic (i.e.prescribed) dose, organ/tumor inter-fractional and intra-fractional morphological changes and setup errors. The inaccuracy in the definition of the GTV may arise from the limitations in imaging modalities, which have a limited resolution, especially in the cranio-caudal direction causing the partial-volume effect [4]. Moreover, inter [5, 6] and intra-observer variations [6–10] in delineating the target volumes are inevitably reflected in the accuracy of target volume delineation. This uncertainty in target volume delineation belongs to the category of systematic errors.

The second source of uncertainty is the definition of the extent of microscopic disease spread i.e. CTV. Though modern treatment planning systems (TPS) offer a great deal of flexibility and precision in delineating gross tumor (GTV) and normal tissues [11,12], delineating the extent of CTV is one of the most challenging tasks for the radiation oncologist. In many cases it is based on the experience of the radiation oncologist, as currently available imaging techniques cannot show microscopic disease. The literature on this subject is vague and the CTV definition is considered 'art' rather than 'science' [13]. There are a few studies which address the extent of microscopic spread of disease based on the surgical resection of specimens for prostate and head-and-neck tumors. Giraud *et al* [14] have shown that a CTV margin of 6 to 8 mm is necessary to cover 95% of the microscopic disease in head and neck tumors. Diaz *et al* have shown in clinically localized prostatic cancer, 47% patients could have been treated excluding seminal vesicles since the seminal vesicles were not involved, which in turn allows higher dose to prostate with lesser rectal toxicity [15]. Though use of a generous CTV margin will reduce the risk of missing microscopic disease, it will also increase the risk of normal tissue complications. Therefore, improvement of the therapeutic ratio depends heavily on *precisely* defining the GTV and CTV volumes.Other major sources of uncertainties in radiotherapy include setup errors [16–18] and organ motion [13, 19–22]. Several studies have shown that setup errors can be reduced by using improved immobilization techniques and setup protocols [16–18, 23–26]. With the advent of 'on-board' imaging such as electronic portal imagers (EPIs) and cone-beam CT (CBCT), setup errors can be precisely measured and corrected. However, the setup verification procedures can only reduce the errors, not completely eliminate them (even the setup errors) due to the limitations in the accuracy of EPIs or CBCT systems. For instance, the target delineation errors cannot be estimated nor corrected by the setup verification procedure. Moreover, organ motion cannot be accounted by setup verification procedures; especially in cases where organ motion management is not used. Thus, the residual errors can never be *totally eliminated* and the CTV *always* requires a margin. The most common approach to account for these uncertainties is to expand the tumor volume (CTV) with an additional margin (PTV). The size of this PTV margin is crucial in

obtaining an optimal treatment plan. In the past, when there were no tools to measure setup errors these margins were purely empirical. The advent of on-board imaging tools made it possible to measure setup errors with high accuracy; they can provide a detailed knowledge of the distribution of errors over a population of patients. Over the last decade much attention has been paid to measuring and correcting geometric errors which has paved the way for a new era in radiotherapy known as *image-guided radiotherapy* (IGRT).

Respiration-induced tumor motion is another cause for concern in radiotherapy. Respiration can contribute to both systematic (Σ) and random(σ) errors. Motion can be accounted for by two methods if its magnitude is known [27, 28].The most common approach is to expand the CTV with a margin for motion (ITV). This margin is added essentially to make sure the CTV receives the prescription dose even when it is moving.The second method is to model the breathing motion to accurately predict the dose delivered to target and normal tissues over the breathing cycle [29, 30]. While the first approach is apparently simple to use, it is always not possible to use a sufficiently large margin in the presence of nearby critical structures. In conventional, static-field treatments, the fluence delivered by a field is spatially (except in the penumbra region) and temporally invariant. Because of this invariance, the introduction of motion will only produce a *blurring* effect of the dose at the edges of the target.This blurring effect is similar to the effect of random errors (σ), but the blurring occurs in every fraction as opposed to blurring over a large number of fractions due to random errors. This effect can be easily managed by using a sufficient ITV margin. On the other hand, fluence in intensity-modulated fields is spatially and temporally varying, generally created by moving the MLC leaves into different positions over time. In IMRT, the implicit condition is that the dose delivered by the different segments add up as planned in the absence of movement of the target. In the presence of motion however, the dose delivered to a moving target will not add up as planned potentially causing "*hot*" and "*cold*" spots in the target volume. This effect is depicted in figure 1.6.

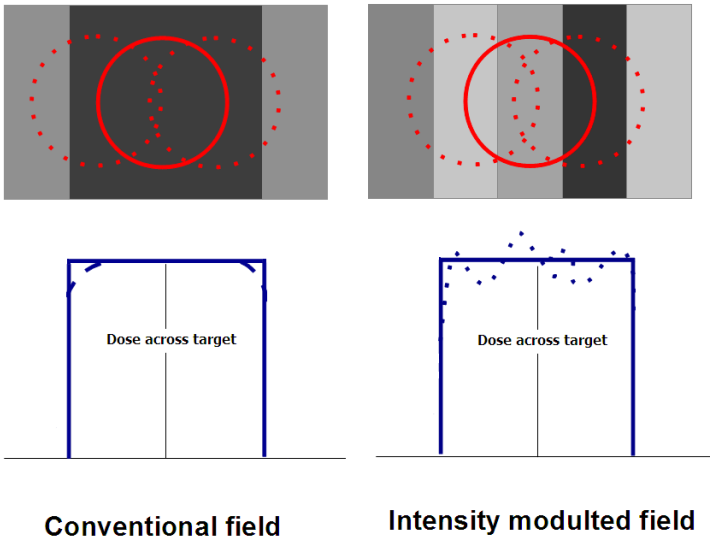

Figure 1.6: Effect of tumor motion(left-to-right) in conventional and intensity-modulated fields. Darker shades of grey represent higher fluence. For simplicity the variation of fluence is shown in 1D. Solid and dotted lines represent dose across target respectively while it is static and moving

While IMRT is preferable to conventional uniform-field radiotherapy for treating some tumors due to its superior normal-tissue sparing capabilities [31–36, 36, 37] there is still some concern about its use for lung tumors because of the dose blurring effect caused by the 'interplay' effect. Several studies [38–45] have shown including the AAPM report "The management of respiratory motion in radiation oncology report of AAPM Task Group 76" [46] that treating tumours affected by respiratory motion with intensity modulated fields remains a concern. Many of these studies doesn't account target deformation during motion and the effect of target deformation on dose distribution remains unknown. Some of these studies have shown that the effect of interplay between tumour motion and MLC leaves average out for treatments with many fractions (∼30 fractions) if a random respiratory phase is assumed from day to day. However, the effect of tumour motion and MLC leaves remains a concern for hypofractionated treatments and this has been emphasized by AAPM report 91 [46]. In addition, lung tumours are the most affected by interplay effect since they tend to displace more than other tumours such as liver or kidneys. Lung tumours are known to have a steep dose-response curve and it indicates a small change in the dose could result in a large change in the biological effect. Different patients have different patterns of breathing including frequency, amplitude, different tumour size, MLC shapes and its weight in the treatment fields and different number of treatment fractions. It is thus very difficult to construct a mathematical model to predict the effect of interplay for a given pattern of MLC movement on tumour control probability. In such a scenario, a computer simulation model of the interplay between tumour motion and the MLC leaves for the

given patient considering the radiobiological characteristics of the tumour (clonogen density, radiosensitivity, dose-response curve), number of fractions and the MLC shapes within each field will provide a valuable estimate of the impact of interplay effect on tumour control.

1.4 Aims

1.4.1 PTV margins

Several research groups have proposed margin recipes based on the knowledge of the distribution of geometric uncertainties in the patient population. Bel *et al* [47] have proposed a margin of 0.7σ to account for random uncertainties alone based on dose distribution of three and four rectangular field prostate treatment plans, so that the minimum dose to the CTV will be 95% of the prescription dose. It should be noted that this number of 0.7 corresponds to a specific beam arrangement and its applicability to other beam arrangements is not valid. Antolok *et al* [48] recommended a margin of 1.65 times random uncertainties which guarantees a minimum CTV dose that is greater than 95% of the minimum PTV dose, but this does not assume any specific beam arrangements nor a specific penumbra profile. The effect of systematic uncertainties, which has a substantial effect on the CTV dose has been ignored in both these studies. Excluding systematic uncertainties results in under estimation of margins which leads to frequent geometric miss of the CTV. In order to accurately model the effect of geometric uncertainties on TCP which depends on knowing the dose that is exactly delivered to the target volume, it is important to account the dose discrepancies caused by both systematic and random uncertainties. Others [49–53] have considered both systematic and random uncertainties in the margin calculation with different assumptions (% of minimum CTV dose, % of CTV receiving the minimum prescribed dose, width of beam penumbra and the gradient of dose fall off and rotational errors). McKenzie *et al* [49] argued that the beam configuration should be taken into account while calculating margins since the dose blurring on the edge of the target volume depends on the number of beams and their orientation. Stroom *et al* [51] and van Herk *et al* [53] proposed margin recipes based on coverage probabilities(probability of certain percentage of CTV volume being covered by certain percentage of the prescription dose). van Herk *et al* [53] suggested a recipe based on coverage probability which includes the width of beam penumbra. However, this is hardly used in any clinic, rather the simplified formula of $2.5\Sigma + 0.7\sigma$ is used. It is also important to note that different tumour types behave differently to same amount of underdosage or overdosage depending on their radiobiological characteristics. While most of these recipes are based on the physical dose delivered to the target volume, a TCP based margin recipe will be more appropriate since it accounts for the radiobiological characteristics of the tumour. van

Herk *et al* [52] proposed a TCP based margin recipe for $\leq 1\%$ drop in population mean TCP for prostate radiotherapy. The σ_α assumed is 0.08 which corresponds to a shallow dose-response curve which is a good approximation for prostate tumours. They also emphasized the importance of including the rotational errors in the margin calculation especially for prostate treatments where the seminal vesicles rotate about a point that is distant from the prostate. They showed a reduction of 30% in probability (from 90 to 60 %) in delivering minimum of 95% of the prescription dose in three field prostate plans if the rotational errors were not included. It was shown by them that the effect of rotational errors are highly dependent on position of the part of the tumour that is rotating and the point about which it rotates. This severe underdosing is due to the complex shape the target volume has when seminal vesicles are added to the prostate tumour in margin determination. The rotational errors may differ from patient to patient even for the same tumours and difficult to predict accurately. Hence, the effect of rotational errors are not included in this thesis and also the aim is to compare margins based on TCP and dose-based recipes and to get insight into the dependence of margins on fraction number, dose-response curve of the tumour and geometrical uncertainties. Jin *et al* [54] went a step further and included the microscopic disease extension in the margin determination and concluded that the margins required for a given set of geometric unceertainties are relatively much smaller if an exponentially decreasing microscopic disease in the GTV-CTV region is assumed. For instance, the margins calculated according to their recipe is 4 mm for $\Sigma = 3, \sigma = 3$ mm whereas it is 10 mm according to the van Herk recipe of $2.5\Sigma + 0.7\sigma$. It should be noted that the metric assume d in both these recipes are different. Although margin recipes are published which includes microscopic disease distribution, it is very difficult to use for PTV determination for the patients as the knowledge of microscopic disease is not adequate.

Sources of systematic errors include but are not limited to target delineation errors, image blurring caused by organ motion which will shift the mean organ position, phantom transfer error (error in transferring the patient position from imaging equipment to the treatment machine) [55]. Sources of random errors include but again are not limited to intra-fraction organ motion, daily setup errors and mechanical inaccuracies of the linac [55]. Assuming that these individual errors are independent of each other and have a Gaussian distribution, the combination of *all* systematic and *all* random errors can be obtained by their quadratic sum as shown in equation (1.1)

$$\Sigma = \sqrt{\Sigma^2_{delineation} + \Sigma^2_{motion} + \Sigma^2_{transfer} + \Sigma^2_{setup}} \tag{1.1a}$$

$$\sigma = \sqrt{\sigma^2_{organ\,motion} + \sigma^2_{patient-setup}} \tag{1.1b}$$

The assumptions on which the margin recipes were derived and their corresponding

recipes are given in table 1.1.

Table 1.1: Margin recipes based on geometric uncertainties

Group	Recipe	Comments/Criteria
Bel *et al* [47]	0.7σ	Random errors only
Antolak and Rosen *et al* [48]	1.65σ	Random errors only
Stroom *et al* [51]	$2.0\Sigma + 0.7\sigma$	95% dose to 99% of CTV on average
Van Herk *et al* [52]	$2.5\Sigma + 1.64(\sigma - \sigma_p)$	Minimum 95% dose to 90% of the patients.σ_p is the standard deviation of the Gaussian penumbra
McKenzie *et al* [49]	$2.5\Sigma + \beta(\sigma - \sigma_p)$	Same as van Herk *et al* [52] but includes fringe dose
Parker *et al* [50]	$\Sigma + \sqrt{\Sigma^2 + \sigma^2}$	Minimum 95% dose and 100% dose to 95% of the CTV
Van Herk *et al* [53]	$2.5\Sigma + 0.7\sigma$ -3mm	$\leq$1% TCP loss in prostate patients
Jin *et al* [54]	$\sqrt{(0.75\sigma)^2 + (1.15\Sigma)^2}$	2% drop at 90% TCP (margin added to GTV accounting for the decreasing density of clonogens in GTV-CTV region)

Though there are several recipes, the van Herk *et al* [52] recipe is the most widely used. In its simple form, the components for a given standard deviation of systematic (Σ) and random(σ) errors are added linearly. It is based on the fact that systematic and random errors have a different effect on the cumulative dose to the target. Systematic errors tend to *shift* the dose distribution while random errors *blur* the dose distribution (for number of fractions ≥ 20). Many of these margin recipes are based on the probability that for a given percentage of patients in a population, the CTV would

receive a certain percentage of the prescription dose. However, margins based on TCP would arguably be more appropriate than dose-based margins, as TCP-based margins are directly linked to the treatment outcome. In addition, radiobiological models consider the tumor dose-response characteristics. Van Herk *et al* [53] provided a margin recipe for prostate tumors treated with a large number of fractions with the criterion being $\leq$ 1% loss in population mean TCP ($\overline{TCP}_{pop}$). However, this recipe is only applicable for prostate tumors treated with $\geq$20 fractions and cannot be applied for tumors with other dose-response characteristics (γ_{50}) and for hypofractionated treatments. Brahme [56] concluded that higher tumor control could be achieved only if the dose delivery accuracy was very high, especially for tumors with a steep dose-response gradient (γ_{50}). This implies that the same degree of uncertainty in dose delivery in tumors with different γ_{50} will cause varying effects on tumor control. Moreover, hypofractionated treatments are becoming more and more common especially for medically inoperable lung tumors where stereotactic ablative body radiotherapy (SABR) is showing promising results [57]. It is thus imperative to understand the relationship between CTV-PTV margins, geometric uncertainties, fractionation, tumor dose-response characteristics and treatment outcome i.e. TCP.

1.4.2 Microscopic disease distribution

As mentioned before, a margin is added to the GTV to create the CTV and thereby include the microscopic disease extension. In clinical practice this assumes that there are no tumor cells outside the CTV and the density of the clonogenic cells is same as inside the GTV. However, histopathological studies have shown that the tumor cell density in the microscopic disease extension (MDE) region decreases with the distance from the GTV boundary and may not be limited to the CTV [14, 58, 59]. The assumption of equal clonogen density in the GTV-CTV region as in the GTV leads logically to the need for a prescription dose to the CTV equal to that in the GTV. Conversely, in cases where the density of the clonogenic cells decreases from the boundary of the GTV, the resulting smaller number of clonogenic cells can be eradicated with less dose than that prescribed to the GTV. This is depicted in figure 1.7 for the assumed(*uniform clonogen density*) and possible (*decreasing clonogen density*) scenarios in the GTV-CTV region and possible dose reduction in the CTV-PTV region. The reduced prescription dose in the CTV-PTV region will in turn reduce the required PTV margin. Moreover due to the nature of the external photon beam irradiation, considerable dose is deposited outside the PTV along the beam pathways. This *incidental* dose outside the PTV may be sufficient to eradicate the low density clonogenic tumor cells outside the CTV [60–62]. PTV margins could be reduced if the clonogen density outside the GTV were known and found to be lower than in the GTV. Only a few studies have quantified the extent to which the PTV margin can be reduced given reduced clonogen density in the GTV-

CTV region. Microscopic tumor islets have been found in 50% of NSCLC patients with an average of 5 islets per patient varying from 1 to 3 mm in diametre [63]. Using this data Siedschlag *et al* [64] have done a Monte Carlo simulation of the effect of MDE on TCP for conventional and stereotactic treatments for various degrees of geometric uncertainties (systematic & random errors). They concluded that TCP improved with increasing geometric uncertainties due to larger PTV margin used to account for larger geometric uncertainties. They have aslo shown that MDE may not always be eradicated by the penumbra or the PTV margins. This questions the decrease of the PTV margin in IGRT treatments where extent of microscopic disease is not accurately known. In another interesting study, Witte *et al* [65] reported that there are low density clonogenic islets in prostate cases which have been eradicated by the 'incidental' dose in some cases but not in others due to the different beam orientations used. These studies provide useful insights into the effect of microscopic disease and low density tumor islets on TCP. However, it would be useful to know how the TCP drops for a given set of systematic (Σ) and random(σ) errors in the presence of tumor islets which are outside the defined CTV. It would also be interesting to know the effect of gradient in clonogen density in the GTV-CTV region on TCP as a function of PTV margin for different Σ and σ.

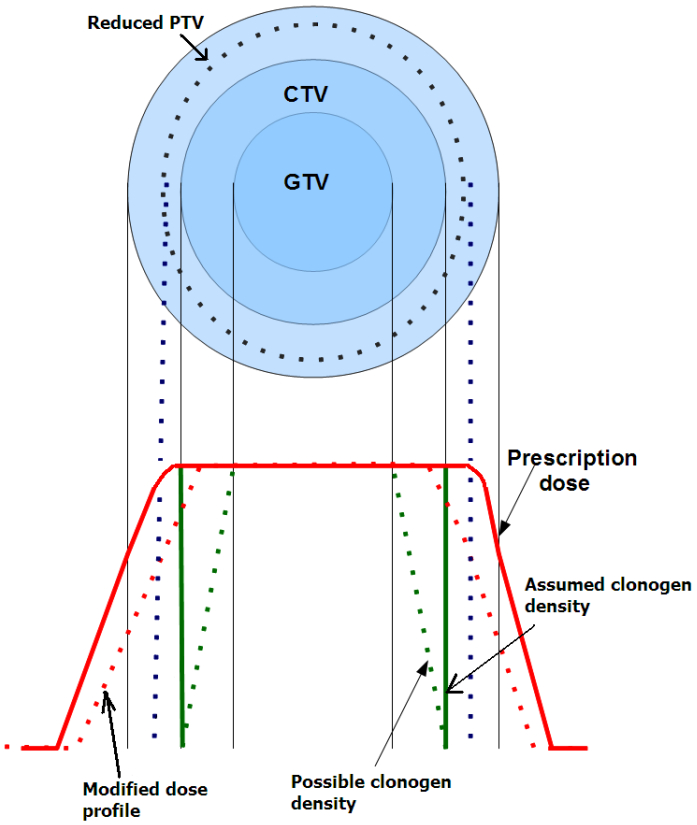

Figure 1.7: Assumed and possible scenarios of clonogen density in the GTV-CTV region and possible PTV margin reduction. The possible and assumed scenarios of dose and clonogen density are represented by dotted and solid lines respectively

1.4.3 Interplay effect in IMRT

These are several studies which have quantified the impact of interplay between MLC movement and tumour motion. But most of these studies have reported the change in the dose to tumour either on a single point or multiple points. However the tumour control actually depends on the dose delivered to the each voxel of the tumour. Moreover, a TCP based analysis with appropriate dose-response slope for lung tumours and fractionation will provide better insights into the effect of interplay on hypofractionate treatments and conventional treatments.

A simulation model is presented in this thesis to obtain the change in the mean population TCP($\overline{TCP}_{pop}$ due to interplay effect for the given patient treatment plan considering the prescription dose, number of fractions and the radiobiological characteristics of the tumour. A ray tracing model is used to find out the voxels that are missed or irradiated by the primary radiation beam during tumour motion while also considering the MLC shape at the given time interval. A dose calculation methodology which account for tissue attenuation, MLC leakage and penumbra at the field edges is presented. The effect of interplay for three different fraction 1, 3 and 20 are studied

using the Marsden TCP model. The simulations are repeated several times for each patient to obtain $\overline{TCP}_{pop}$. As the dose rate increases, the treatment duration decreases. As a result of this, the intrafraction dose blurring effect is reduced an the effect of interplay can worsen. To study this two different dose rates are considered namely, 300 MU/min and 600 MU/min.

Chapter 2

Tumor Control Probability

Cells are the basic structural, biological and functional unit of all living organisms. The main constituents of the cell are the cytoplasm, which supports all metabolic functions and the nucleus which contains the DNA. When cells are exposed to ionizing radiation the standard physical interaction between the atoms of the cell and the radiation particles occur followed by possible biological damages to cell's functions. The biological damages are believed to occur due to the damage of the DNA, which is considered to be the most critical target within the cell. The damage may occur directly or indirectly depending upon the nature of the radiation. In direct action, the radiation interacts directly with the atoms of the critical target (DNA) which leads to physical and chemical events that result in biological damage. Direct action mainly occurs with high LET (linear energy transfer) radiation whereas indirect action is responsible for cell damage in low LET radiation such as x-rays and electrons. In indirect action the radiation interacts with molecules and atoms (mostly water, as 80% of cell is composed of it) within the cell to produce short lived but highly reactive free radicals such as H_2o^+ and OH. The free radicals in turn break the chemical bonds of the DNA which leads to biological damage. The DNA has two strands formed in a double helical structure. SSBs are easier to repair than DSBs. The damages to the DNA can be caused in the form of single strand breaks (SSBs) or double strand breaks (DSBs) The resulting damage caused by radiation is divided in to three categories:

- *Lethal damage*, which is irreversible and irreparable and leads to cell death.
- *Sub lethal damage* is reparable if sufficient time is given unless additional damage is made.
- *Potentially lethal damage* is repairable if the cells are allowed to remain in a non-dividing state for a long time before additional damage is made.

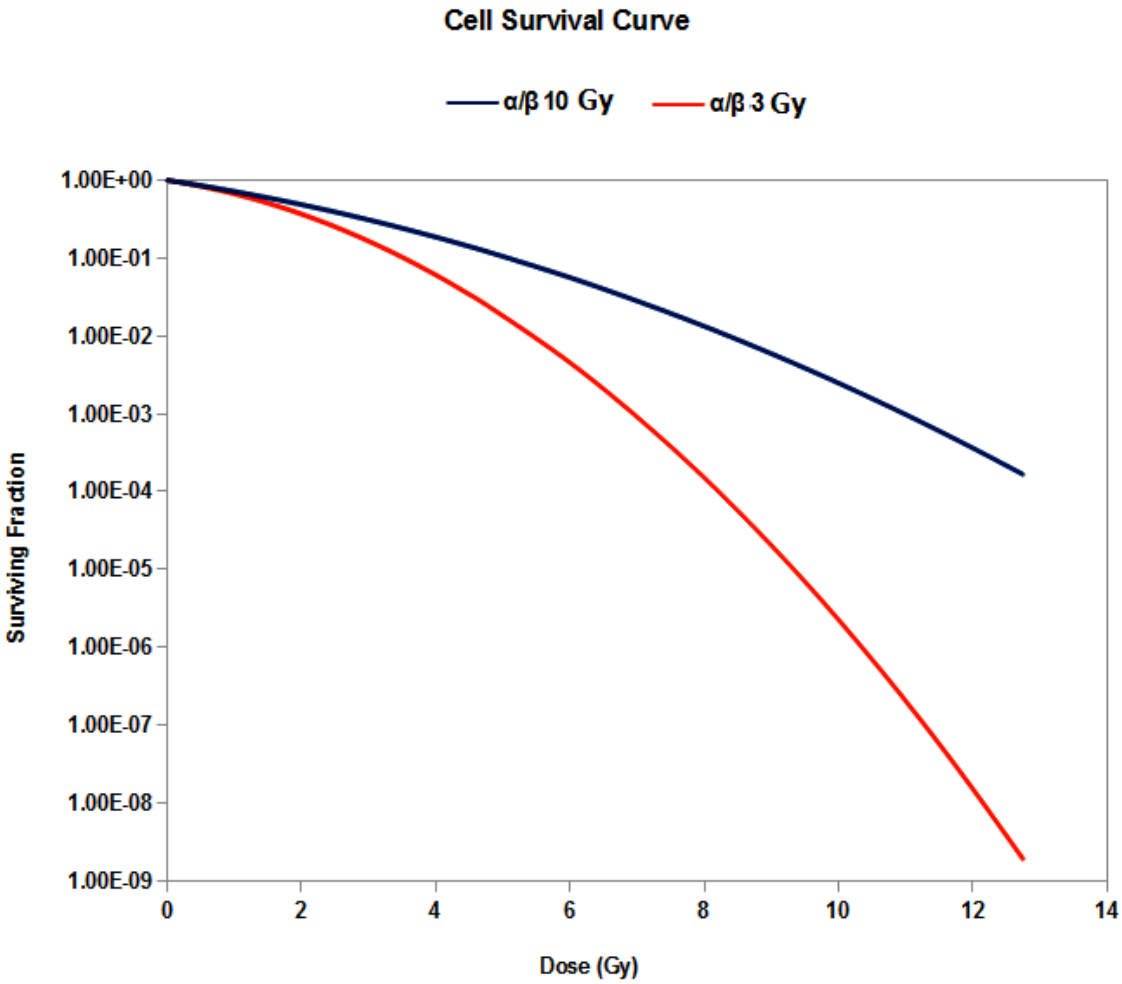

Figure 2.1: Cell survival curves for two different α/β ratios; 3 Gy (normal tissues) and 10 Gy (tumor) for single fraction.

2.1 Linear-Quadratic model based TCP calculation

It has been clinically and experimentally observed that the dose-response curves (DRC) have a sigmoidal shape. A simple approach is to fit a mathematical function to this curve, but such an approach will not be able to incorporate the changes in tumor radiosensitivity and inhomogeneity in dose distribution. Radiobiological experiments have shown that cell killing by radiation in certain cell lines can be described by a linear-quadratic (LQ) model [66–68]. The α and β parameters (which are described in the next section) in the LQ model characterize the initial slope and degree of curvature respectively of the cell survival curve. Figure 2.1 shows the survival curves for two different α/β ratios.

There are several models to quantify TCP including the Niemierko and Goitein model [69] and the 'Marsden' model [70]. All these models are very similar to each other and assume that tumors have a sigmoidal DRC and use the LQ model of cell kill

with Poisson statistics to calculate the probability for clonogens to survive. The original "Marsden" TCP model does not account for fractionation effects and it was modified by Nahum and Sanchez-Nieto [71] to account for fractionation, which is refered to as the "Enhanced Marsden" model in this thesis. The "Enhanced Marsden" model is used in the entire work carried out in this thesis.

2.1.1 TCP calculation

The linear-quadratic (LQ) model assumes that there are two contributions of cell killing by radiation namely 'linear' and 'quadratic' contributions. The 'linear' contribution refers to damage produced by a single track of radiation whereas 'quadratic' contribution is produced by two different radiation tracks. The 'linear' contribution of cell kill is directly proportional to the dose d and the 'quadratic' contribution is proportional to d^2.

The total cell kill by radiation is given as an exponential form of both 'linear' and 'quadratic' contributions. The amount of cell kill produced by single track radiation is given by the α term in units of log cells killed per Gy and the amount of cell kill produced by two different radiation tracks is given by the β term in units of log of cells killed per Gy^2. Assuming an initial clonogen number of N_0 and N_s number of surviving cells, the surviving fraction of cells can be written as $SF = N_s/N_0$. The mean fraction of cells surviving a single dose of d is given by equation (2.1).

$$ln(SF) = -(\alpha d + \beta d^2) \tag{2.1}$$

which can be written as

$$SF = e^{-(\alpha d + \beta d^2)} \tag{2.2}$$

for n fractions of d Gy each, the mean surviving fraction would become

$$SF = e^{-(\alpha nd + \beta n d^2)} \tag{2.3}$$

Therefore, the average total number of cells surviving (N_s) can be calculated using the LQ model by applying equation (2.3) as shown in (2.4)

$$N_s = N_0 e^{-(\alpha nd + \beta n d^2)} \tag{2.4}$$

Since the ratio of α and β is better known than the individual α and β values, equation (2.4) is rewritten as

$$N_s = N_0 e^{-(\alpha D(1+(d/\frac{\alpha}{\beta})))} \tag{2.5}$$

N_0 can be calculated as $\rho_{cl}V$. where ρ_{cl} is the clonogen density and V is the volume of the tumor.

Once the number of surviving cells are calculated, the probability for no single clonogenic cell survival will be given by Poisson statistics.

The probability distribution of a random Poisson variable X is given by the equation (2.6)

$$P(k) = \frac{\lambda^k e^{-\lambda}}{k!} \tag{2.6}$$

where k is a discrete stochastic variable with values 0,1,2,3.... and λ is the mean (expected) number of success in the time interval. In the context of radiotherapy, k=0 since the probability we are interested in is for "zero" surviving clonogens and the expected number of cells (λ) is equal to N_s.Thus equation (2.6) becomes

$$TCP = P(k = 0) = \frac{N_s^0 e^{-N_s}}{0!} = e^{-N_s} \tag{2.7}$$

2.1.2 Inter-patient radiosensitivity variation

As mentioned earlier the clinically observed DRCs (from analyzing patient treatment outcomes treated with different prescription doses) are shallower than observed by in vitro experiments. Numerous dose-response curves have been published in the literature [72–78]. None of these curves exhibit steepness such as that observed in invitro experiments. Many hypotheses have been proposed in the literature for the shallowness of the clinically observed DRCs [79, 80]. But the most credible is the inter-patient radiosensitivity of the tumor cells [79, 81–83]. The application of the TCP formalism in (2.7) produces a steep dose-response curve rather than a relatively shallow one. To account for the variation in the inter-patient radiosensitivity, equation (2.7) has been modified such that the TCP is calculated by averaging over a population of patients with "normally" distributed α with a standard deviation of σ_α. The TCP formalism accounting for inter-patient radiosensitivity is shown in equation 2.8. The dose-response curves generated for different σ_α is shown in figure 2.2. The distinct steepness for $\sigma_\alpha = 0$ can be noted, while other curves exhibit a relatively shallow dose-response curve. The slope of the dose-response curve decreases with increasing σ_α.

$$TCP = \frac{1}{\sigma_\alpha \sqrt{2\pi}} \int_0^\infty (\prod_i exp(-N_s) exp[-(\alpha - \bar{\alpha})^2)/2{\sigma_\alpha}^2] d\alpha \tag{2.8}$$

where σ_α is the standard deviation of radiosensitivity $\bar{\alpha}$ in a population of patients.

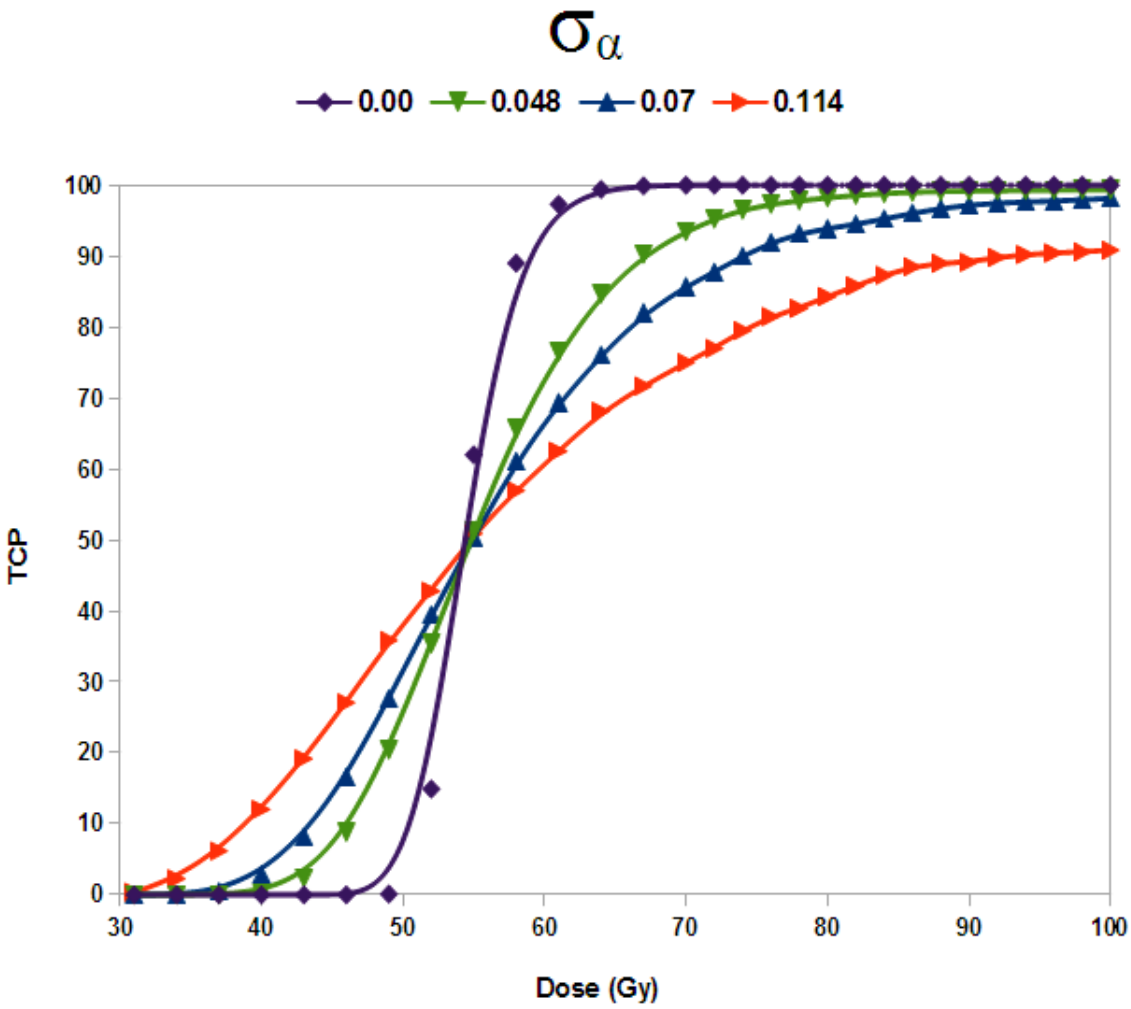

Figure 2.2: Dose-response curves for different σ_α. Other parameters used for the calculations are; $\bar{\alpha} = 0.3\,Gy^{-1}$, $\rho_{cl} = 1.0E7\,cc^{-1}$, α/β=10Gy and number of treatment fractions=20

.

2.1.3 Random sampling of α over Gaussian distribution

Accounting for inter-patient radiosensitivity can be done mathematically using equation (2.8); which uses a uniform sampling technique for the integration. However, it can also be randomly sampled over a Gaussian distribution of α; which is known as *Monte Carlo integration*. A comparison of both the methods is given in this section. TCP inclusive of inter-patient radiosensitivity using Monte Carlo integration is given by equation (2.9).

$$TCP = \frac{1}{n}\sum_{1}^{n} TCP(\alpha_n) \tag{2.9}$$

where α_n is the α value at n^{th} iteration randomly sampled from the Gaussian distribution of α characterized by σ_α. $TCP(\alpha_n)$ is calculated according to equation (2.7) by substituting α with α_n.

In a "normal" distribution of α, the range varies from $-\infty\, to\, +\infty$. However in reality, none of the patients would have a extremely low, high or negative radiosensitivity. Thus, the values are truncated on both sides of the Gaussian distribution around $\bar{\alpha}$ with a interval of $\bar{\alpha} \pm 2\sigma_\alpha$. The sampled α values falling outside the $\bar{\alpha} \pm 2\sigma_\alpha$ range are neglected in the Monte Carlo integration.

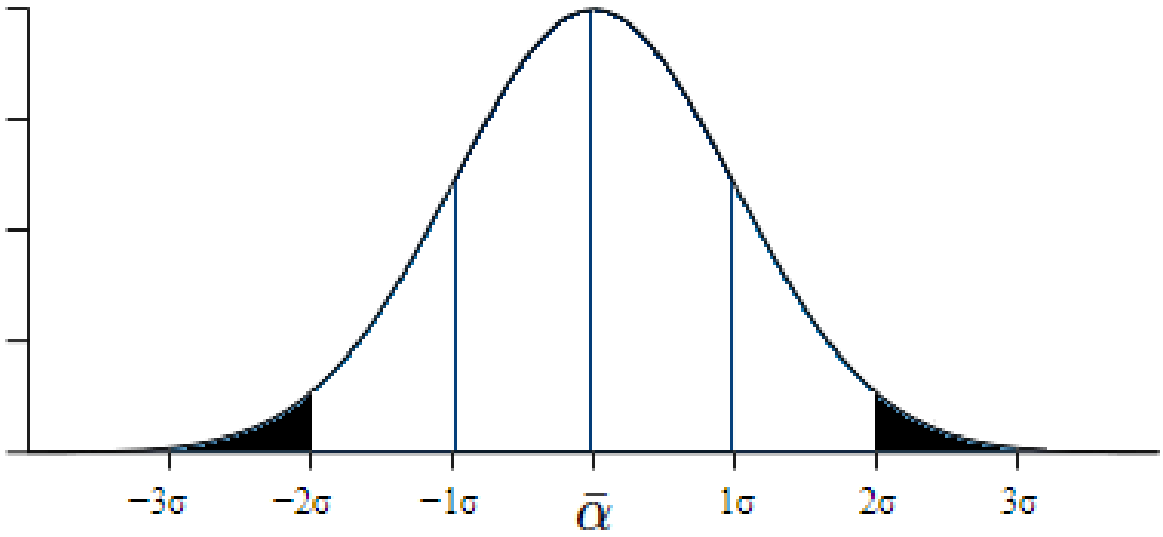

Figure 2.3: Clipped-Gaussian distribution of α. Only values in the white region of the bell curve are used in the calculations.

The TCP values calculated using both methods for different $\bar{\alpha}$ values at different dose levels (50, 60, 70 Gy) for three different σ_α values are shown in figure 2.4. Moreover, DRC produced with two integration methods are shown in figure 2.5 for σ_α of $0.07\, Gy^{-1}$.

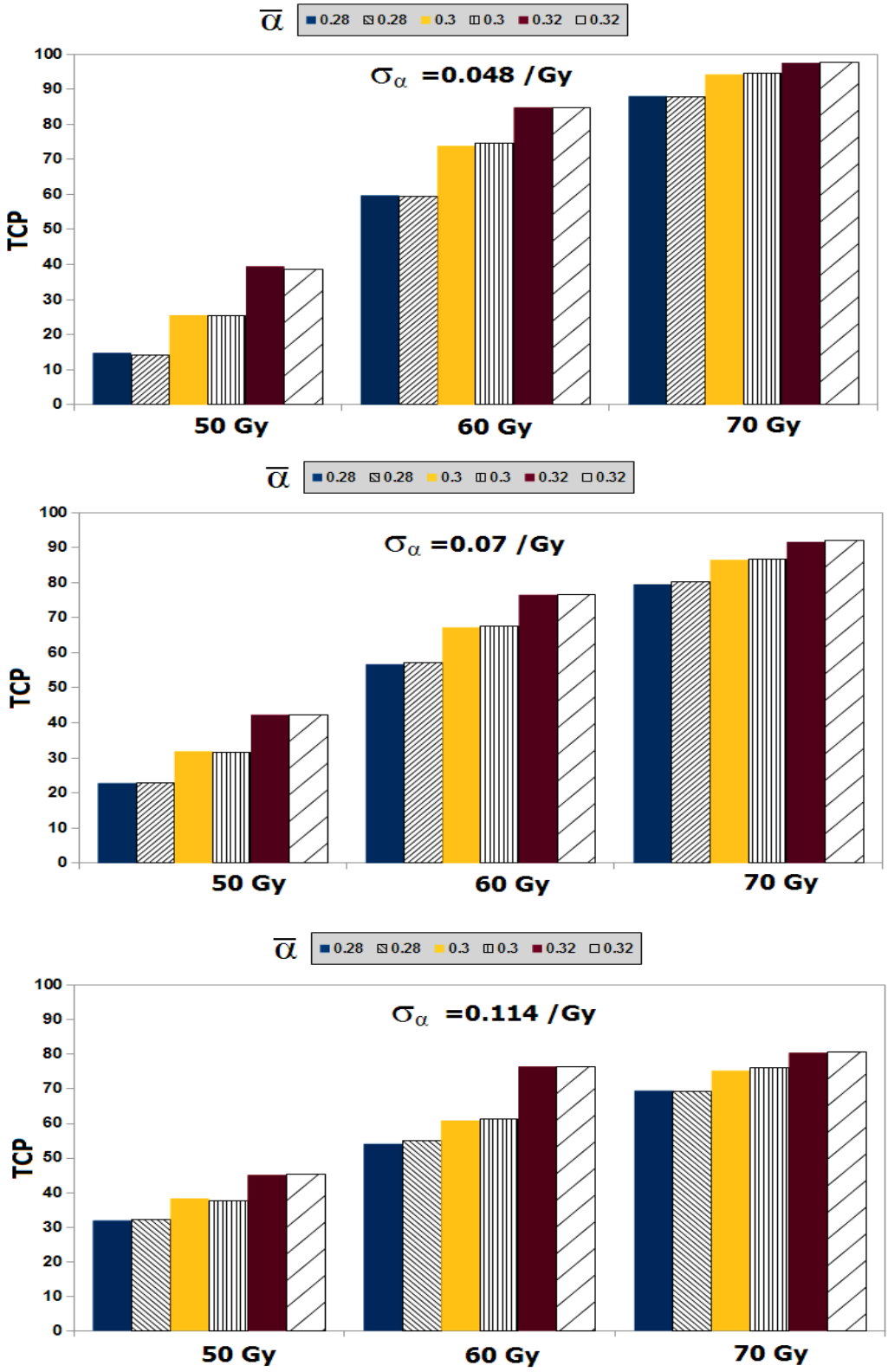

Figure 2.4: Random sampling vs Integrating over the Gaussian distribution of α. The hatched bars represent TCP values calculated by random sampling and the solid bars represent values calculated by averaging over the Gaussian α. TCP parameters are $\rho_{cl} = 1.0E7\, cc^{-1}$ and $\alpha/\beta = 10$.

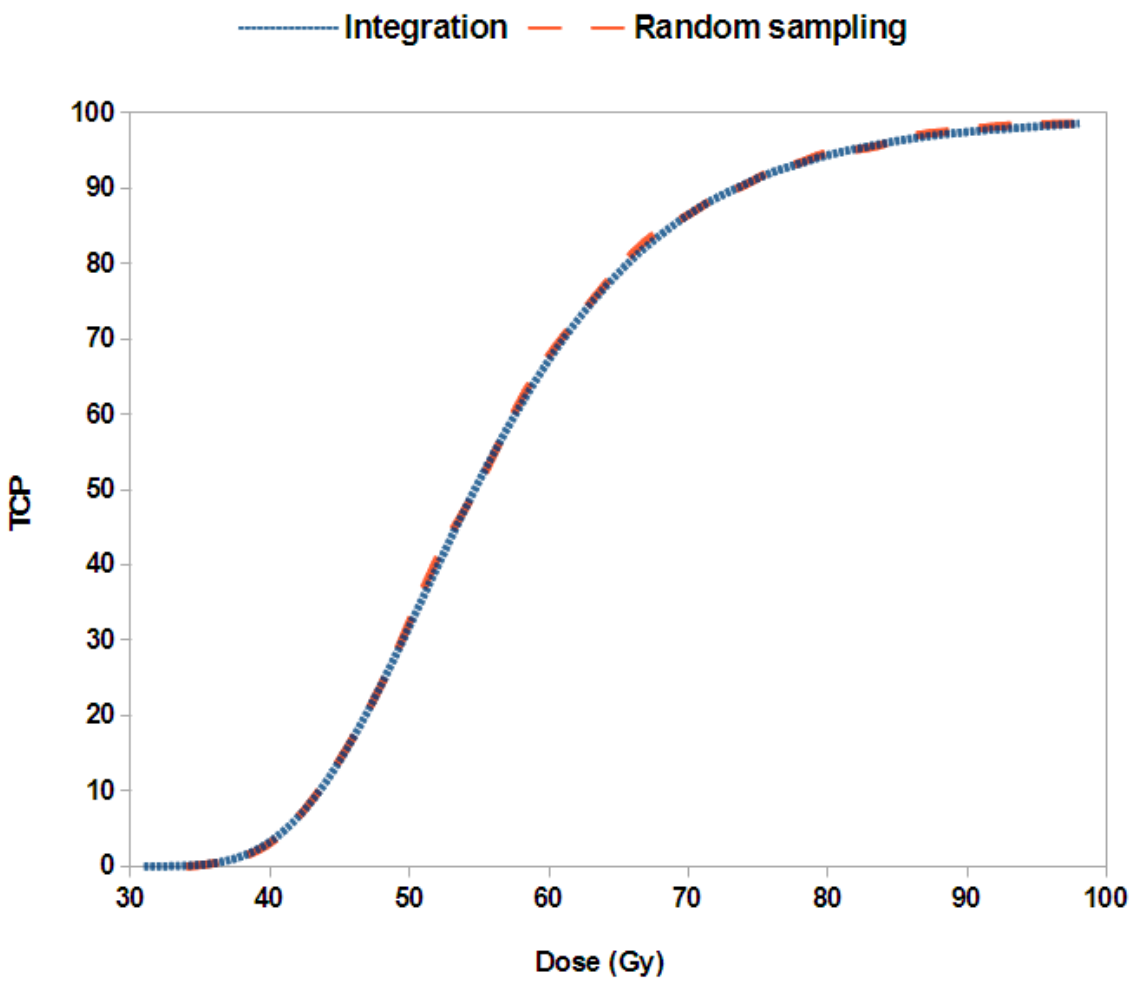

Figure 2.5: Dose-response curve generated by integration and random sampling methods of accounting for inter-patient radiosensitivity variation. The TCP parameters used in the calculations are $\bar{\alpha} = 0.30\,Gy^{-1}$, $\alpha/\beta = 10\,Gy, \sigma_\alpha = 0.07\,Gy^{-1}, \rho_{cl} = 1.0E7\,cc^{-1}$.

2.1.4 TCP calculation by dose summation and SF methods

TCP values inclusive of geometric uncertainties are calculated by summing the dose values for each fraction according to the displacement of the voxels. Since every voxel receives a different dose at each fraction, the biological effect of assuming that every voxel receives a uniform dose of $D_{mean}(i.e., D_{total}/n)$ every fraction is not radiobiologically accurate. However, it has been shown by Bortfeld *et al* that for fractionated treatments where the voxel doses vary moderately between fractions, the radiobiological effects resulting from dose summation or calculating the TCP by calculating the *surviving-fraction* (SF) each fraction are equivalent [84]. This consideration applies especially to tumor, which have higher α/β ratio than normal tissues which means that tumors are less sensitive to fraction size.Moreover, tumors experience relatively less dose variation due to displacements than OARs since tumors are surrounded by a relatively high dose region compared to OARs. This is demonstrated in figure 2.8, where

TCP values are calculated from the final summed dose values in each voxel and by calculating the SF in each voxel at every fraction. TCP calculation by the SF method is shown in figure 2.6. At the end of each fraction the number of surviving cells in each voxel is calculated and the total remaining cells in all voxels are summed to obtain the remaining number of cells in the tumor volume. Considerable difference can be found only at low TCP values (where the underdosing due to tumour displacements is high, leading to lesser TCP compared to the static tumour) between the two methods for both 20 and 3 fractions. Some studies have shown that the α/β ratio for prostate tumours can be as low as 3 Gy [85–88]. Hence, the effect of α/β is briefly studied for different standard deviations of systematic and random errors for high (10) and low (3.0) α/β ratios with a PTV margin of 6 mm. The description of the simulation process is shown in chapters 3 & 4. Other simulation parameters used are similar to the one used in margin determination study. The σ_α used is 0.114 Gy^{-1}. The results are given in table 2.1. To achieve the same TCP as with α/β of 10 Gy the α parameter is adjusted to acheive 50% TCP in the α/β of 3 Gy^{-1}. Thus is due to the fact that TCP parameters should always be fitted to the clinically observed treatment outcomes. The α/β parameter is found to have little impact on the TCP loss than σ_α since the relative drop in TCP is determined by the steepness of the dose-response curve which is determined by σ_α. The maximum deviation found between two α/β is 1.2%.

Table 2.1: TCP loss vs α/β ratios

Σ, σ	$10Gy(\alpha = 0.3\,Gy^{-1})$	3 Gy$(\alpha = 0.2\,Gy^{-1})$
1,1	50.0	50.0
2,2	50.0	49.2
3,3	41.83	41.3
4,4	27.30	26.10
5,5	14.81	15.26

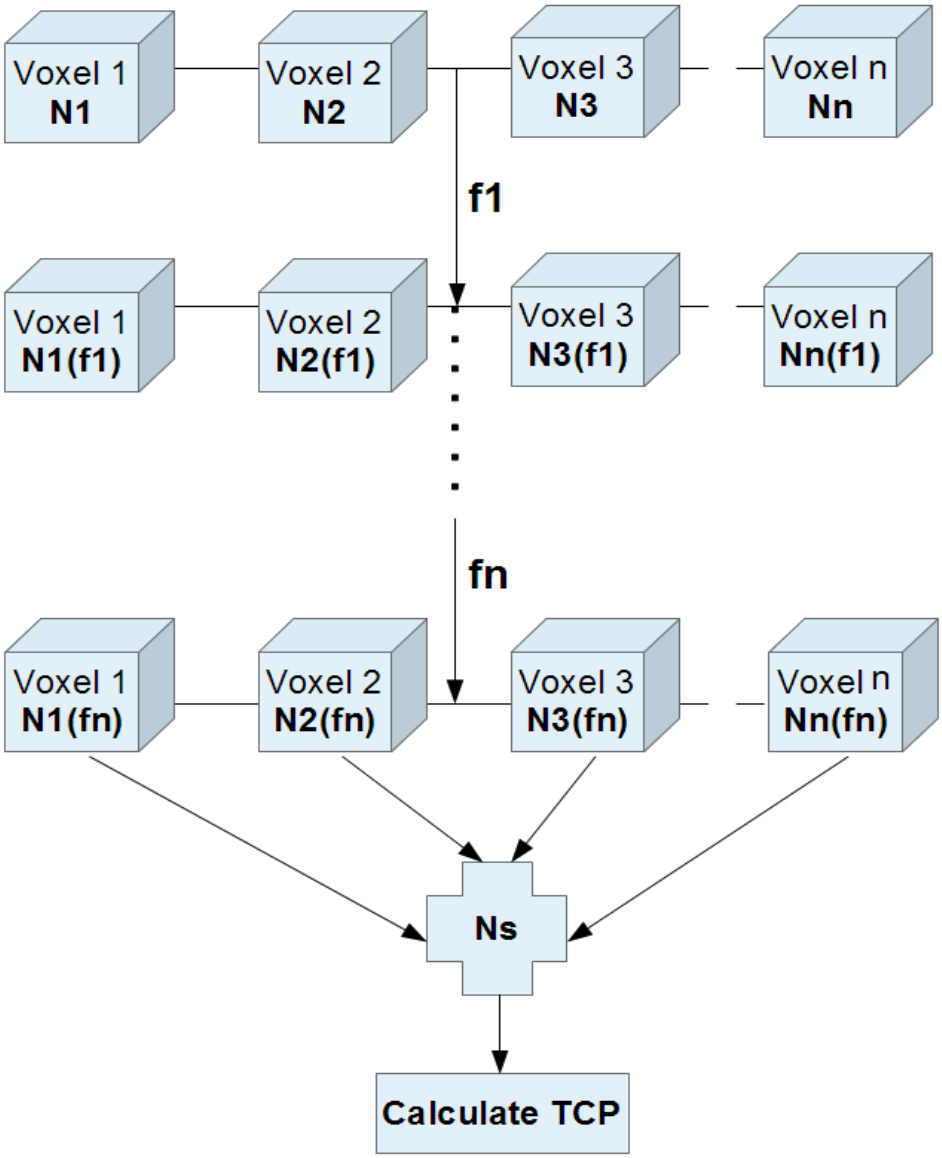

Figure 2.6: TCP calculation by SF method. N1,N2...Nn represent the initial number of clonogenic cells in each individual voxel *n*, whereas *f1,f2...* represent the fraction number. The number of surviving cells in each voxel is calculated at the end of each fraction and the total cells in each voxel are summed at the end of treatment to obtain the total number of remaining cells in the whole tumour.

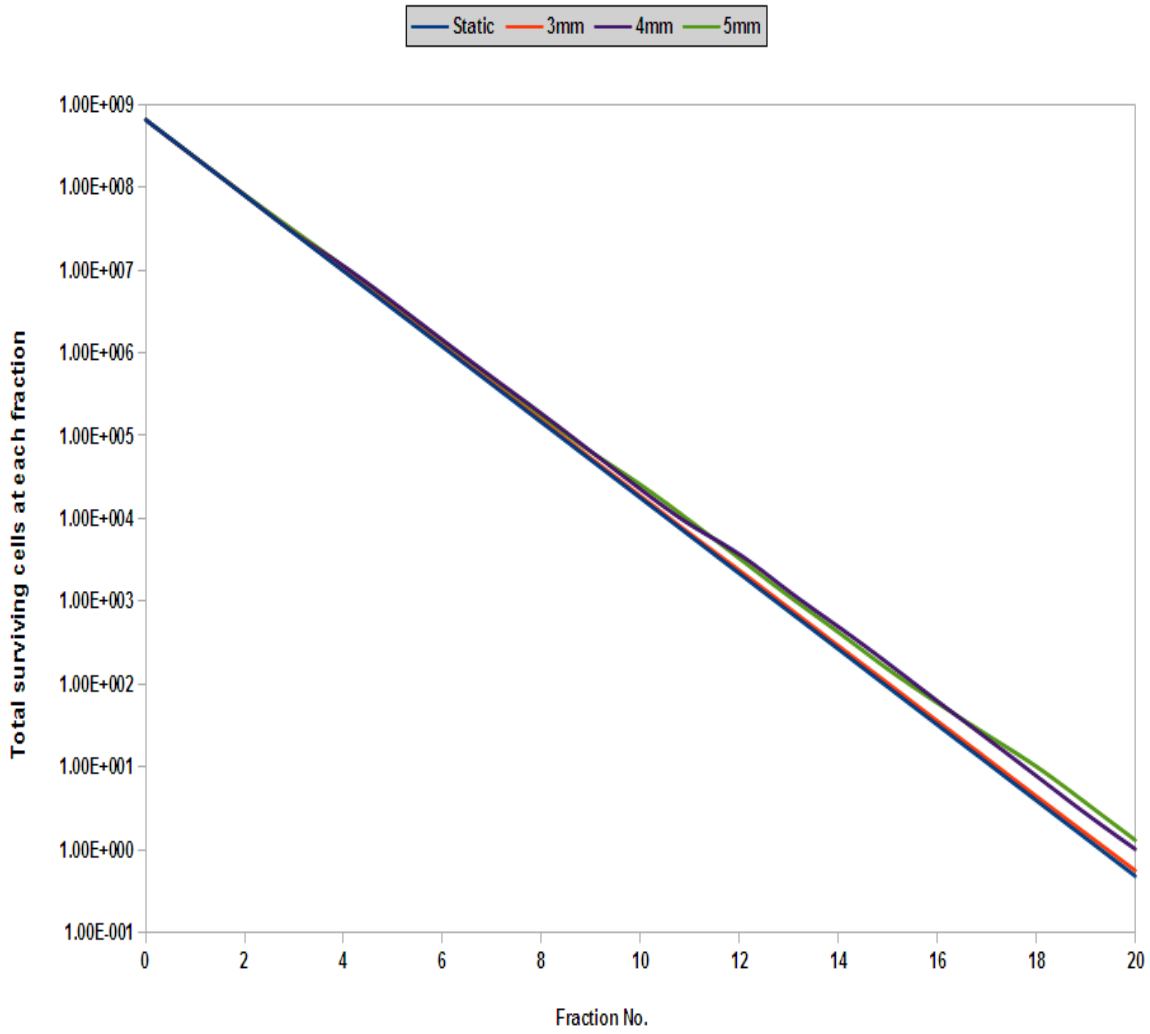

Figure 2.7: Total number of surviving cells at each fraction for different Σ and σ (Σ,σ=3,4, and 5 mm) compared with the static case. TCP parameters used for the calculations are; $\bar{\alpha} = 0.3\,Gy^{-1}$, $\rho_{cl} = 1.0E7\,cc^{-1}$, α/β=10Gy and number of treatment fractions=20.

The decrease in the total number of cells at each fraction is shown in semi-log plot in figure 2.7 for a 20 fraction treatment with different standard deviations of systematic and random errors. Figure 2.8 shows TCP calculated for 9 different simulations using SF and dose summation methods with systematic and random errors randomly drawn from their Gaussian distributions. Σ,σ=3 and the TCP parameters are same as used in generating plots in figure 2.7.

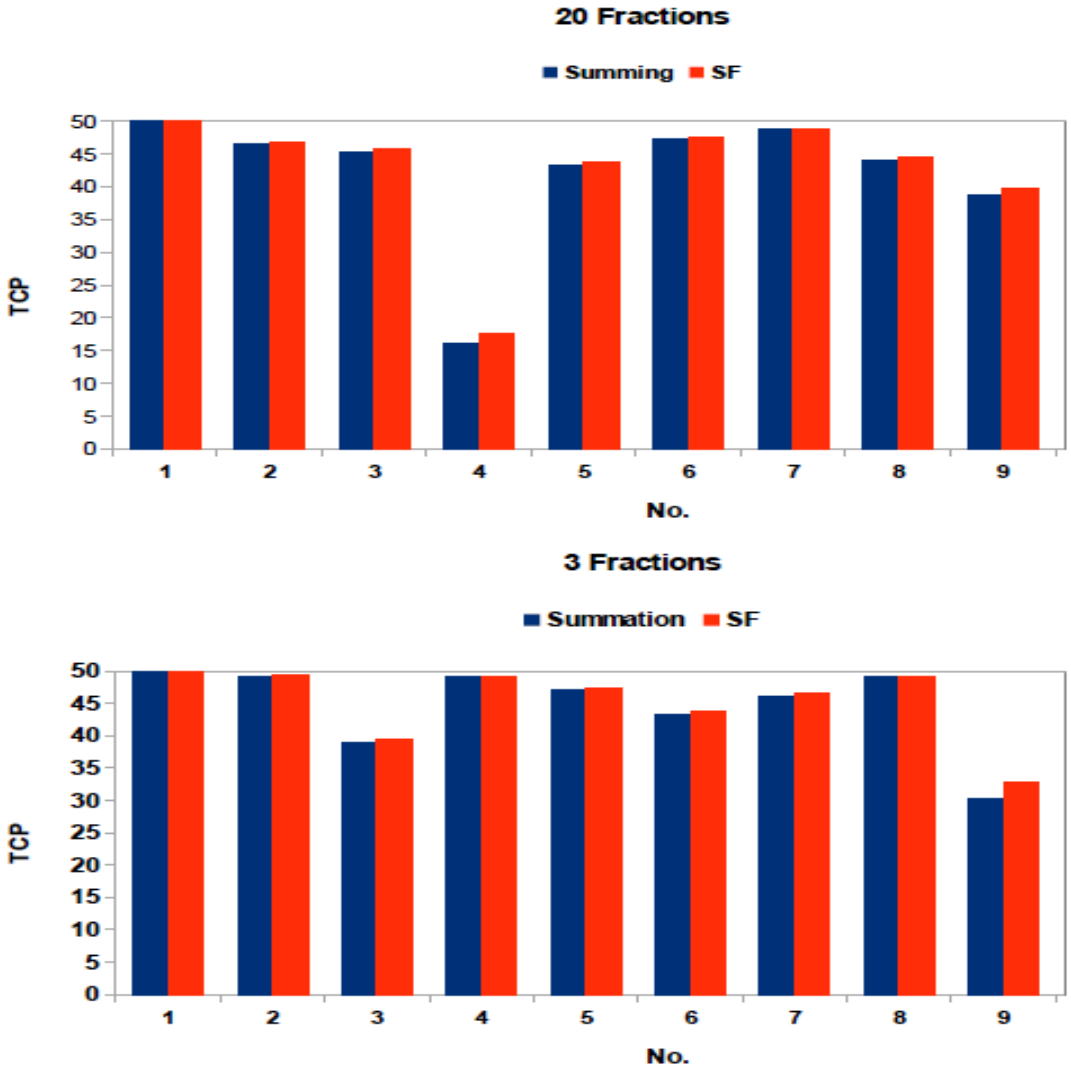

Figure 2.8: Comparison of TCP calculation by dose summation and SF methods for nine different simulations.

2.1.5 Mean population TCP calculation

Most of the results in this thesis are evaluated on the basis of population mean TCP ($\overline{TCP}_{pop}$), which provides the mean of the TCP_{pop}(inclusive of inter-patient radiosensitivity variation) values calculated from a large number of TCP values generated from the simulations for each plan. The population mean TCP is calculated as shown in equation 6.23.

$$\overline{TCP}_{pop} = \frac{1}{n}\sum_{1}^{n} TCP_{pop} \tag{2.10}$$

where n is the number of simulations.

Chapter 3

Biosim: A software program for simulating geometric uncertainties and interplay effect

3.1 Introduction

Biosim is an in-house developed modular software written in C++ for the purpose of simulating the radiobiological effect of geometric uncertainties, variation of clonogen density in the tumour and the interplay effect in step-and-shoot IMRT treatments. In the current version, it supports the Millennium120 multi-leaf collimator (MLC) (Varian Medical Systems, Palo Alto, CA) for simulating interplay effect and visualizing the beam's eye view (BEV), but it can be easily extended to other MLCs. Visualization Tool Kit (VTK) is used for image processing and 3D visualization and the open source edition of Qt is used for developing the graphical user interface [89]. Biosim can read DICOM CT images, RT structure sets, RT Dose and RT plans using the GDCM DICOM toolkit [90]. Moreover, a cubical phantom with a user-specified uniform Hounsfield unit (HU) can be generated along with other standard shapes such as spheres, cylinders and cubes with user specified dimensions as volumes-of-interest (VOI). Dose-volume histograms (DVH) can be independently calculated for the VOIs. Dose can be either imported from TPS in DICOM format or a spherical dose distribution can be generated with a Gaussian penumbra. However, for studying the interplay effect a ray-tracing based dose model is used. The "Enhanced Marsden" model is used to calculate TCP to take account of geometrical uncertainties and interplay effect.

3.2 VTK

VTK is an open-source object-oriented c++ class library for 3D computer graphics , visualization and image processing [91]. It offers a variety of algorithms to visualize

scalars, vectors, tensors and volume rendering of 3D medical datasets such as CT and MRI. It also offers many modelling techniques such as mesh generation, mesh smoothing, polygon reduction, cutting, clipping and triangulation to mention a few of them.

3.2.1 Rendering in VTK

VTK uses a pipeline architecture connecting multiple elements such as data sources, filters, mappers and renderer to render the data into the render window. A typical VTK rendering pipeline is shown in figure 3.1. Filters operate on the source data and produce an output different from the source data then the modified output is processed through the mapper which converts the data into graphics primitives (actors) to be rendered into the render window by the renderer.

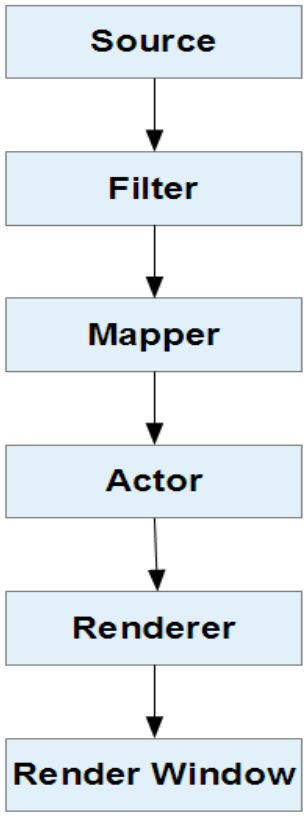

Figure 3.1: Typical rendering pipeline in VTK

3.2.2 VTK Image Data

Imported DICOM CT images and manually created phantom images are represented internally as vtkImageData(a special vtk class) with attributes such as spacing, origin, dimension and data type in Biosim. The vtk coordinate system with the image data is shown in figure 3.2. vtkImageData is a 3D matrix of uniform spacing along the

individual axes, but can be different on each axis. The first voxel of the vtkImageData is at the lower left corner of the image; with k increasing into the screen. If the index (i,j,k) of the specific voxel in image coordinates is known then its world coordinates (x,y,z) can be calculated using the information in the vtkImageData class as shown in equation (3.1)-(3.3).

$$x = O_x + i * S_x \tag{3.1}$$

$$y = O_y + j * S_y \tag{3.2}$$

$$z = O_z + k * S_z \tag{3.3}$$

where $O_{(x,y,z)}$ is the origin and $S_{(x,y,z)}$ is the spacing of the image data in their corresponding axis.

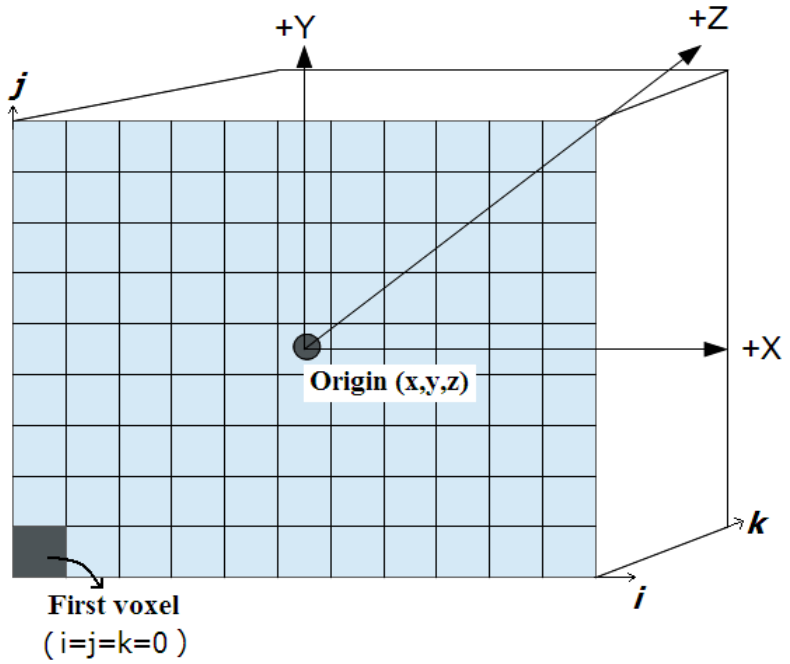

Figure 3.2: VTK world (x-y-z) and image (i-j-k) coordinate system with vtkImageData

3.3 Importing DICOM datasets

As mentioned earlier, Biosim can import CT, RTDOSE, RTSTRUCT and RTPLAN and cumulative DVHs in DICOM format. A c++ class named as "DCMImporter" has been developed for this purpose. Some of the relevant DICOM tags used for processing the DICOM data are given in table 3.1.

Table 3.1: DICOM Tags used for processing RT dataset

Modality	Tag Name	Tag Value
RTPLAN	Dose reference sequence	0x300a,0x0010
RTPLAN	Fraction group sequence	0x300a,0x0070
RTPLAN	Beam control sequence	0x300a,0x00b0
RTPLAN	Beam limiting device sequence	0x300a,0x011a
RTPLAN	Control point sequence	0x300a,0x0111
RTPLAN	Plan label	0x300a,0x0002
RTPLAN	Fractions planned	0x300a,0x0078
RTPLAN	Machine name	0x300a,0x00b2
RTPLAN	Beam Name	0x300a,0x00c2
RTPLAN	Beam type	0x300a,0x00c4
RTPLAN	Beam Energy	0x300a,0x0114
RTPLAN	Beam Angle	0x300a,0x011e
RTPLAN	Collimator Angle	0x300a,0x0120
RTPLAN	Couch Angle	0x300a,0x0122
RTPLAN	SSD	0x300a,0x0130
RTPLAN	FieldSize, MLC leaf positions	0x300a,0x011c
RTPLAN	Isocentre	0x300a,0x012c
RTPLAN	Meter set (MU)	0x300a,0x0086
RTPLAN	Beam Dose	0x300a,0x0084
RTDOSE	Dose gride scaling factor	0x3004,0x000e
RTDVH	DVH sequence	0x3004,0x0050
RTDVH	DVH type	0x3004,0x0001
RTDVH	Referenced ROI no.	0x3006,0x0084
RTDVH	DVH bins	0x3004,0x0056
RTSTRUCT	ROI sequence	0x3006,0x0020
RTSTRUCT	ROI contour sequence	0x3006,0x0039
RTSTRUCT	Struct set label	0x3006,0x0002
RTSTRUCT	ROI No.	0x3006,0x0084
RTSTRUCT	ROI color	0x3006,0x002a
RTSTRUCT	ROI name	0x3006,0x0026
RTSTRUCT	ROI type	0x3006,0x00a4
RTSTRUCT	Contour data	0x3006,0x0050
RTSTRUCT	Contour slice data	0x3006,0x0050

3.4 Graphical User Interface

Biosim provides four sub windows in a multiple document interface area for viewing axial, sagittal, coronal and 3D views of the ROIs, beams and dose. The axial, sagittal and coronal windows contain a vertical slider to slice through the dataset in their corresponding axis. BEV can also be viewed for co-planar gantry angles. The details of the imported plans are shown in a resizable table format. The details of the imported structures and some general information are provided in a structured tree format.

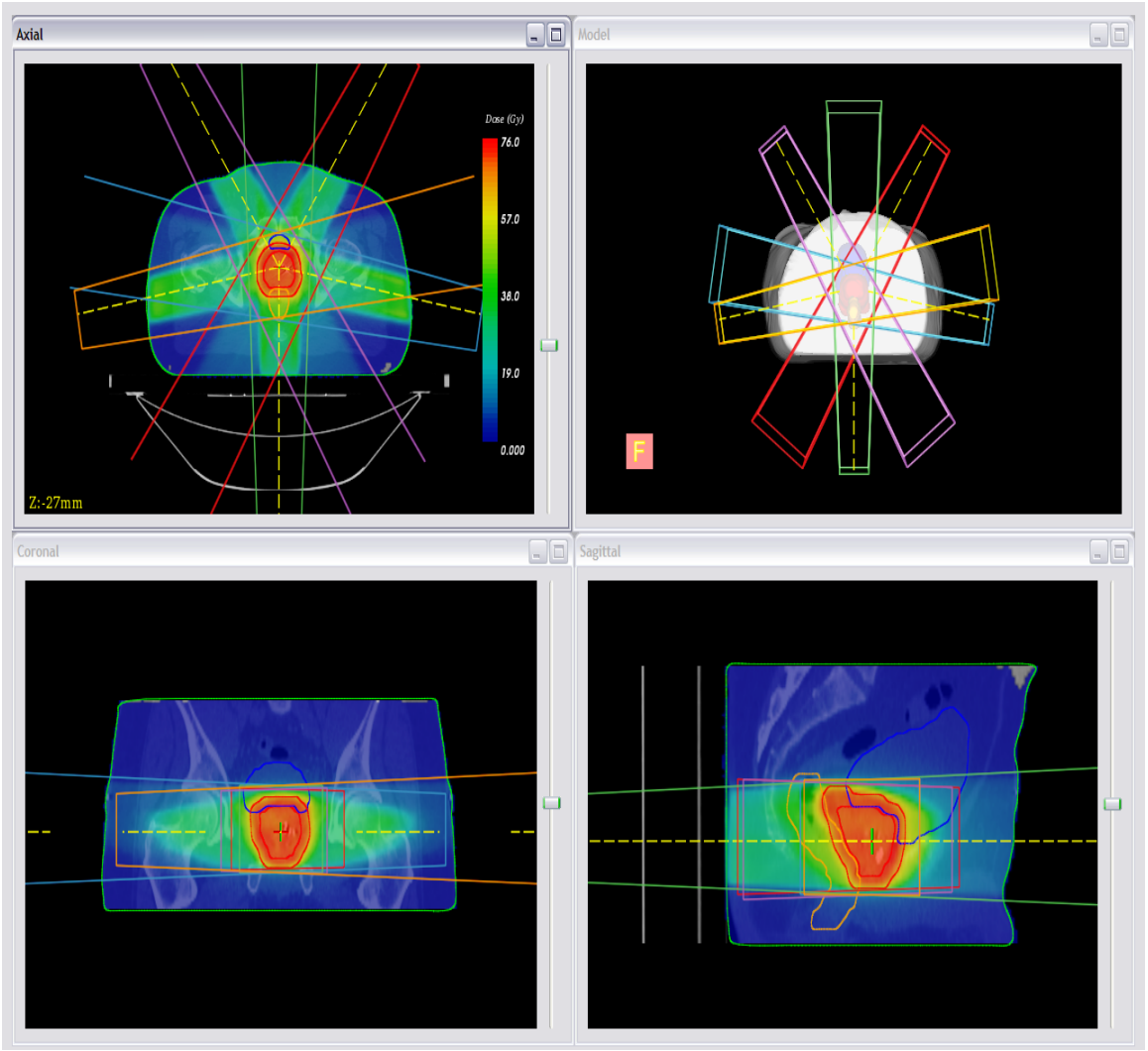

Figure 3.3: GUI with axial, sagittal, coronal and 3D views

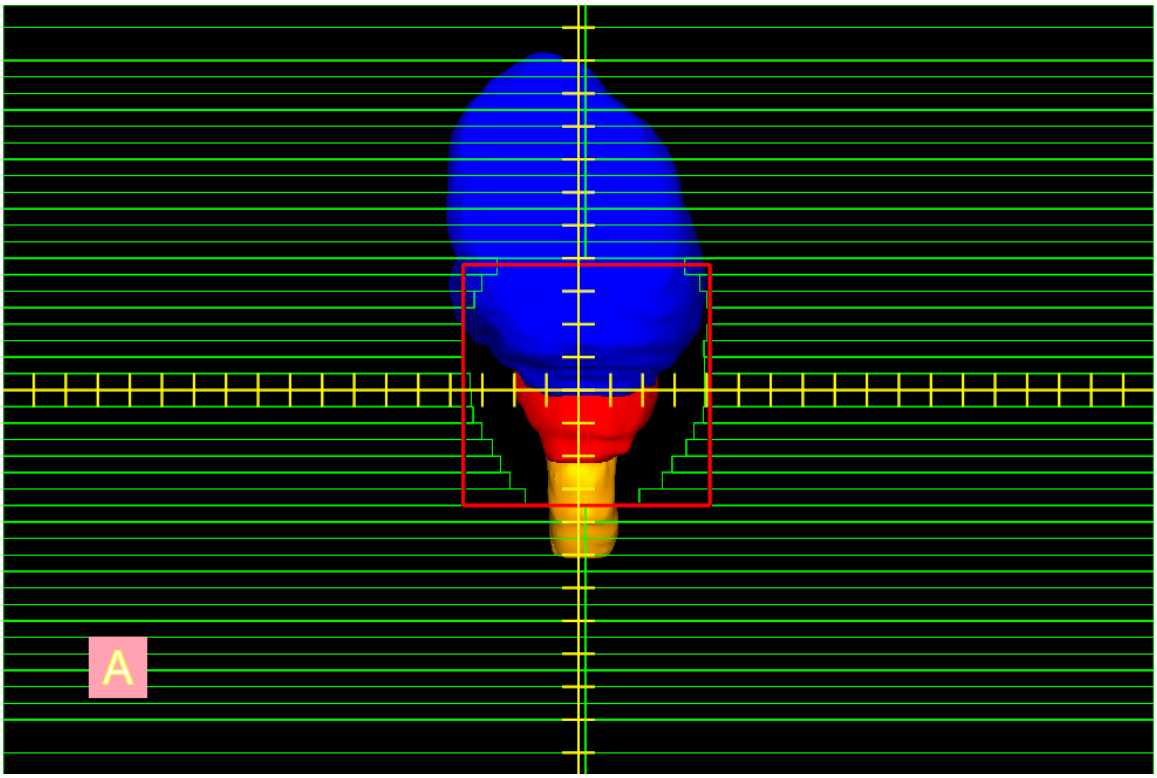

Figure 3.4: BEV for 0^o gantry angle with bladder, rectum and prostate shown in blue, yellow and red respectively.

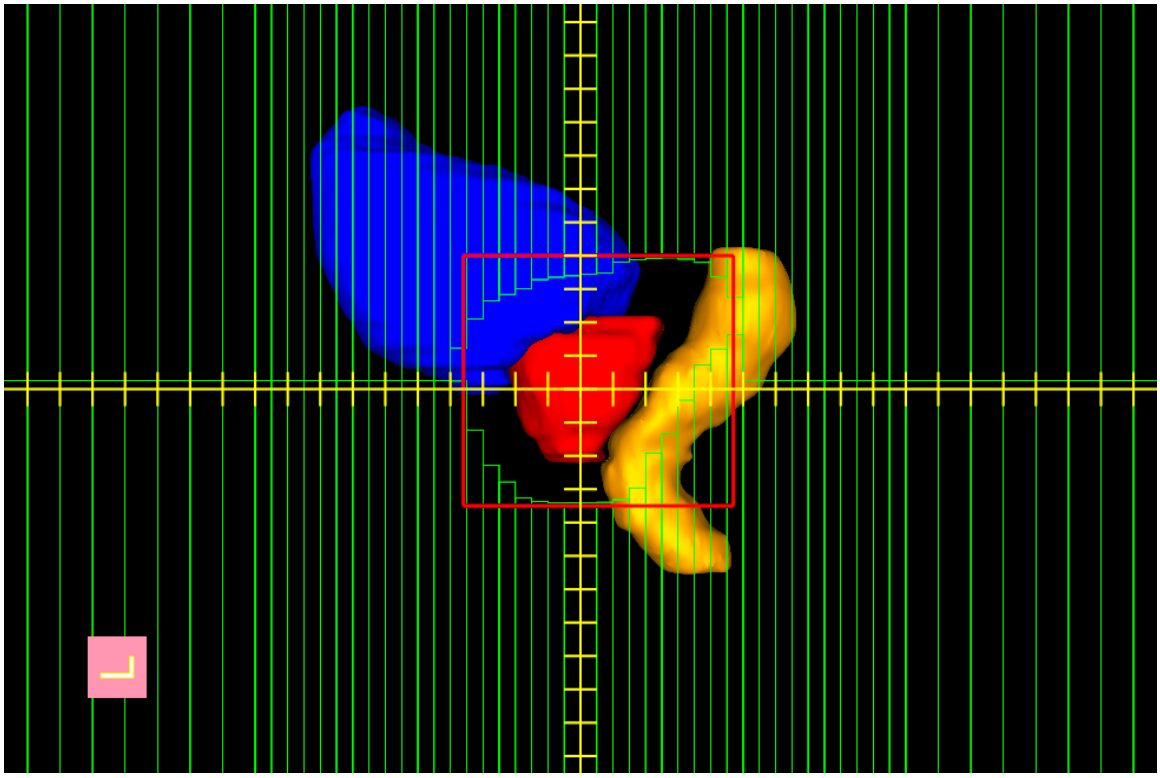

Figure 3.5: BEV for 90^o gantry angle with bladder, rectum and prostate shown in blue, yellow and red respectively.

3.5 Mesh generation

Figure 3.6 shows the steps involved in generating a 3D surface mesh using the Marching Cubes algorithm in VTK. Some of the generated meshes can be seen in figures 3.4 and 3.5 in the BEV.

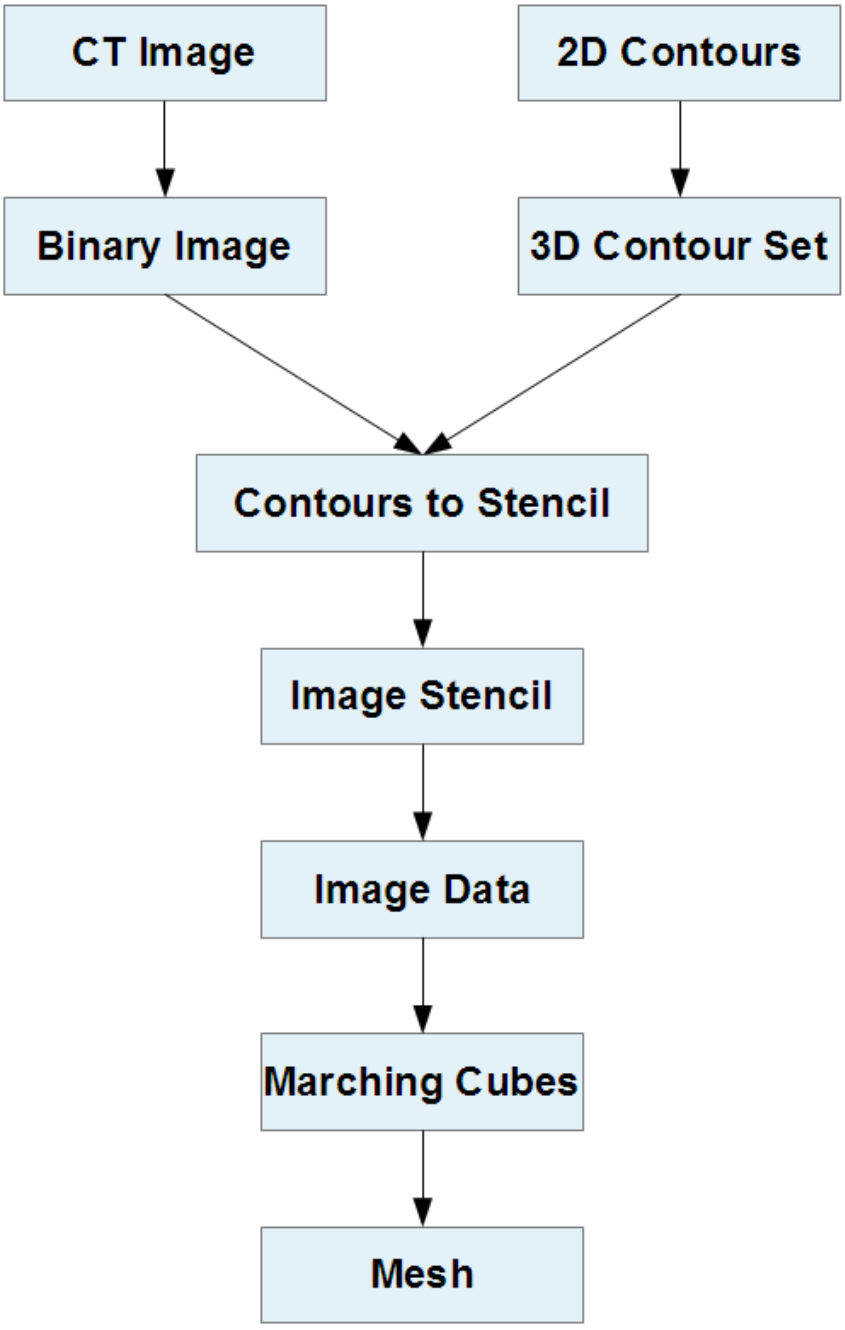

Figure 3.6: General steps in generating a mesh in VTK

3.6 Anisotropic margin growing algorithm

Structures can be anisotropically expanded or contracted in Biosim with user-specified margin in each axis. The general steps involved in margin growing are shown in figure 3.9. Structure contraction can be achieved with the same methodology as shown in figure 3.9,except by inverting the binary image of the triangular mesh (with "0" inside and "1" outside).

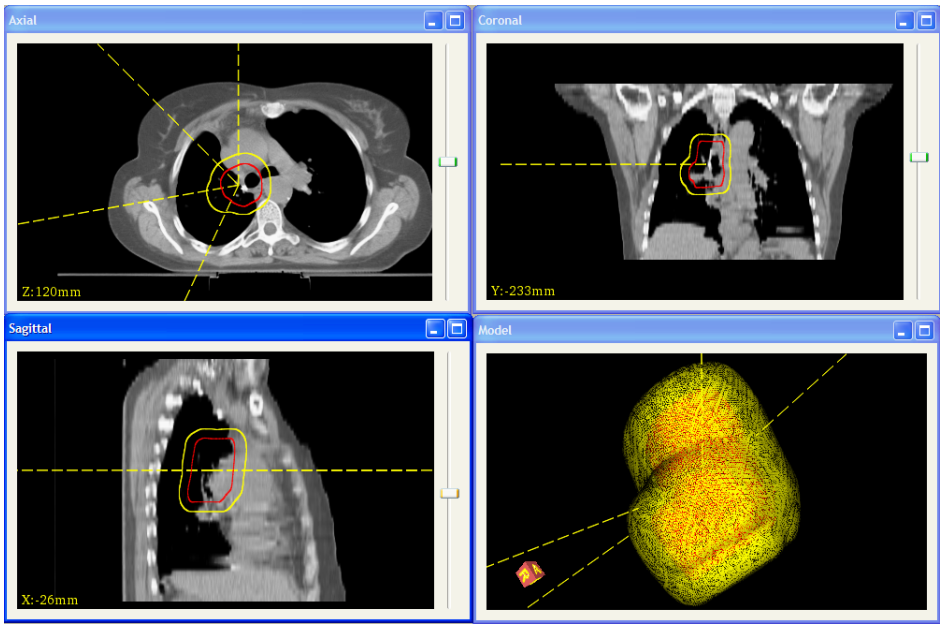

Figure 3.7: CTV (red) margin expanded 10mm isotropically (yellow)

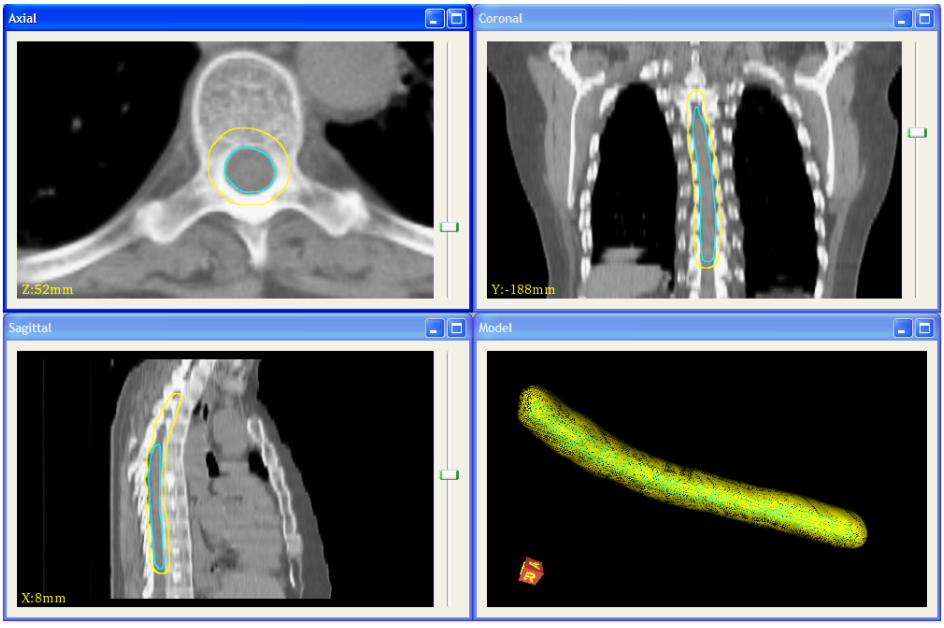

Figure 3.8: Spinal cord (cyan) expanded 5mm istropically (yellow)

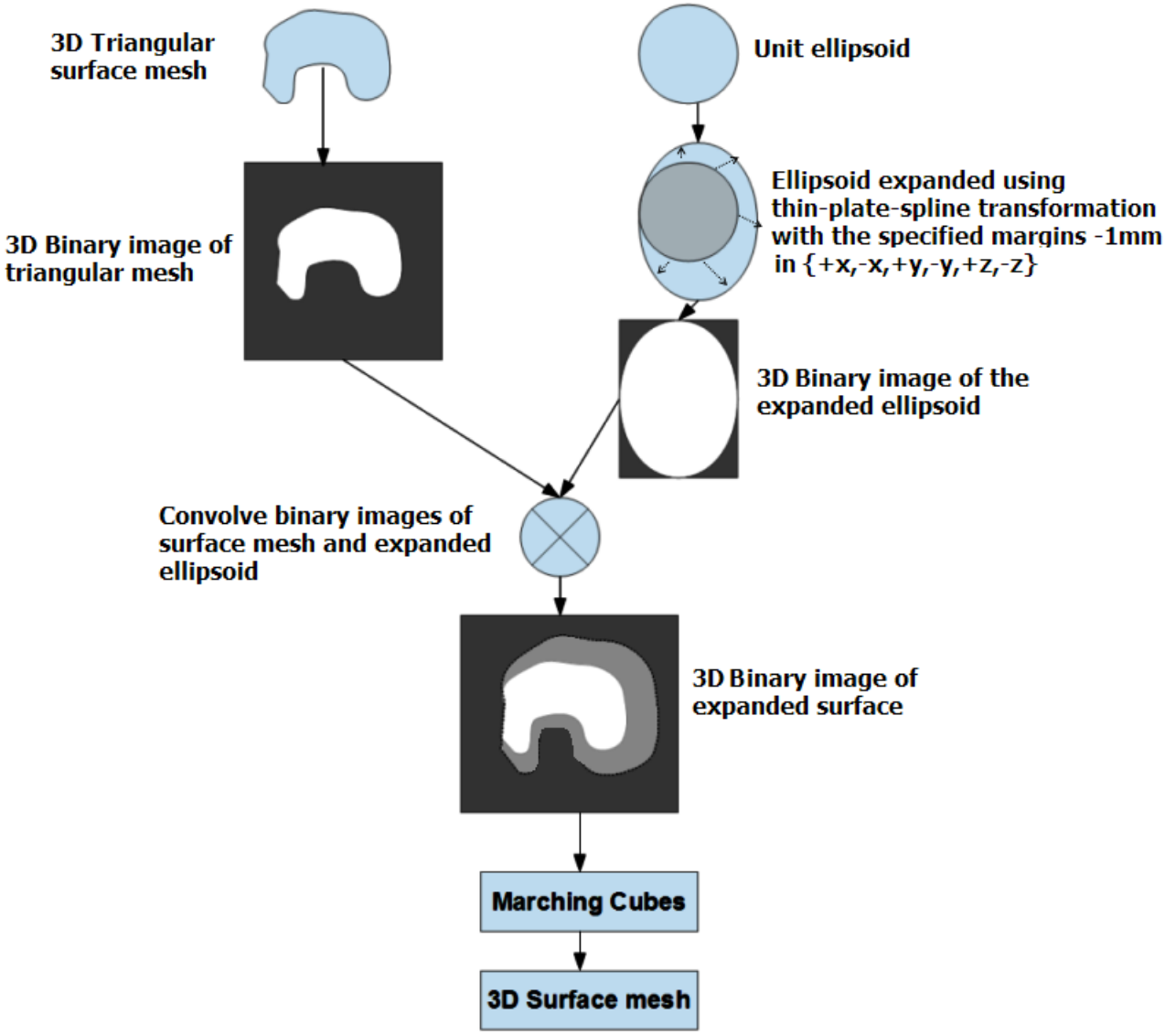

Figure 3.9: Steps involved in anisotropic margin expansion

3.7 DVH Calculation

DVHs are calculated using some of the classes in VTK with some additional functions in Biosim. In radiotherapy planning, the 3D shape of the structures is generally derived from a set of 2D contours drawn on the axial CT images. A surface mesh of the structure is generated from the set of 2D contours using vtkMarchingCubes for the structure-of-interest, and the resulting mesh is stored as a vtkPolyData. The dose calculated within the patient volume by the TPS is a 3D array with a commonly-used resolution of 2-to-3 mm. This 3D dose array is generally a matrix of uniform spacing in all three axes, which can be imported into Biosim as vtkImageData. The key step in calculating the DVH is to identify the voxels inside the structure-of-interest. This can be achieved with a combination of some of the VTK classes, namely vtkPolyData-

ToImageStencil and vtkImageStencil. The dose outside the structure is set to zero using SetBackgroundValue in vtkImageStencil. Then, the voxels inside the structure can be easily identified by iterating over the binary image matrix. The entire dose array and dose extracted for bladder using vtkPolyDataToImageStencil is shown on an axial slice in figures 3.10 and 3.11 respectively.

Figure 3.12 shows the steps involved in calculating differential DVH in VTK. A representative differential DVH calculated for tumour is shown in figure 3.12.

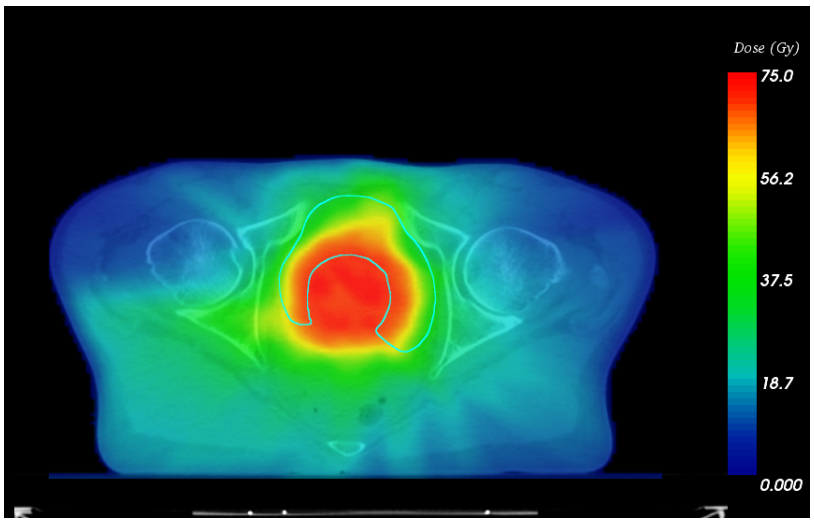

Figure 3.10: Dose grid with bladder contour

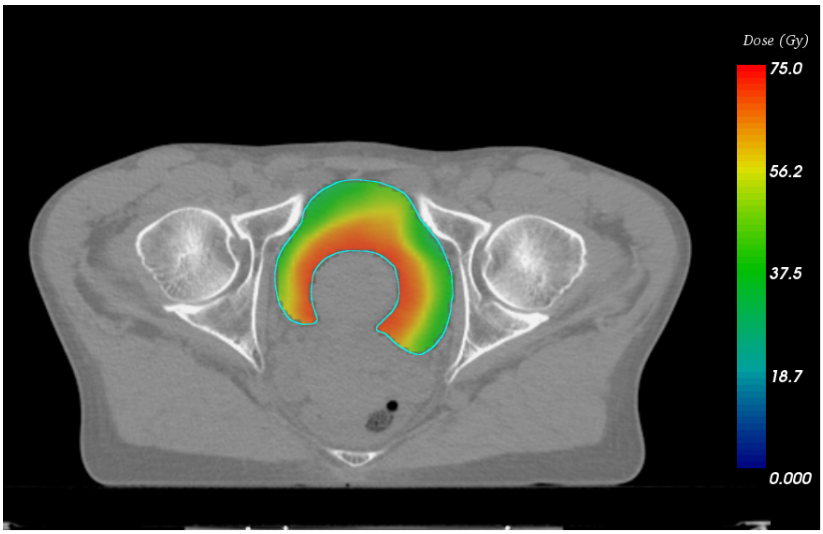

Figure 3.11: Dose extracted with bladder contour

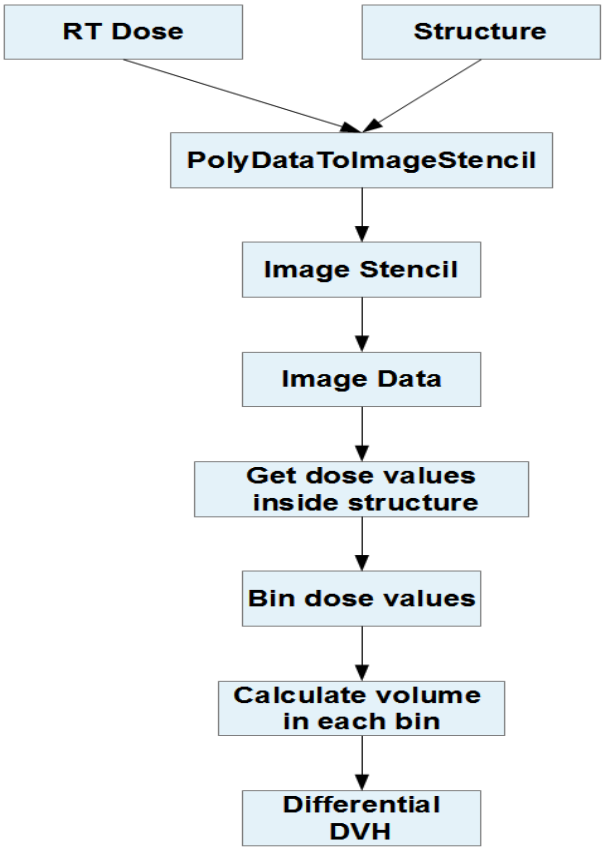

Figure 3.12: General steps in calculating a differential DVH in VTK

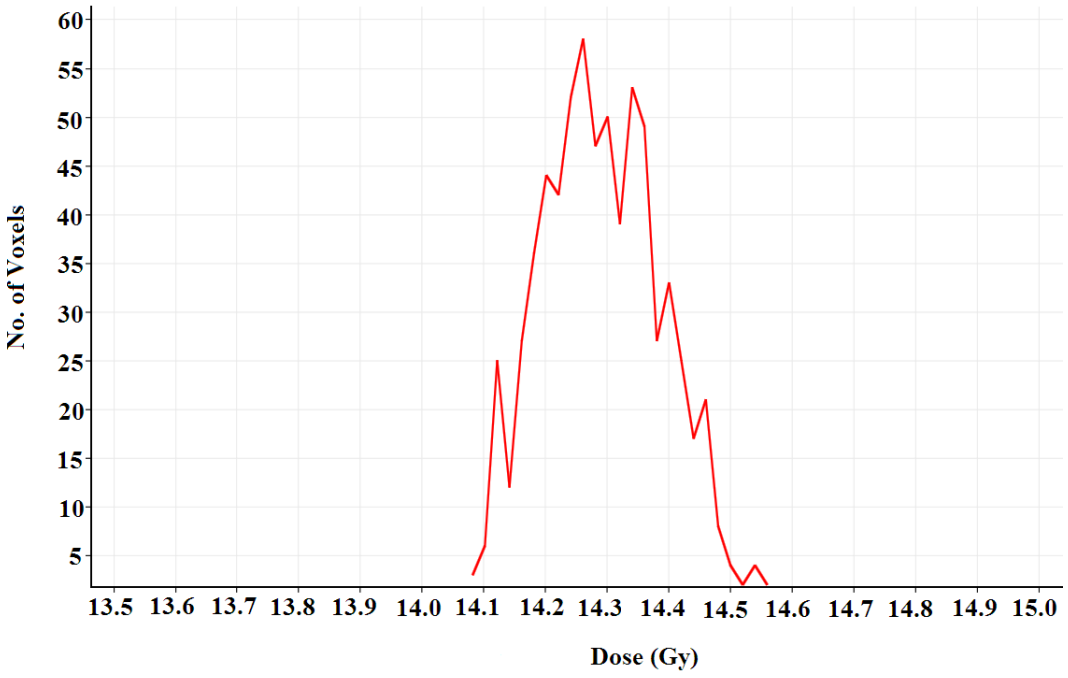

Figure 3.13: Differential DVH for a tumour calculated in Biosim

The DVHs calculated using Eclipse^{TM}(Varian Medical Systems,Palo,Alto) and Biosim are shown in figure 3.14 and 3.15 for a prostate and breast case respectively.

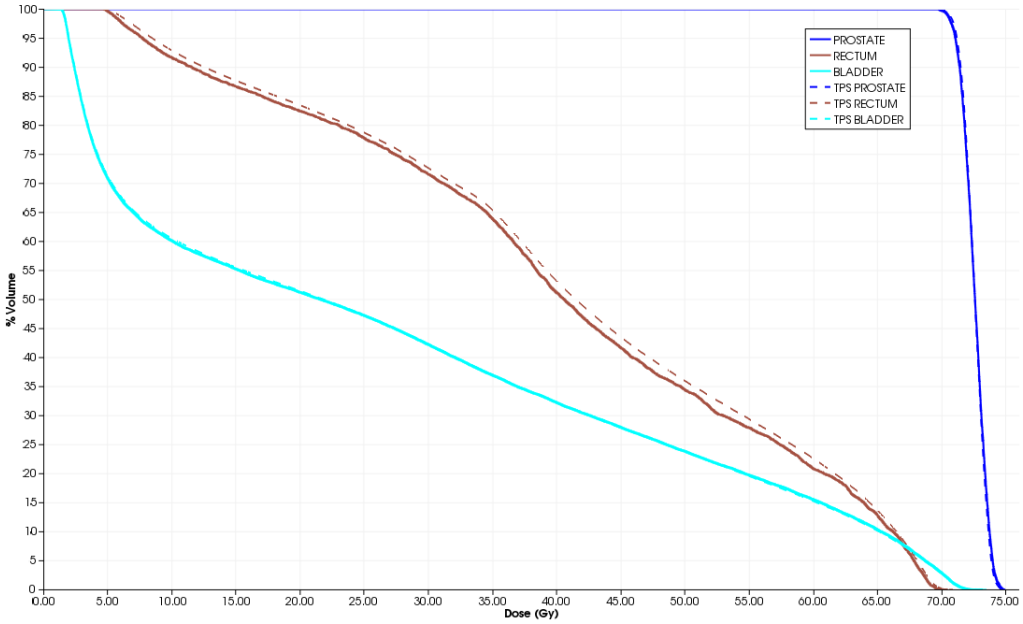

Figure 3.14: Cumulative DVHs calculated in Biosim compared with Eclipse^{TM} DVHs for prostate case

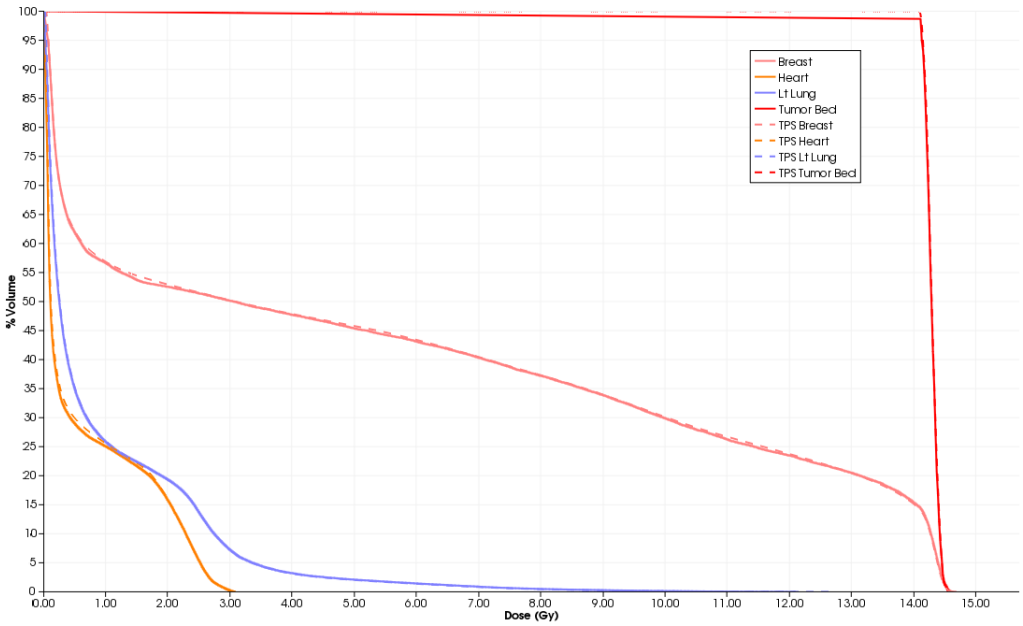

Figure 3.15: Cumulative DVHs calculated in Biosim compared with Eclipse^{TM} DVHs for breast case

3.7.1 Volume calculation in Biosim

The volume for the given structure is calculated as the number of voxels times the voxel volume. The volume calculated using VTK and analytical methods for a sphere (25 mm radius), cube (25 mm sides), and cylinder (25 mm radius and 40 mm length) are shown for 1 mm and 2.5 mm resolution of dose matrices in figure 3.16. The results are closer to the analytical method for 1mm resolution because of the reduced partial-volume effect.

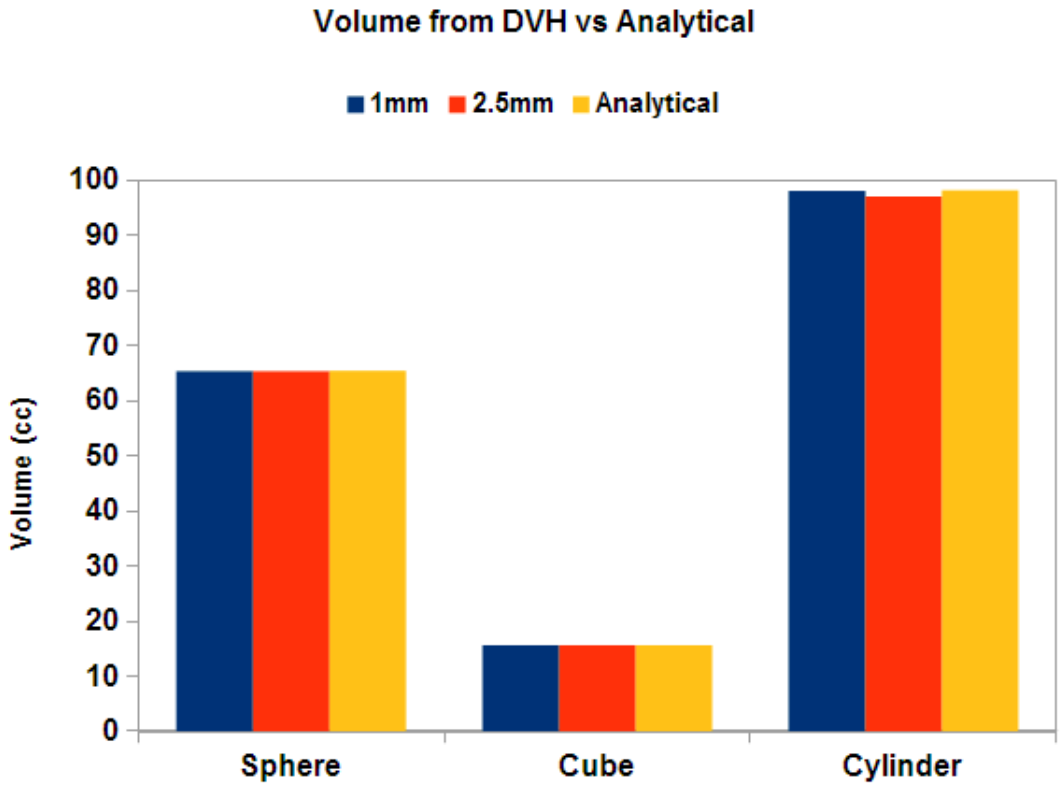

Figure 3.16: Volume calculation compared with analytical methods

3.8 Spherical dose distribution

A spherical dose distribution with a Gaussian penumbra can be generated with a user specified standard deviation as shown in figure 3.17. To generate such a distribution; the selected structure of interest (PTV) is expanded 5mm (where the 50% isodose surface will be placed) and 'flood filled' with a uniform value. This binary image is then convolved with a 3D Gaussian kernel to obtain the dose distribution. It is also possible to generate dose distributions with different penumbra widths along different axes, but a uniform penumbra width (same σ) is used through out the work carried out in this thesis using spherical dose distributions. A σ of 3.2 mm is used which results in 5mm between the 95% and 50% isodose surfaces.

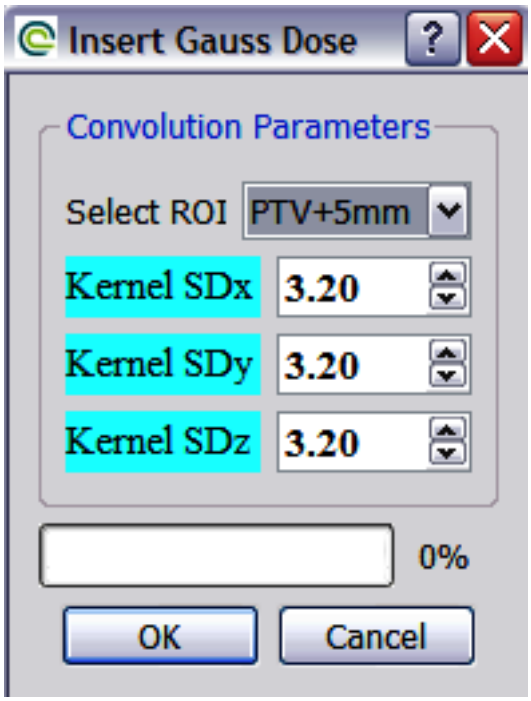

Figure 3.17: Gaussian convolution kernel parameters dialog with standard deviations set in each axis (3.2 mm)

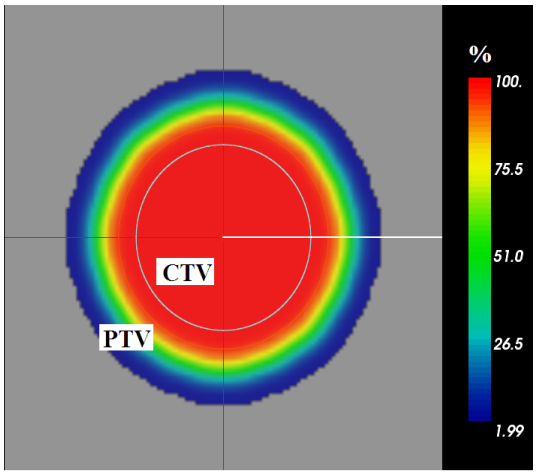

(a) Dose colour wash on central axial slice

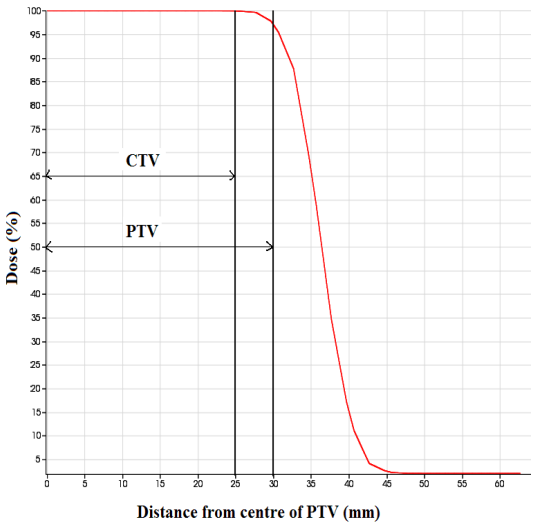

(b) Dose profile across PTV (white line shown in figure a). The ∼ 95% covers the PTV whereas the CTV receives 100% dose

Figure 3.18: Dose color wash and the dose profile across the PTV

3.9 Four-field brick dose distribution

To simulate a conventional four-field brick plan, a 3D matrix is filled with uniform value, in the shape determined by the jaw aperture. The beam divergence is calculated by assuming a source-to-axis distance (SAD) of 100 cm. This matrix is convolved plane-by-plane from top to bottom by a Gaussian kernel (σ=0.8 mm) to achieve a penumbra width of ∼6 mm at the isocentre level. A Collimator leakage of 0.5% is assumed outside the field. The resulting dose distribution and the percentage depth dose curve for the anterior field is shown in figure 3.20a and 3.20b respectively. The 2D Gaussian kernel is shown in figure 3.19. Tissue-maximum ratio (TMR) values for a 6MV beam taken from BJR supplement 25 [92] for the respective field size are used to calculate the dose in each voxel. Three more dose matrices are generated by applying matrix rotations of 90,180 and 270 degrees about the isocentre. The dose distribution for a four-field box is generated by summing all four matrices and normalized at the isocentre. The resulting dose distribution for 5x5 cm^2 anterior field is shown in figure 6.12. The cross profile at the isocentre level is shown in figure 3.21.

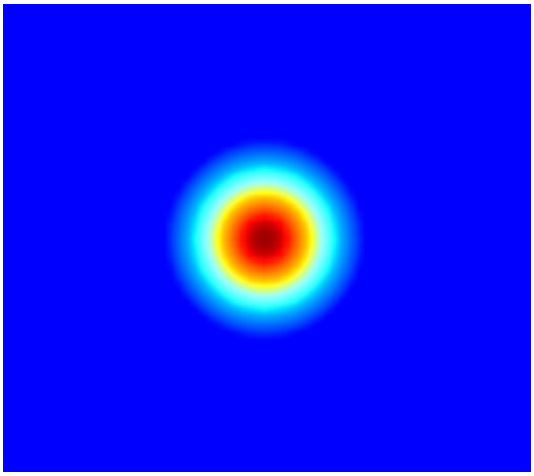

Figure 3.19: 2D Gaussian kernel

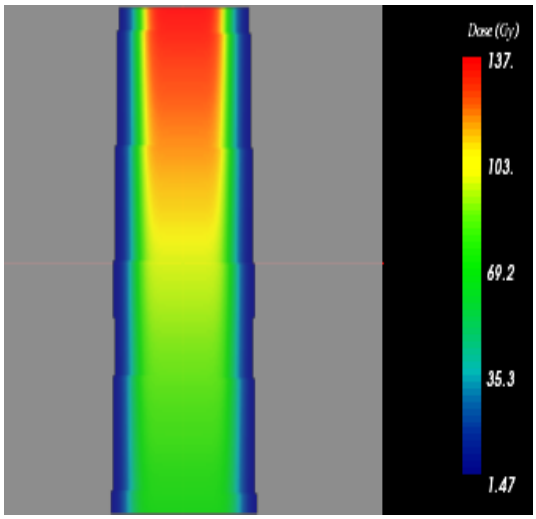

(a) Dose color wash for the anterior 5x5 cm^2 field

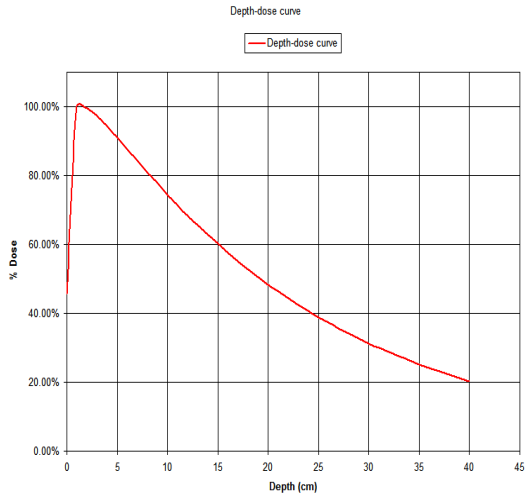

(b) Depth dose profile

Figure 3.20: Dose color wash and its corresponding depth dose profile for the anterior field

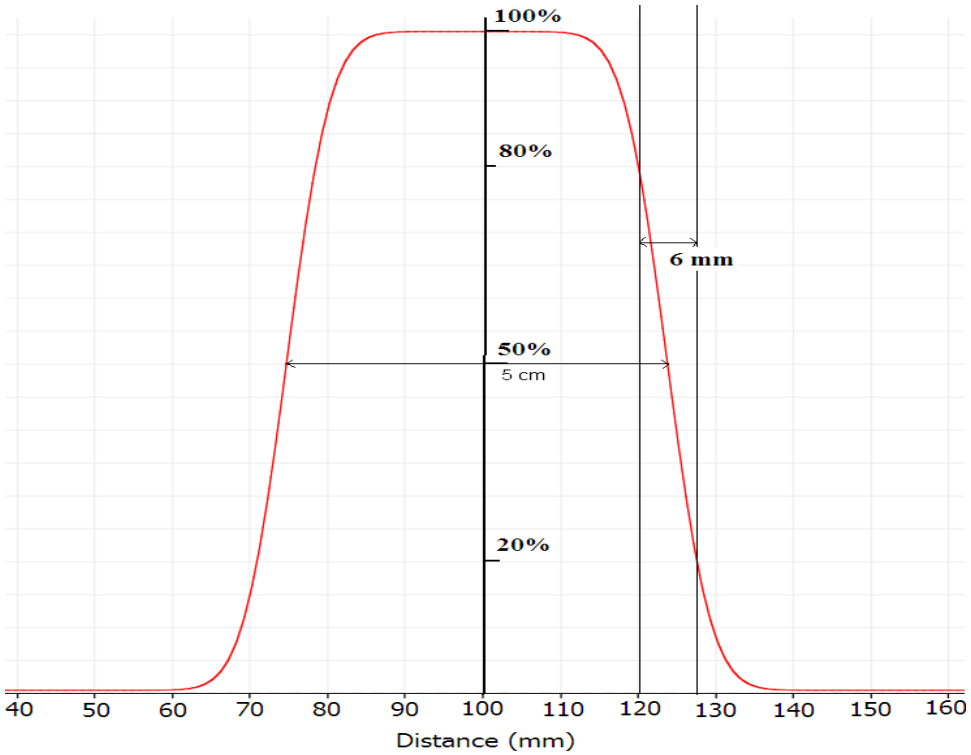

Figure 3.21: Cross profile for the anterior 5x5 cm^2 field with the penumbra width shown

The summed dose distribution for the 4F-brick technique by applying matrix rotations and its lateral cross profile are shown in figures 6.12 and 3.22b respectively and their isodose lines are shown in figure 3.23.

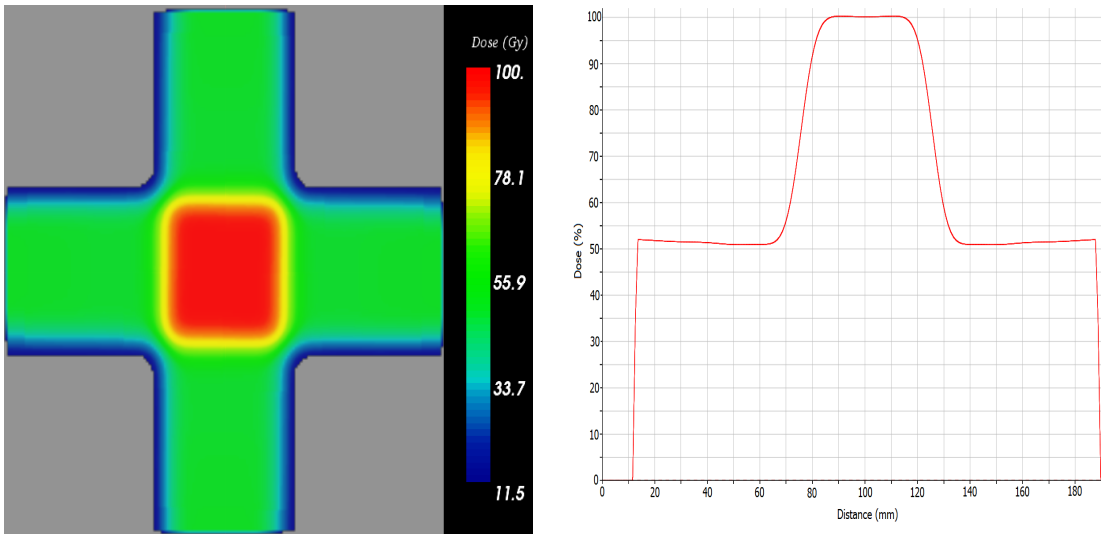

(a) Dose color wash

(b) Lateral cross-profile

Figure 3.22: Dose color wash and lateral cross profile for 4F-brick technique with 5x5 cm^2 fields

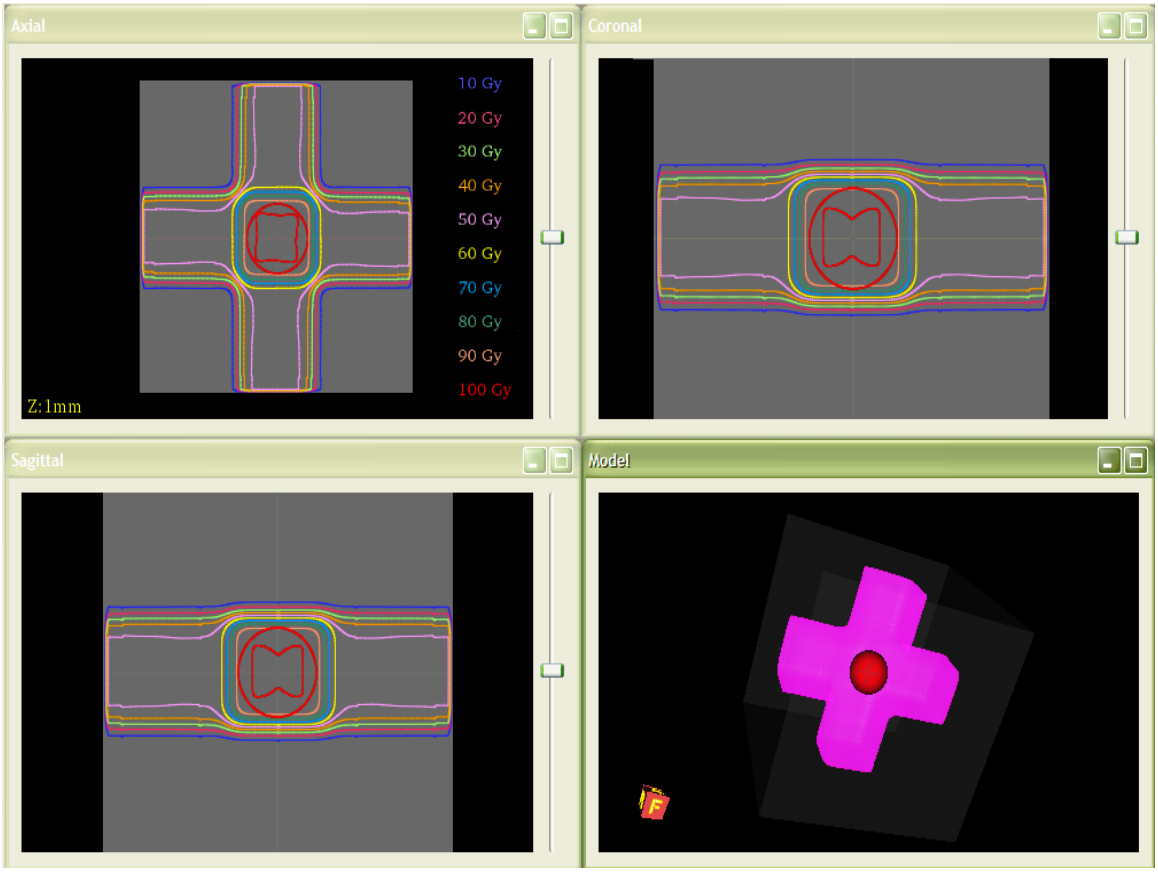

Figure 3.23: Isodose lines for the 4F-brick technique in axial, sagittal and coronal planes

3.10 Simulation of geometric uncertainties in Biosim

Systematic(Σ) and random(σ) uncertainties can be simulated for VOIs generated either from DICOM objects or standard shapes. The systematic and random standard deviations and the TCP parameters can be set using the simulation dialog as shown in figure 3.24. The dose grid is first resampled to 1x1x1 mm^3 using cubic interpolation since the displacement resolution is 1 mm. The target structure of interest (generally CTV) is divided into 1x1x1 mm^3 voxels. The voxel indices in the corresponding dose grid are found using equations (3.1)-(3.3). Systematic and random errors are randomly generated using a quasi-random number generator from the Gaussian distribution of their corresponding errors (characterized by their standard deviations). A 3xn array [(x,y,z),n] of both errors were generated for each treatment, where n is the number of fractions. The values for the systematic error are the same for all the fractions in a particular treatment, but different from fraction-to-fraction in the random error array. The error vector in each element of the array is summed and rounded off to the nearest integer to provide the resulting displacement for each fraction.

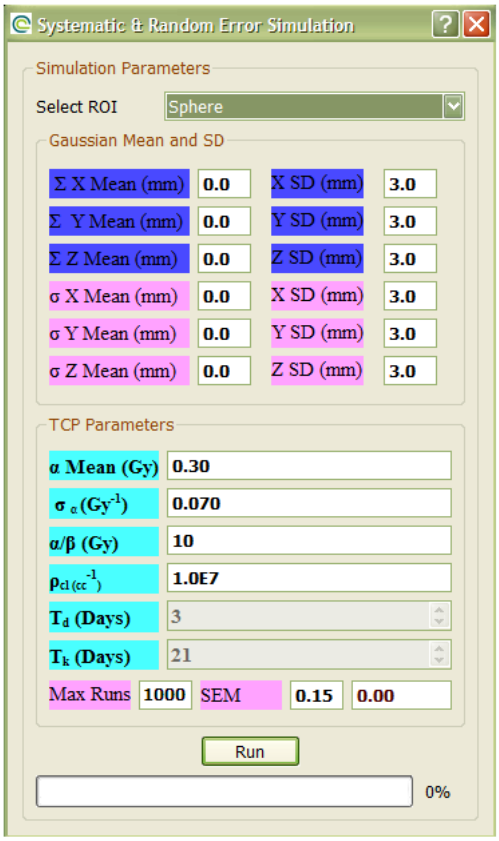

Figure 3.24: Simulation dialog with TCP parameters, systematic(Σ) and random(σ) error standard deviations set. The maximum number of runs and the desired standard error of mean (SEM) for the simulations can be set. Simulation automatically stops when either of the criteria is met.

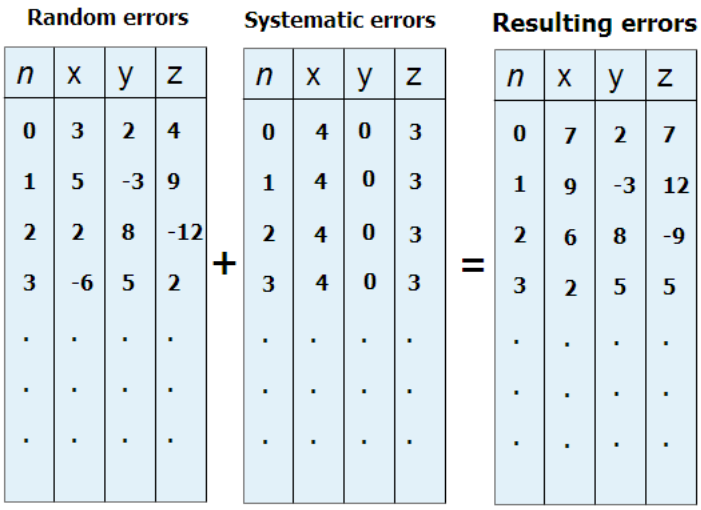

Figure 3.25: Summation of error vectors

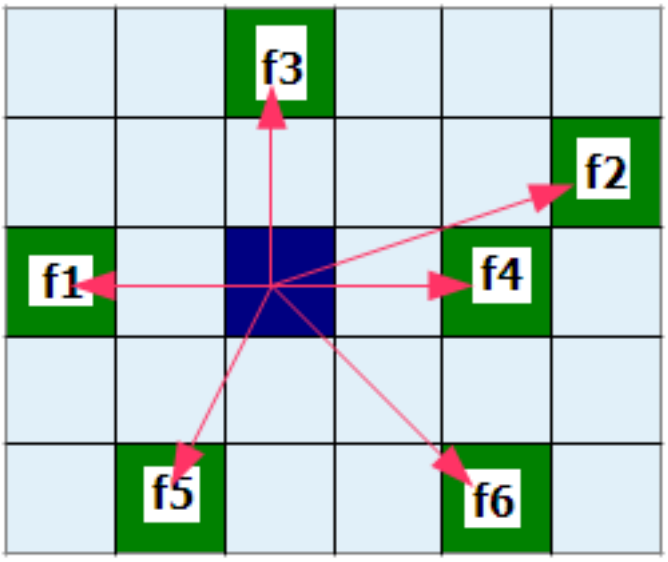

Figure 3.26: Depiction of dose accumulation process

Consider the blue voxel in figure 3.26 as the voxel-of-interest for which the dose needs to be accumulated. The green voxels are the position of blue voxel in each fraction (f1,f2....f6) due to geometric uncertainties. Then the cumulative dose to blue voxel is the summation of dose values at voxels f1 to f6. This is mathematically expressed in equation (3.4).

$$D_{voxel} = \sum_{f=0}^{f=n} D_f \tag{3.4}$$

Where D_f is the dose at the position of the voxel in fraction f. Differential DVHs are calculated from the accumulated doses to compute TCP values. The simulations

are repeated several times until the standard error of the mean TCP is $\leq 0.15\%$. The simulation process in shown in figure 3.27 and the resulting sample DVHs are shown in figure 3.28 respectively .

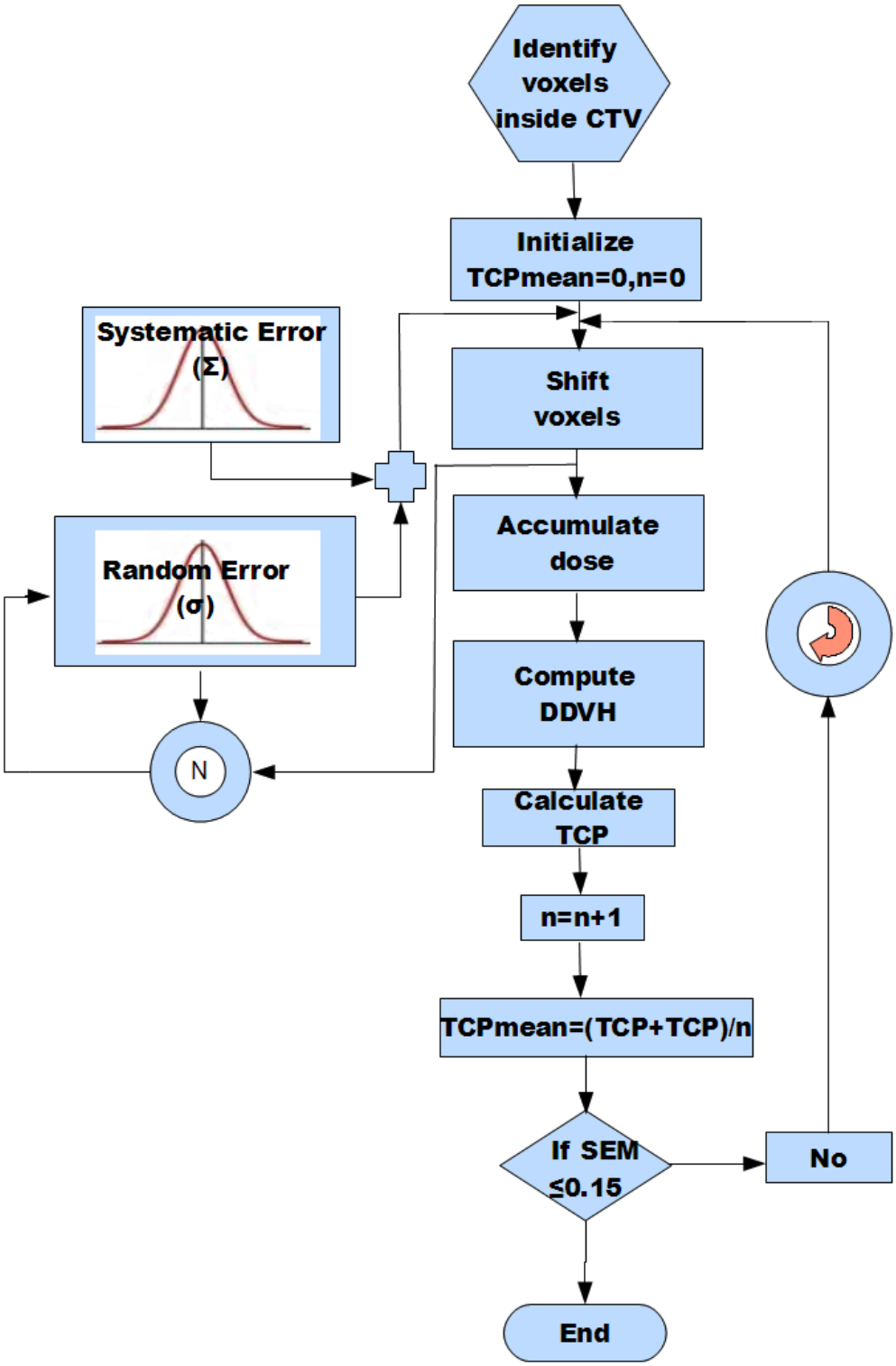

Figure 3.27: Geometric uncertainties simulation process: One systematic error per treatment and one random error per each fraction in the treatment are generated using a quasi-random number generator. Subsequently, the dose in each voxel inside the CTV is summed using the error vector resulting for each fraction to obtain the cumulative dose at the end of the treatment. Differential DVHs are generated to calculate TCP. The entire process is repeated several times (n number of items) until the standard error of the mean TCP values obtained is ≤ 0.15.

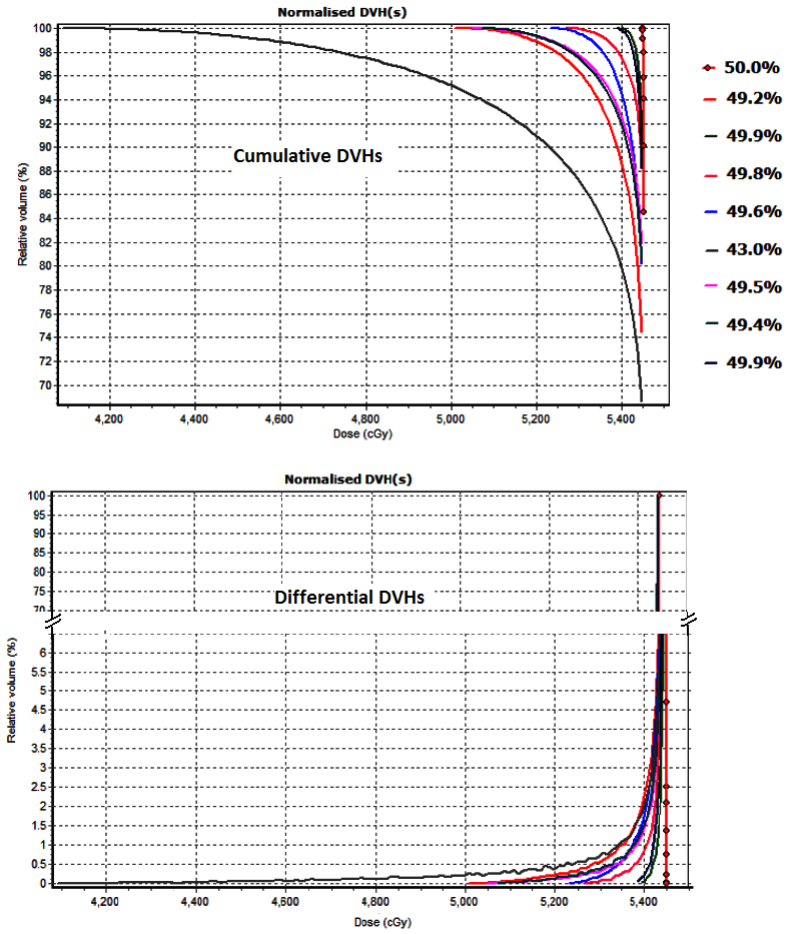

Figure 3.28: Representative DVHs inclusive of geometric uncertainties for a 25 mm radial CTV. The DVH for the static CTV is shown with the red marker. The PTV margin is 8mm with Σ, σ=3mm.The dose was 55Gy in 20 fractions with $\bar{\alpha} = 0.301 Gy^{-1}, \sigma_\alpha = 0.114 Gy^{-1}, \alpha/\beta = 10 Gy, \rho_{cl} = 1.0E7\, cells/cc$. *Take note of the dose range.*

3.11 Varying clonogen density in GTV-CTV region

A clonogen density grid with an exponential fall-off can be generated in Biosim. This is achieved by calculating the distance from the nearest surface of the surface mesh (GTV) to every voxel that lies outside the specified surface. Using the distance value the clonogen density can be calculated with a user specified slope (s). The maximum distance up to which the calculation is performed can also be set, which is usually up to the CTV. The clonogen density input dialog is shown in figure 3.29 with a clonogen density profile is shown along with the dose profile in figure 3.30 for a 20 mm radial GTV and 25 mm radial CTV with a slope factor of '3'. The density values are truncated at the edge of the CTV, i.e., the density values only inside the GTV-CTV space are considered for the calculations.

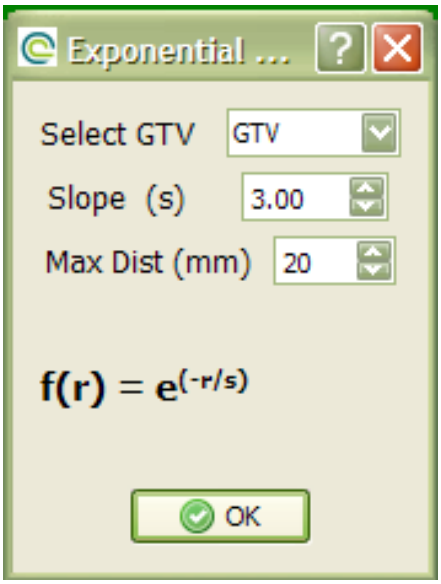

Figure 3.29: Exponential clonogen input dialog

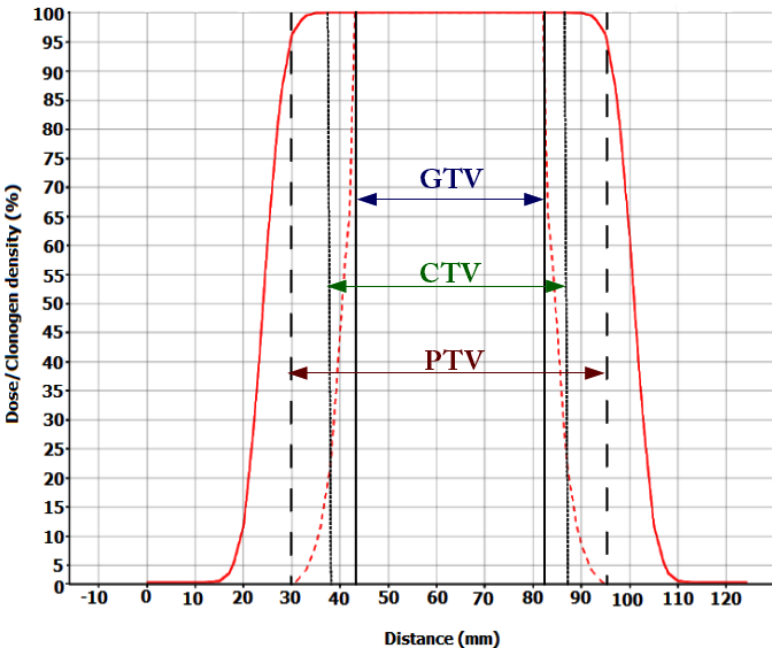

Figure 3.30: Profile of clonogen density (dashed) and dose (solid) across GTV, CTV and PTV.

Chapter 4

Loss of local control due to tumour displacement as a function of margin size,dose-response slope and number of fractions

4.1 Introduction

External beam radiotherapy comprises several procedures from imaging through treatment delivery, involving patient positioning, imaging, target delineation, dose calculation and treatment delivery. Uncertainties are inherent in all of the above procedures which can be reduced but not eliminated by quality assurance and quality control procedures. These uncertainties are categorized as systematic and random errors [93, 94]. Systematic (preparation) errors are those which propagate throughout the course of treatment with the same magnitude and direction. Random (execution) errors can vary from fraction to fraction, examples include organ motion or day-to-day setup variations, resulting in dose not being delivered as intended. Assuming shift-invariance (ignoring the effects of changes in source-to-surface distance (SSD), change in depth, surrounding tissue density on dose delivered) systematic errors tend to shift the dose distribution while random errors blur the dose distribution [53, 94, 95]. To compensate for these uncertainties a planning target volume (PTV) is created by expanding the clinical target volume (CTV) by an appropriate margin [**?**, **?**]. Adequate margin size is crucial to obtain good coverage of the target volume during treatment delivery but the unavoidable inclusion of normal tissues in this margin usually limits the dose that can be delivered due to the risk of complications. In reality, systematic and random errors may, in addition to translations, include rotation and deformation of target as

well. These rotational and deformation uncertainties will, however, not considered in this study in order to limit its complexity.

Probability density functions (PDFs) of systematic and random errors in radiotherapy delivery have been modelled as Gaussian distributions with empirically determined standard deviations. This makes it possible, as often suggested in the literature, to model the effect of random errors by convolving the dose distribution with the random error PDF [96–99].The convolution method has been shown to overestimate the radiobiological indices for the target volumes and underestimate for the organs-at-risk [100]. Also, the radiobiological dose-response relationship is non-linear and the linear convolution of dose does not reflect the biological effects on the individual voxels correctly [84]. It is nevertheless accurate enough for moderately fractionated radiotherapy (number of fractions >15) and small changes in the dose experienced by the tumour [98, 101].

For given standard deviations of systematic (Σ) and random errors (σ), several authors have proposed margin recipes meeting various criteria based on the minimum delivery of a certain percentage of the prescription dose to the CTV for a certain percentage of patients [51, 94, 101]. For example, vanHerk*et al* proposed a margin of $2.5\Sigma + 0.7\sigma$ whereas Stroom *et al* proposed a margin of $2.0\Sigma + 0.7\sigma$ [51]. While both recipes have the same coefficient for random errors, the coefficient for systematic errors differs slightly due to the criteria chosen to derive the margins. It is obvious from the margin recipe formulas that the systematic errors are more detrimental than random errors, which has much larger coefficients. The effect of individual errors (Σ, σ) and both combined is shown in figure 4.1, which clearly shown that systematic errors alone or combined with random errors is more detrimental than random errors alone.

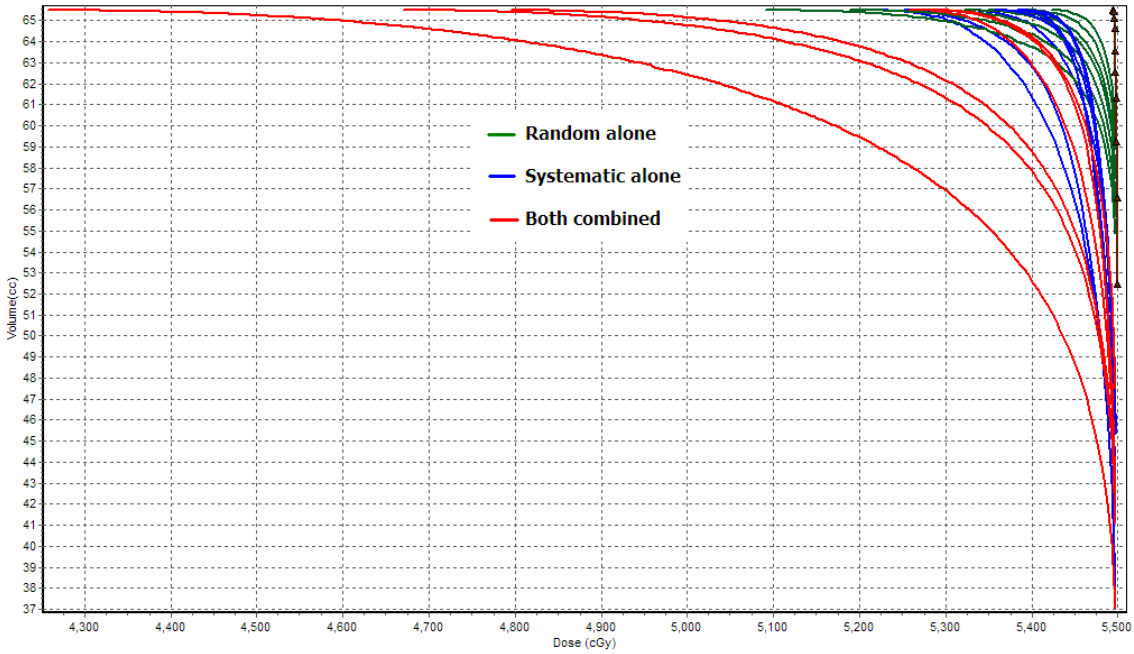

Figure 4.1: Cumulative DVHs with systematic and random errors individually (random alone, systematic alone) and combined (systematic+random) for a 20 fraction treatment. The DVH for the static case is shown with markers.

These and similar margin recipes consider criteria which are based on physical dose to the tumour. Such criterion are not directly clinically relevant. A more clinically relevant criterion is the tumour control probability (TCP), a metric which has already been considered for margin determination. For example, with the criterion of $\leq 1\%$ TCP loss to prostate tumours, van Herk *et al* proposed a modified margin recipe, $2.5\Sigma + 0.7\sigma$ -3mm [52], thus subtracting a constant from their previously published margin recipe. This strongly suggests that physical dose-based margin recipes are conservative and reduced margins can be used from the radiobiological point-of-view. To generalize their results to treatments with a small number of fractions, Van Herk*et al* proposed another revision to their recipe by adding an uncertainty term to the systematic error, which is standard deviation of the random error divided by the square root of the number of fractions [94]. Hypofractionated treatments such as SABR are more widely used for lung tumours [102, 103]. The margins required for these hypofractionated treatments is indeed becoming increasingly important. Moreover, if the criteria for margin determination are based on TCP, it is important to consider variation in TCP parameters and their impact on derived margins. In particular it is known that different tumours have different dose-response slopes (γ_{50}) and their differences may influence the magnitude of derived margins.

In this work we study the combined effects of dose conformity, fraction number, γ_{50}

as well as Σ and σ on margins using the criteria of $\leq 1\%$ loss in the population mean TCP ($\overline{TCP}$) and of $\leq 1\%$ loss in 90% of the patients, each loss being relative to the TCP obtained for a static tumour.

4.2 Material and Methods

4.2.1 TCP calculation for different γ_{50}

TCP for each treatment (or patient) and mean population TCP ($\overline{TCP}$) for n patients are calculated using the enhanced Marsden model [71] as shown in chapter 2. Since γ_{50} is not a parameter in this TCP model, it is impossible to directly use the published values. So σ_α was fitted to produce the same gradient at TCP=50% as the slopes in the literature, for $\bar{\alpha}$ fixed at 0.30 Gy^{-1}. The γ_{50} values for squamous cell carcinoma (SCC) is shown to be in the range 1.5 to 2.5 [68]. So their corresponding values of σ_{alpha} in that range representing different tumour types with shallow, steep and intermediate dose-response characteristics were chosen namely 0.8, 1.8, 2.8 and 3.9. The σ_α value for NSCLC was taken from Nahum *et al* [104] and the corresponding γ_{50} is shown table 5.1.

Table 4.1: γ_{50} and their corresponding σ_α for different tumour types

Tumour Type	γ_{50}	σ_α
SCC	0.8	0.218
SCC	1.8	0.070
SCC	2.8	0.048
NSCLC	3.9	0.037

The TCP parameters used in the calculations for different σ_α are $\bar{\alpha}$ =0.30 Gy^{-1}, ρ_{cl}=$10^7 cc^{-1}$ and α/β=10.0.

4.2.2 Dose models

Firstly, a spherical dose distribution with a Gaussian penumbra and a 4F box-technique to respectively mimic fully and less conformal dose distributions were used to simulate the effect of geometric uncertainties with a fixed standard deviation (3 mm for both Σ and σ) for four different γ_{50} (covering the range of observed slopes, taken from the literature) for 3, 5, 10, 20 and 30 fractions. Secondly, different combinations of systematic and random uncertainties (Σ ,σ) namely (1, 1), (1, 3), (3, 1), (3, 3) were used to derive the margins required for a $\leq 1\%$ loss in $\overline{TCP}$ for the range of number of fractions and γ_{50} mentioned above. A Monte Carlo approach was used to simulate the effect of geometric uncertainties on TCP. The dose models are generated as described

in sections 3.8 and 3.9 in chapter 3 (Biosim). In the spherical dose distribution the 95% isodose surface just encompasses the PTV and the distance between the 95% and 50% isodoses is approximately 5mm. This level of dose conformity cannot be realized in practice, but represents a best-case in terms of conformity and will be the most sensitive to tumour motion, due to the equal and rapid dose fall off in all directions. For the 4F box-technique technique the 95% isodose surface encompasses the PTV but there is a considerable amount of incidental dose outside the PTV. This dose distribution is used to study the effect of less conformal technique and the incidental dose outside PTV on the required PTV margins.

4.2.3 Monte Carlo simulation of geometric uncertainties

To simulate the geometric uncertainties, systematic and random displacement vectors were sampled from two Gaussian distributions using pseudo-random number generator. Different sets of standard deviations were chosen for both systematic and random displacement distributions. One systematic displacement per treatment (patient) and one random displacement for each fraction of each treatment were sampled. The vector sum of systematic and random vectors give the total displacement for each fraction of the treatment. This method of explicitly simulating the random errors was chosen over the convolution/blurring method, because the later is valid only when using a large number of fractions. A grid resolution of 1x1x1 mm^3 was used for the calculations. Doses were summed for each voxel over the entire treatment and dose-volume histograms for each patient computed. Even though this method of summing the doses linearly at each fraction is not strictly correct but the radiobiological differences between this approach and that of applying the linear quadratic (LQ) model at each fraction are clinically insignificant [105]. The number of simulated treatments, n was increased until the standard error of the mean calculated as $SEM_{TCP} = (SD_{TCP}/n\ )$ was ≤ 0.15.

Where SD is the sample standard deviation. The number of simulations ranged from a few hundred to a few thousand depending on the PTV margin.

The PTV margin was varied from 3 mm to 12 mm in steps of 1mm and the simulations were performed on both dose distributions for different dose-response slope and for 3, 5, 10, 20 and 30 fractions. The prescription dose for 20 fractions was 55 Gy as per the local protocol for lung radiotherapy and prescribed doses for other fraction numbers were derived such that they all resulted in 50% TCP for a static tumor. We chose 50% as our reference TCP value to be at the steepest point in the dose-response curve. It is therefore at this point that TCP will undergo the largest changes caused by any dose degradation due to geometric uncertainties. The margins required at this TCP level can thus be safely applied for any other TCP value. The $\overline{TCP}$ and percentage of patients receiving $\leq 1\%$ TCP loss from the static tumour TCP were calculated

for each case. Clonogen proliferation was not considered in this study.

Figure 6.17 shows the typical variation in dose and TCP (for respective DVH shown) for a CTV of 25 mm radius for 3 and 30 fractions with a PTV margin of 8 mm for $\Sigma, \sigma = 4$ mm (*deliberately a smaller margin was chosen to show the differences clearly*) . The prescription dose was chosen to provide 50% TCP for a static tumour. TCP values vary more for 3 fractions compared to 30 fractions, as would be expected.

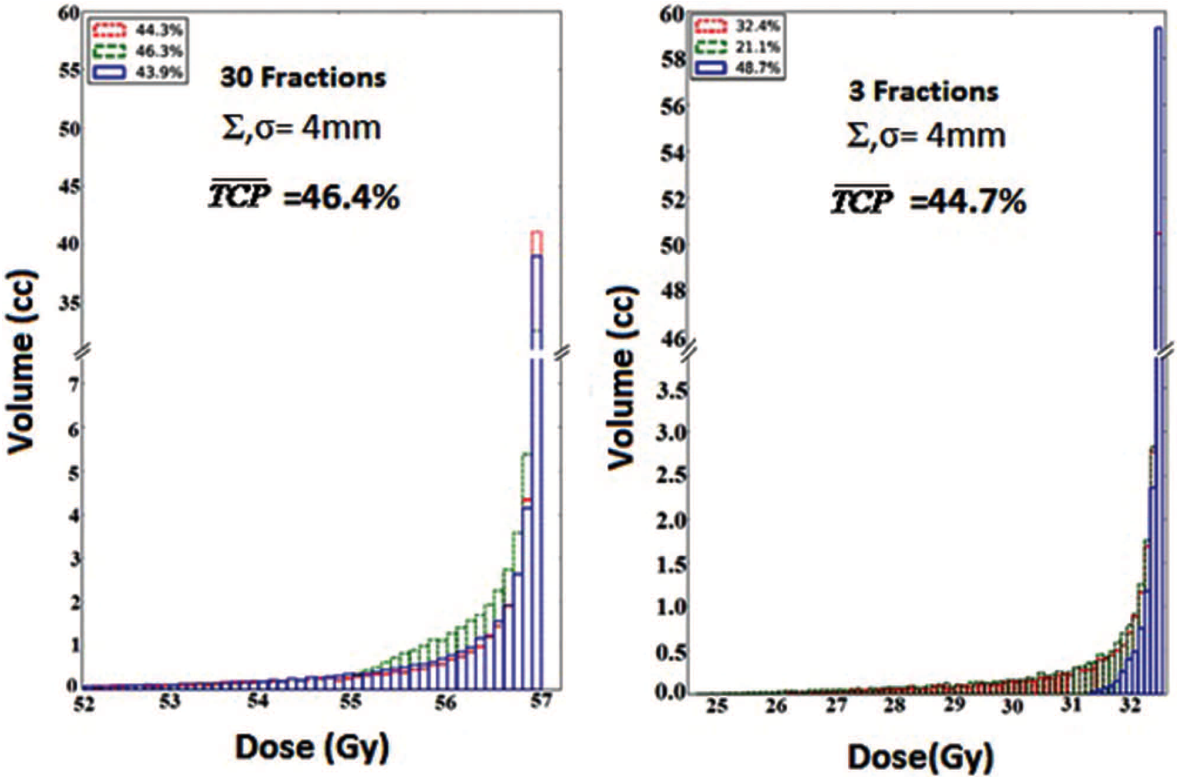

Figure 4.2: Differential DVHs showing the effect of fractionation on cumulative dose to CTV. TCP for the selected DVHs is shown with $\Sigma = \sigma = 4$ mm, as is the mean population TCP (averaged over a large number of DVHs as described in the text). The individual TCP values are shown in the figure legend.

4.3 Results

4.3.1 TCP vs Margin size

$\overline{TCP}$ and $\leq$1% in 90% of the patients for different number of fractions and dose-response slope values are shown in figure 4.3 for spherical and four-field box dose distributions for 3 mm Σ and σ. From these figures gradually increases and attains a constant value (highest achievable for the given dose) above a certain margin. They also show clearly that the margins required for smaller numbers of fractions are larger than those for greater numbers of fractions, indicating hypofractionated treatments are more vulnerable to geometric uncertainties. Furthermore, the difference between the

margins required for $\leq 1\%$ loss for 3 and 30 fractions increases as γ_{50} increases. The margin for the four-field box distribution shows a similar dependence on fractionation and γ_{50} but the margins required are reduced. This is due to a reduced dose fall-off from opposing beams. Similar trends can be seen for the percentage of patients receiving $\leq \%$ loss in TCP (figure 4.4 a & b). But the required margins are slightly larger than the later case.

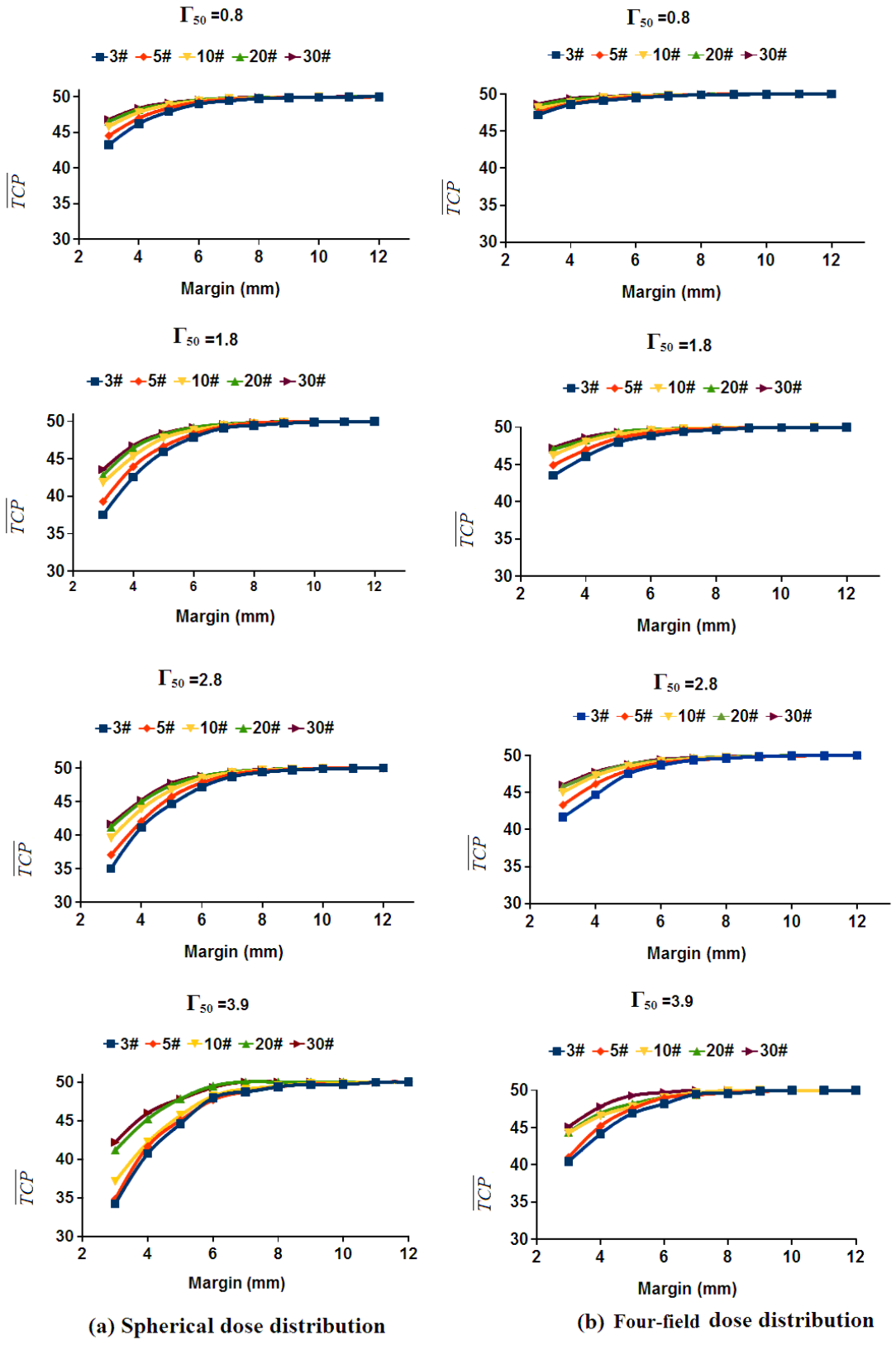

Figure 4.3: $\overline{TCP}$ plotted against PTV margin for different number of fractions for spherical and four-field box dose distributions with $\Sigma \,\&\, \sigma = 3mm$ for different γ_{50}.

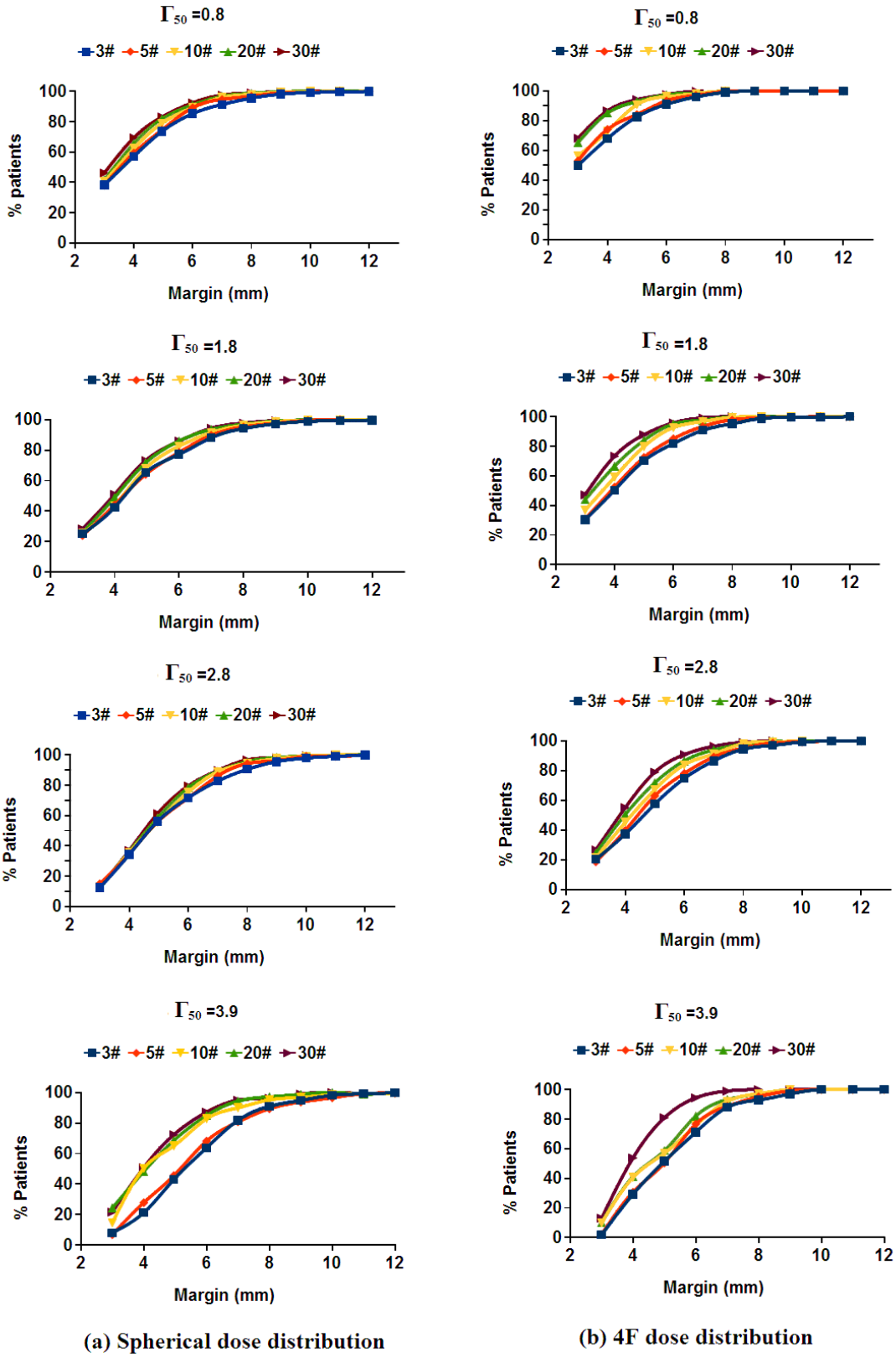

(a) Spherical dose distribution **(b) 4F dose distribution**

Figure 4.4: Percentage of patients with $\leq$ 1% loss in TCP vs PTV margin for a) spherical and b) four-field box dose distributions with $\Sigma \,\&\, \sigma$ =3mm for different γ_{50}.

4.3.2 Margin comparison with published recipes

The differences between fractionation-dependent margins calculated using van Herk *et al* TCP-based recipe [53] and the TCP- loss based margins derived in this work for Σ=1 and σ =3 mm are shown in figure 4.5. The fractionation is accounted in the TCP-based recipe as suggested by van Herk et al [52] by quadratically adding an additional term to Σ (which is calculated by dividing σ by the square root of the number of fractions). Figure 4.5 clearly demonstrates that fractionation-dependent margins considerably increase as the number of fractions decreases for both the margins derived using van Herk et al TCP-based recipe and from this work. For a fixed value of γ_{50}, both curves are still essentially parallel, showing that van Herks correction term reproduces the fractionation dependence found in this work. It should be born in mind that the van Herk TCP-based recipe is derived for prostate tumours which have a shallow DRC (low γ_{50}) and for large number of fractions. The margins calculated in this work and van Herk et al [52] TCP-based recipe is almost the same for a large number of fractions and low γ_{50} . However, the margins differ considerably for other fractions and γ_{50} . The differences could be greater for larger Σ and σ. The gap between the two surfaces widens as γ_{50} increases, which demonstrates the importance of considering dose-response slope of tumours when deriving margins. This also emphasizes the fact that margins derived from a TCP-based recipe assuming a particular γ_{50} will not apply for tumours with different γ_{50}.

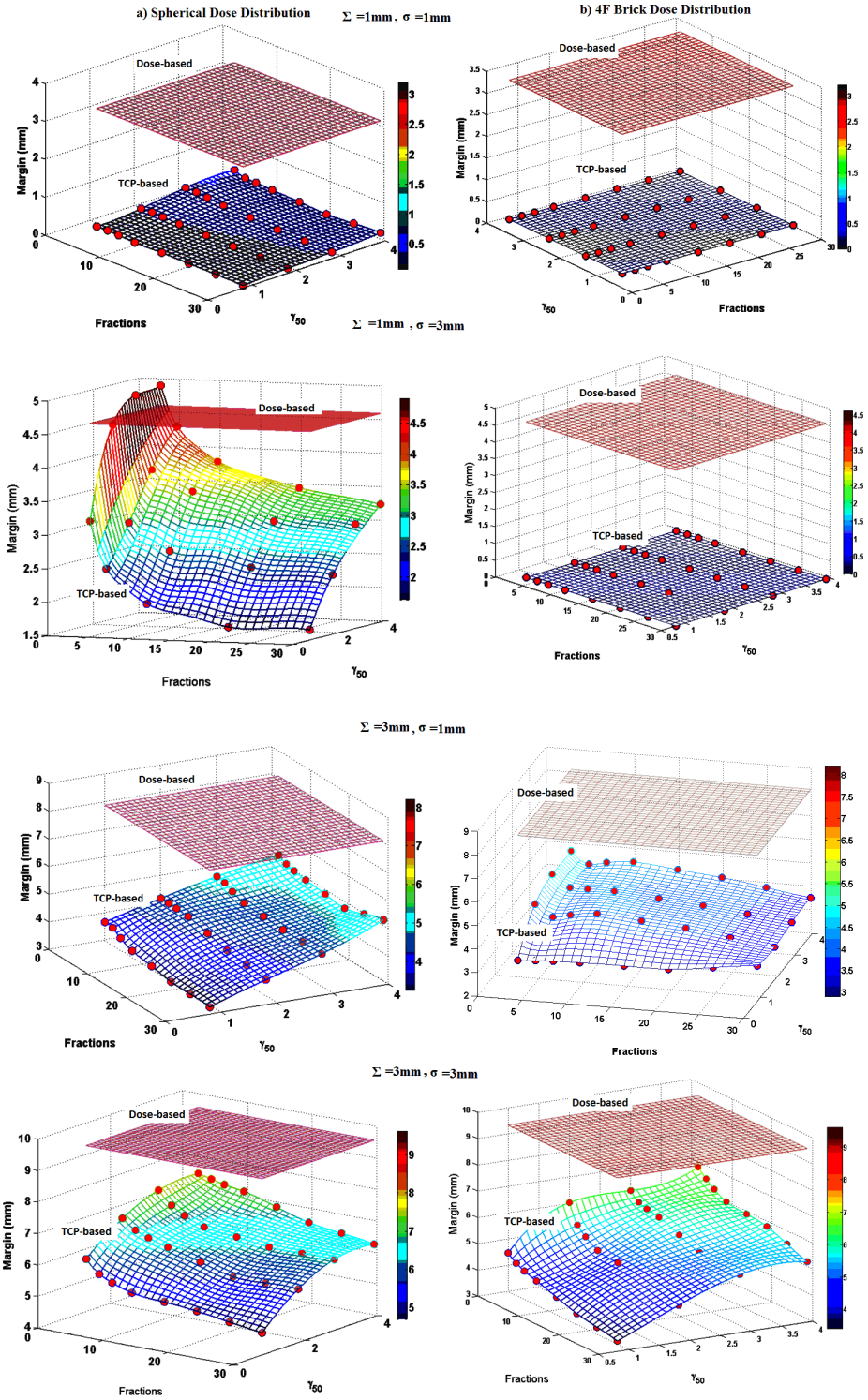

Figure 4.5: Surface plot of margin required for $\leq$ 1% loss in $\overline{TCP}_{pop}$ as a function of treatment fractions and γ_{50} for different combinations of systematic and random uncertainties with their corresponding physical dose-based margins shown as a plane (Red dots represent actual data values).

4.3.3 Fractionation corrected vs uncorrected Margins

The differences between fractionation-corrected and uncorrected margins calculated according to the physical dose-based recipe [94] with the $\overline{TCP}$ loss based margins forΣ=1 and σ =3 mm are shown in figure 4.6. The fractionation is accounted for by quadratically adding an uncertainty term to Σ, which is calculated by dividing σ by the square root of the number of fractions. Fractionation corrected margins significantly increase as the number of fractions decrease. Nevertheless, TCP-based margins accounting for fractionation are significantly smaller than fractionation-corrected margins calculated using a physical dose-based recipe.

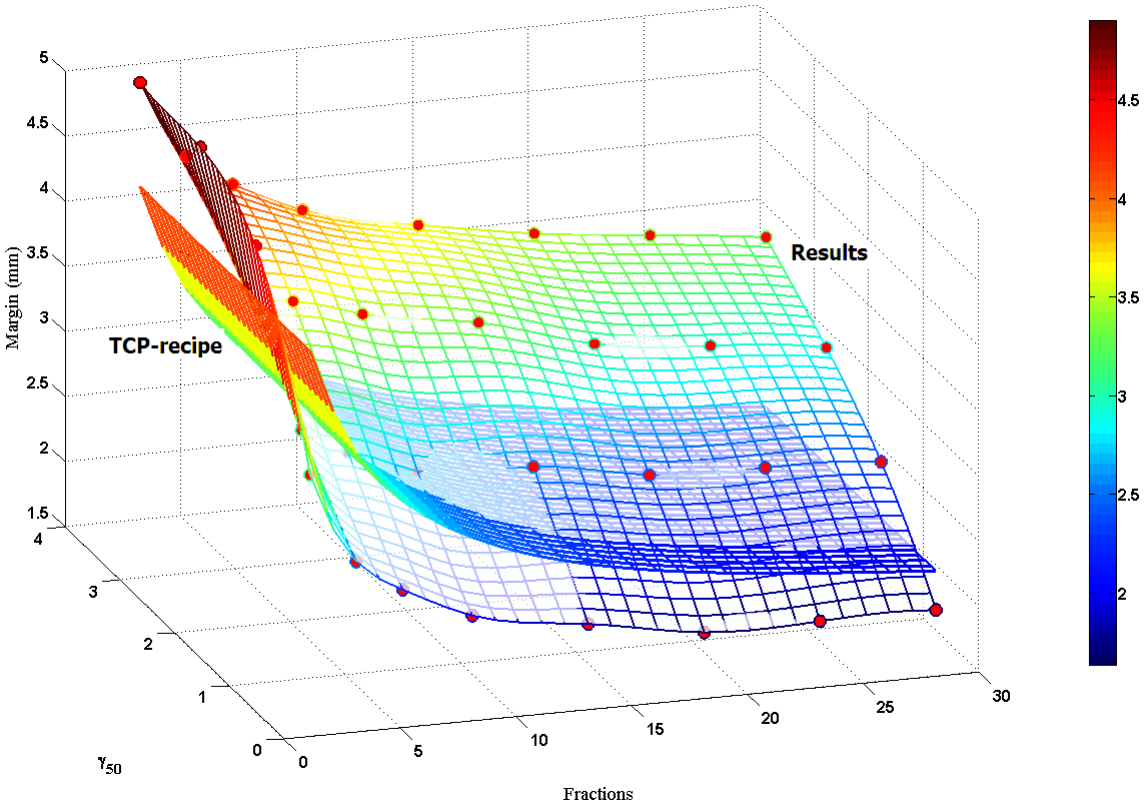

Figure 4.6: Van Herk *et al* (VH) margin plane corrected for fractionation and uncorrected with the margins obtained in this study for $\leq 1\%$ loss in $\overline{TCP}$

4.3.4 Dependence of margins on dose conformity

To demonstrate the dependence of margins on dose conformity; a prostate tumour with different PTV margins was planned with different techniques. The techniques include three-field (Anterior, 2 laterals), four-field (AP-PA , 2 laterals), IMRT (5 fields) and spherical dose-distribution with Gaussian penumbra. The field arrangements are shown in figure 4.7. The spherical dose distribution is an artificial dose distribution which has no beam entry or exit paths and has the least incidental dose among all four techniques. The PTV margin was varied from 2mm to 10mm in steps of 1mm. The MLC leaves

were refitted in the planning system and the dose recalculated for three-field and four-filed techniques. For the IMRT technique the plans were reoptimized considering the newly generated PTV volumes. For the spherically-symmetric dose distribution the dose was regenerated for the new PTV volumes. DICOM datasets(CT, RT dose, RT structures) were imported into Biosim for each PTV margin and technique. CTV displacements were simulated assuming 3mm standard deviation for both systematic and random errors for a 20 fraction treatment. The prescription dose was adjusted for each technique to obtain 50% TCP for the static case.

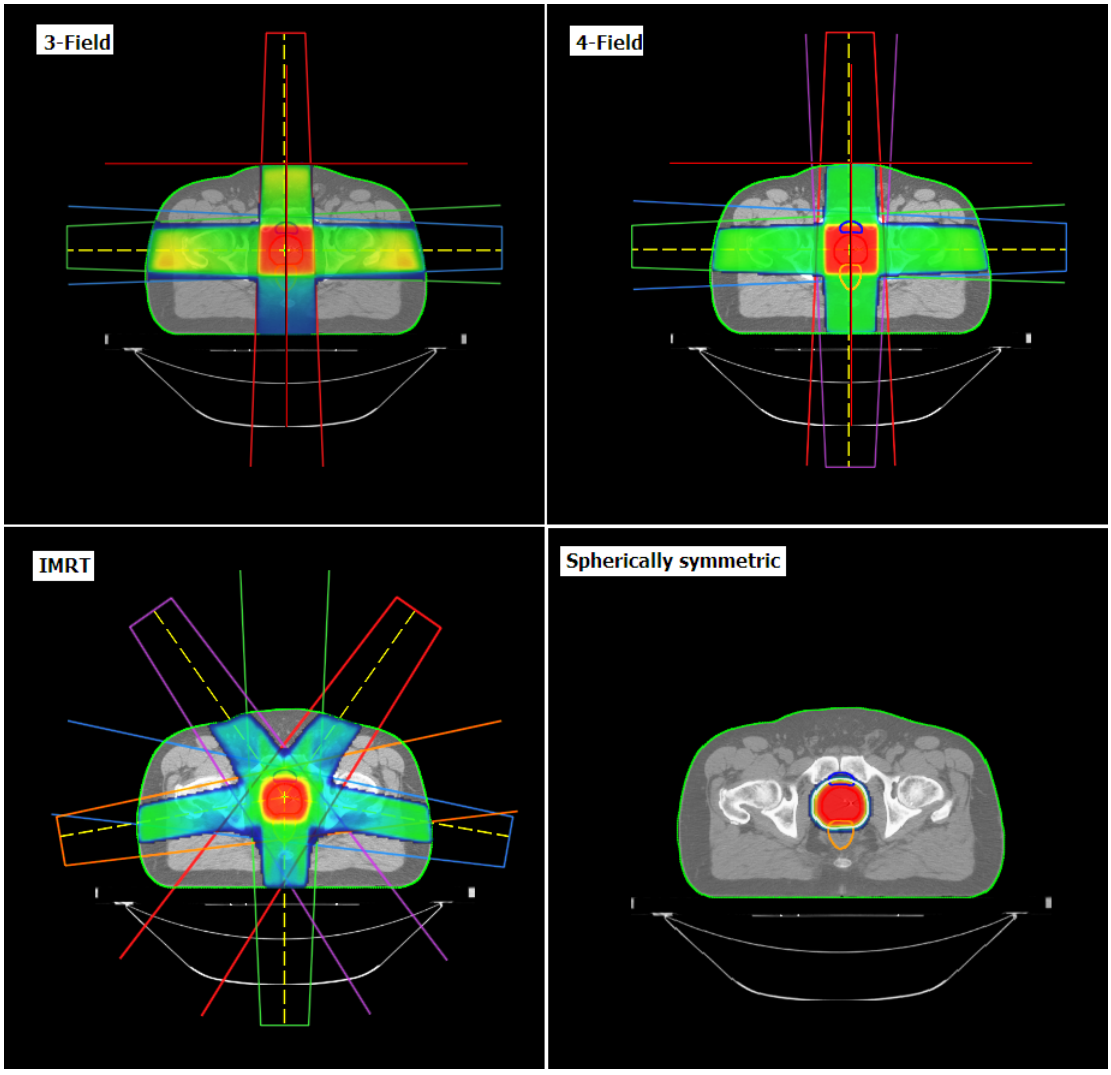

Figure 4.7: Margin vs technique. Wedges were used for the 3-field plan but wedge display is not currently supported in Biosim.

The Margin-TCP curves asymptotically increases for all the techniques.The margins required for the $l \leq 1\%$ loss in $\overline{TCP}$ increases as the dose conformity increases, which in this case increases in the order; spherically-symmetric distribution, IMRT, four-field and three-field distributions. From figure 4.7 it's also evident that the rate of TCP drop significantly increases with increasing dose conformity.

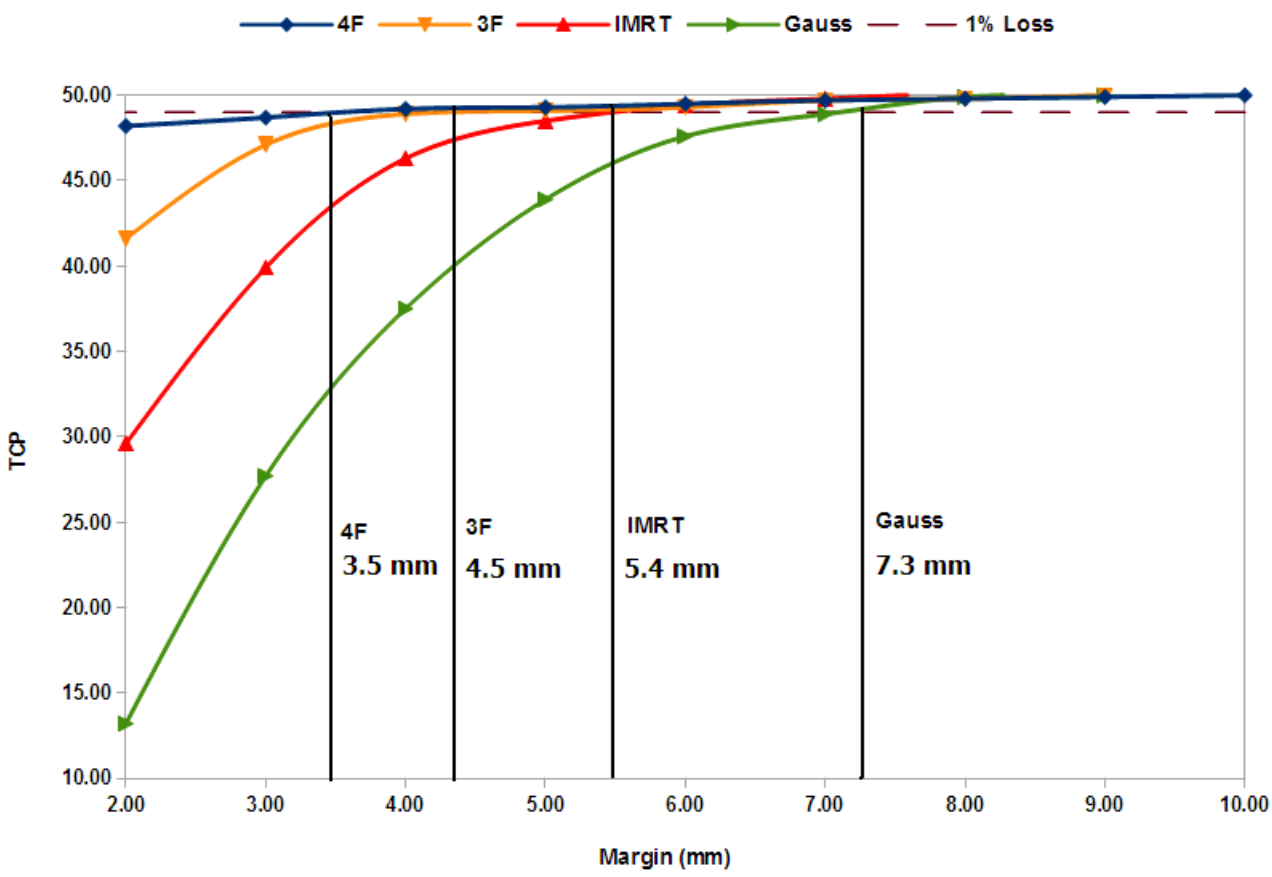

Figure 4.8: Margin required for $\leq 1\%$ loss in $\overline{TCP}$ vs technique. $\Sigma, \sigma = 3\,mm$

4.3.5 Dependence of TCP loss on tumour volume

To study the effect of TCP loss on tumour volume, CTV radius was varied from 15 to 45 mm in steps of 5mm. Prescription doses were adjusted to achieve 50% TCP in 20 fractions for the static tumour. A margin of 6mm is used. This is from our analysis of previous results which results in $\leq$ 1% loss in TCP for a 25 mm radial tumour for the number of fractions (20) and $\gamma_{50}(1.8)$ used. TCP losses were obtained by running the simulations until the standard error is $\leq$0.2 with 3mm standard deviations of systematic and random uncertainties. The TCP parameters used were same as used in other calculations in this study except γ_{50} was 1.8 (average dose-response slope). The variation of TCP loss with tumour volume is shown in figure 4.9.

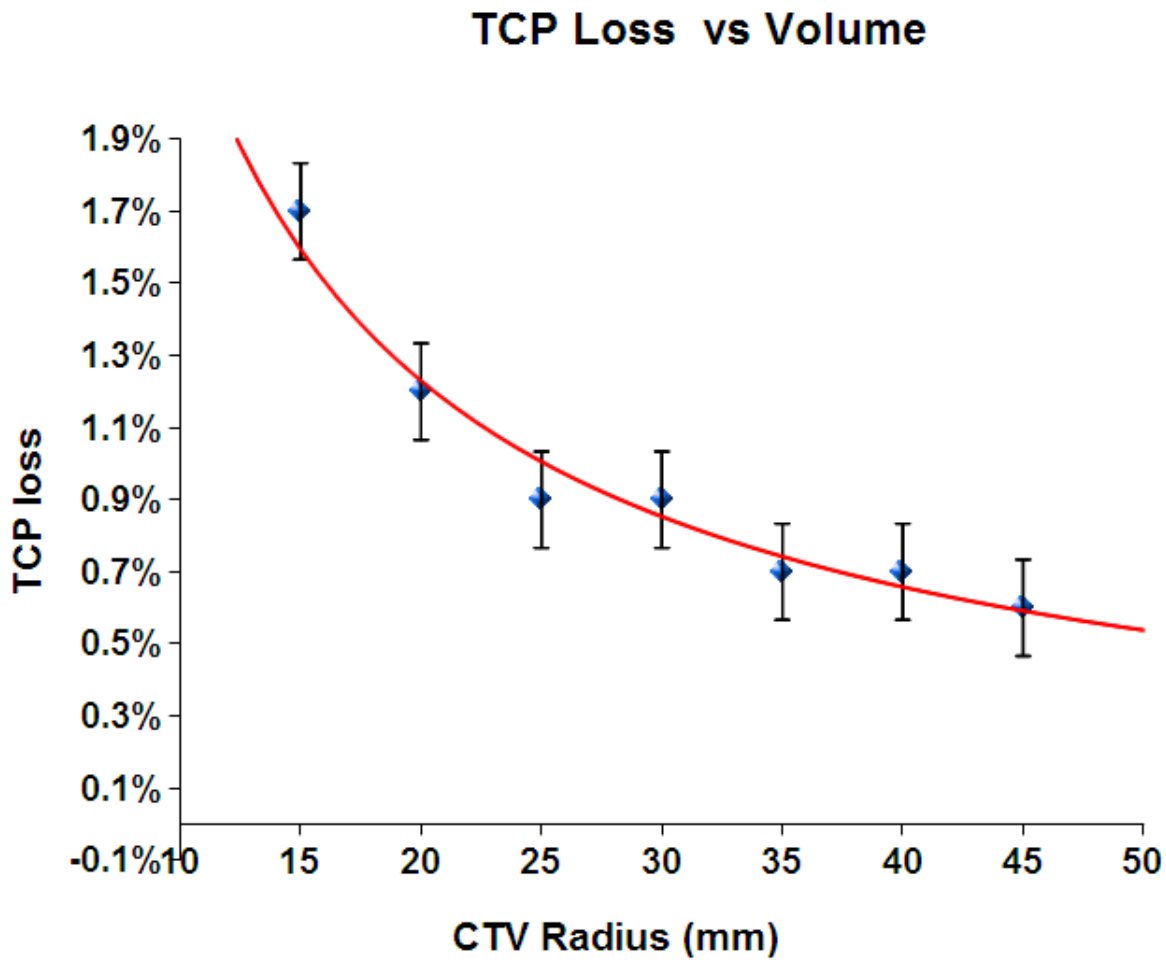

Figure 4.9: Variation of TCP loss with CTV volume with standard error ($\bar{\alpha}$=0.30 Gy^{-1}, σ_α= 0.07 Gy^{-1}, ρ_{cl}=$10^7 cm^{-3}$ and α/β =10 Gy)

4.4 Discussion

TCP-based margin recipe for prostate tumours treated with three fields has been reported and the margins were shown to be much smaller than the physical dose-based recipes (van Herk *et al* 2002). But this assumes a large number of fractions and a single dose-response slope (γ_{50} for prostate tumours).So it is difficult to use this recipe for tumours other than prostate and also for different fractions, especially hypofractionated treatments. This study involves all the variables that the TCP-based margin would depend on, namely number of fractions, γ_{50} and systematic and random uncertainties with different levels of dose conformity as well.

There are several assumptions made in this work, including shift-invariance of dose distributions, very high conformity of dose in the spherical dose distributions and a uniform clonogen density inside the CTV. We consider two of these assumptions to be worst-case scenarios thus allowing our conclusions to be safely extended to more

realistic situations. The first pertains to our use of a constant clonogen density in the GTV-to-CTV region where it will be lower than that in the GTV [106–109]. However, overestimating the number of clonogens in the region which will be the most affected by tumour displacement will lead to an overestimation of required margins, so in that sense the margins derived in this work are conservative. Another assumption is the high conformity of the spherical dose distribution. We realize this dose distribution may be unachievable but here again any displacement will bring the clonogens to an unrealistically low dose region. This will in turn increase clonogen survival and therefore reduce TCP further. The four-field box dose distribution was chosen to study the effect of beam directions and significant incidental dose on the TCP.

The slope of the dose-response curve affects the importance of systematic and random errors on TCP [110]. Our results show that it not only depends on geometrical uncertainties and dose-response slope but also on the number of fractions and treatment technique used. It is evident that random errors increase in significance for hypofractionated radiotherapy. For a small Σ and σ (1, 1) the margins are much smaller (near zero) than the margin calculated according to the physical dose-based recipe [94]. In this case, the variation of the margin with number of fractions and dose-response slope is negligible. In the case of (1, 3) though Σ is less, it is interesting to note that the margins for a very small number of fractions and a steep γ_{50} are even higher than the margins calculated by physical dose-based recipe. This emphasizes the need to use a larger margin for hypofractionated radiotherapy, particularly for tumours with steep dose-response slope, such as in SABR of lung tumours. For a large Σ and a small σ (3, 1) the margins increase gradually with fractions and γ_{50} but they are much larger than (1, 3) denoting that a large Σ always require a larger margin than for the same σ. The margins required for $\leq 1\%$ loss in $\overline{TCP_{pop}}$ are in general significantly lower than the ones calculated by physical dose-based recipe. It has also been recently shown by Yoda *et al* [111] that the coefficient of the systematic component in van Herks margin recipe is smaller than the one used by van Herk *et al* [94] for anisotropic systematic uncertainties, which shows that the margins for anisotropic systematic uncertainties is smaller than the ones calculated by van Herk *et al* (vanHerk2000).

For the four-field dose distribution the margins are <1mm for Σ and σ (1, 3) and (1, 1) mm. This indicates that for less conformal treatments the incidental dose outside the target volume will take care of small geometric uncertainties with out needing any extra margin around it. The margins for other combinations of Σ and σ are lower than those required for the spherical dose distribution. This leads to the conclusion that margin selection strongly depends on the conformity of the prescribed dose, number of beams and their directions which determines the dose spread outside the PTV, in particular in situations where uncertainties are not isotropic. The relationship between

the level of the incidental dose and the number of beams would also be interesting to explore as it should affect the resulting incidental killing of clonogens. Jin *et al* have shown that the distance between the 50% and prescription isodose level are in most cases exceed 10 mm and this dose can be sufficient to kill the relatively small number of clonogens in the GTV-CTV region [54]. Thus, the inclusion of a non-uniform clonogen density in the GTV-CTV region would reduce the required margins even further. Jin *et al* (2011) have derived a margin recipe as a function of geometric uncertainties and variation of clonogen in the GTV-CTV region, this margin being directly added to the GTV rather than the CTV. These margins are substantially (few mm) smaller than the TCP loss-based and physical dose-based margins but reliable clinical data on the clonogen variation in the GTV-CTV region is scarce and yet crucial if these results are to be used clinically. On the other hand, parameters for TCP calculation for certain tumour types are available in the literature. It is worth mentioning here that the TCP model parameters were fitted to the dose distributions derived using the dose calculation algorithms in the treatment planning systems (TPS) and the observed clinical outcomes. TCP parameters published in the literature assume that the dose distributions calculated by the dose calculation algorithm in the TPS represent the actual dose delivered to the tumour, which is valid. In reality the difference between the doses calculated and delivered to tumours differ because of the limitations in the accuracy of the dose calculation algorithms and also due to the geometric uncertainties in the treatment delivery, which the dose calculation algorithms do not account for. Differences up to 20% were reported while using TCP parameters inconsistent with the dose calculation algorithm [112]. Thus the TCP parameters require a refit to the observed clinical outcomes using the dose distributions actually delivered to tumours which accounts for geometric uncertainties. TCP based margins are more robust if the assumptions on which they are based are valid, namely TCP parameters, accurate definition of CTV.

The dependence of TCP loss on tumor volume was found to be weak. In general, the relative loss in TCP was greater for smaller tumors, but depends on the TCP parameters used and the prescription dose and degree of geometric uncertainties. From the results of an average dose-response slope (γ_{50}), 20 fractions and 3 mm standard deviation of both systematic and random uncertainties the variation in TCP loss (relative to static tumour) ranged from 1.7% to 0.6%.

Chapter 5

Effect of clonogen distribution on tumour control probability

5.1 Introduction

A typical planning approach is to expand the CTV with a PTV margin such that CTV will always receive the prescribed dose even in the presence of geometric uncertainties. As mentioned before, general objective of treatment planning is to achieve a uniform dose distribution inside and as low as possible outside the PTV. This assumes that there are no clonogenic cells outside the CTV and every voxel inside the CTV has the same number of clonogenic cells. However, studies have shown that the probability of clonogenic cell density decreases from the GTV boundary and it may not be limited to the CTV [14, 58, 59, 113]. In such a scenario, relatively lower density clonogenic cells can be eradicated with a relatively less amount of dose than that is usually considered tumoricidal. Thus the PTV margin can be reduced to limit the high dose more closer to the CTV and the gradual dose fall off inside the *reduced-PTV* should be sufficient to eradicate the low density clonogenic cells even in the presence of geometric uncertainties (cf. fig1.4).

Treatment delivery accuracy can be greatly improved with IGRT techniques, thus a smaller PTV margin can be used to account for smaller uncertainties in these techniques. However, the reduced PTV margins should be treated with caution as the accuracy of CTV definition (extent of clonogenic cells) becomes more and more important in these situations [114]. In cases where large PTV margins are used (conventional treatments), the uncertainty in the CTV definition can be taken care of by the large PTV margin whereas the probability of missing the CTV is higher in IGRT due to smaller PTV margins used. This is illustrated in figure 5.1.

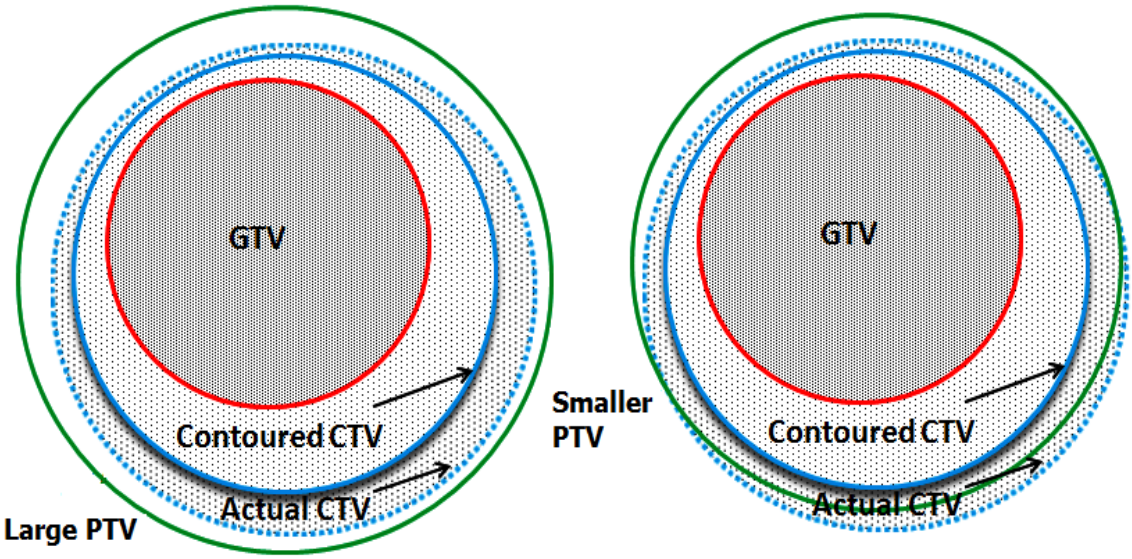

Figure 5.1: Illustration of a scenario where CTV is inaccurately delineated and its consequences in a)conventional radiotherapy with large PTV margin and in b)image-guided radiotherapy where smaller margins are employed

Another important point to be considered regarding the distribution of clonogenic cells is the effect of *extra-CTV tumour islets* on treatment outcome. Low density tumour islets outside the CTV are not easily detectable by current imaging modalities. In some cases the extra-CTV tumour islets can be eradicated by the incidental dose outside the PTV due to the nature of photon beam irradiation, whereas in other cases they may be missed. Witte *et al* [65] have shown in a multi-centric retrospective analysis of prostate treatments that patients who had local failure had different beam orientations than others where the beams did not pass through the areas where microscopic disease extension is expected. Thus the treatment outcome is highly influenced by the probability of these extra-CTV islets being eradicated by incidental dose.

The work presented in this chapter briefly discusses three important issues on treatment outcome using TCP modelling:

(a) Possible PTV margin reduction if the clonogen distribution in the GTV-CTV region is found to be less than in the GTV

(b) Consequences of using small PTV margins in IGRT treatments where accurate CTV extent is unknown

(c) Effect of extra-CTV islets and incidental dose on TCP

Due to time constraint, the work presented in this chapter is not complete but provides useful insights into the issues surrounding the PTV margins, clonogen distribution and their effect on treatment outcome.

5.2 Decreasing clonogen density in GTV-CTV region and the required PTV margins

5.2.1 Material and methods

To study the effect of decreasing clonogen density distribution in the GTV-CTV region on TCP and PTV margin, an exponential clonogen distribution with different degrees of fall off from the boundary of the GTV is assumed. The clonogen density distribution is calculated using equation 5.1. The radius of the GTV and CTV is 20 and 25 mm respectively. The total number of clonogens in all the cases within the CTV is set constant by adjusting the density of the clonogenic cells. The distribution of clonogenic cells from the boundary of the GTV is shown in figure 5.2 for three different slopes. For the slope factors of 0.5 and 1.0 the density is near zero at the boundary of the CTV whereas it is considerably higher for slope factor of 3.0.

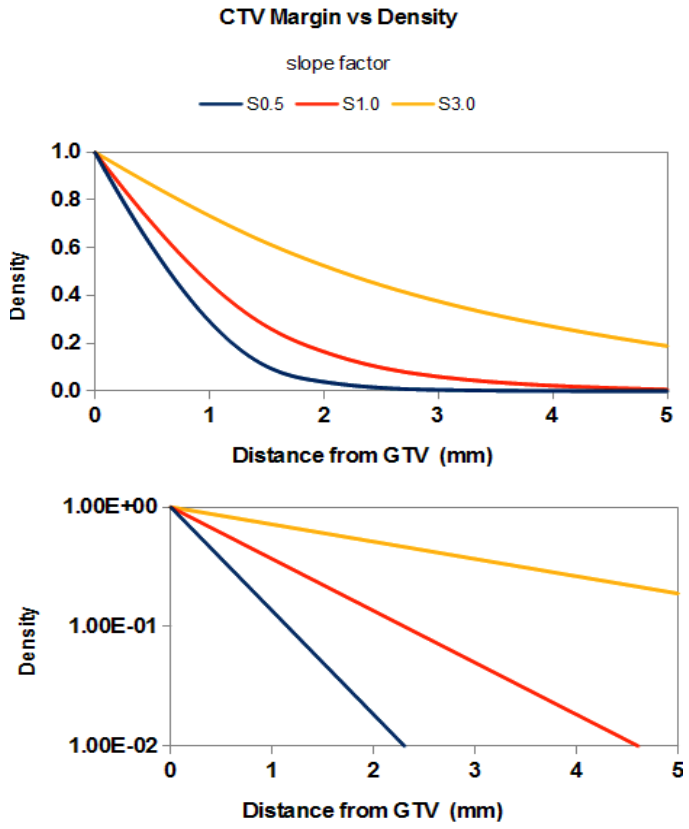

Figure 5.2: Exponential clonogen density distribution from the edge of the GTV in normal (top) and semi-log (bottom) scales

$$\rho_{cl}(r) = \exp(-r/s) \tag{5.1}$$

where ρ_{cl} is the clonogen density, r is the distance from the edge of GTV and s is the slope factor.

TCP calculation inclusive of geometric uncertainties and clonogen density distribution

A spherically symmetric dose distribution as discussed before is used for simulating the effect of geometric uncertainties on TCP with an exponentially decreasing clonogen density in the GTV-CTV region. Four different combinations of high and low systematic (Σ) and random (σ) errors were used for the simulations. The PTV margin was varied from 0 (no PTV margin) to 10 mm. The prescription dose was selected to obtain 50% TCP for the static case in 20 fraction treatment. Average dose-response slope was assumed for the TCP calculations (σ_α=0.07 Gy^{-1}). The dose in each voxel in each fraction is summed for the give Σ and σ for the entire course of treatment as described in chapter 3. The voxel control probabilities (VCP) for each voxel is calculated from the accumulated voxel dose values and their corresponding clonogen density (ρ_{cl}) from the exponential function. The rest of the TCP calculation is performed similar to CTV with uniform clonogen density distribution. The simulations were performed as mentioned in chapter 3 for different combinations of systematic (Σ) and random (σ) errors namely (1,1), (1,3), (3,1), (3,3). Simulations were repeated until the standard error of the mean population TCP ($\overline{TCP}$) is $\leq$0.15.

5.2.2 Results and discussion

The results showed a similar trend as observed for the uniform clonogen distribution except the required margins for $\leq$1% loss in mean population TCP are considerably smaller except for the slope factor of 3.0. Larger margins required for slope factor of 3.0 is due to the reason that more number of clonogens will be missed due to displacements as the clonogen density is greater at the outer edge of the CTV compared to slope factors of 0.5 and 1.0.

Table 5.1: Margins (mm) for $\leq$1% loss in $\overline{TCP}_{pop}$ for different combinations of systematic and random errors (Σ, σ) compared with exponential decrease in clonogen density from GTV and a uniform clonogen density in the CTV.

Slope	(1,1)	(1,3)	(3,1)	(3,3)
0.5	0.0	0.5	2.0	4.0
1.0	0.0	1.4	3.0	5.5
3.0	0.8	2.5	4.0	6.3
uniform density	1.8	3.5	5.0	6.3

However, for large geometric uncertainties ($\Sigma, \sigma = 3mm$) the margins with an exponential and uniform distribution of clonogens are almost same. This shows that geometric uncertainties are a dominant factor in deriving margins. This also highlights

the importance of reducing geometric uncertainties in radiotherapy.

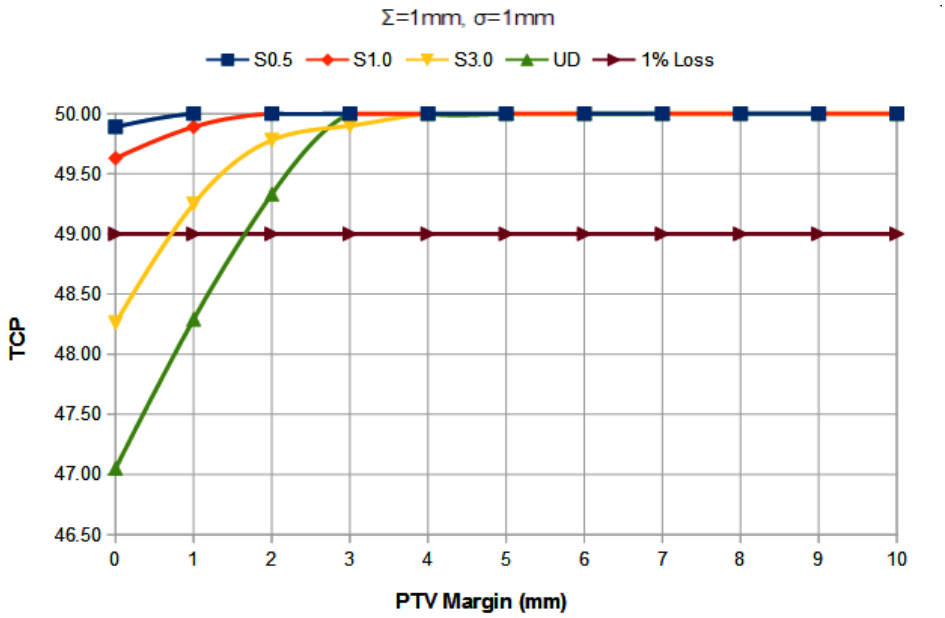

Figure 5.3: $\overline{TCP}_{pop}$ vs PTV margin for Σ=1mm and σ=1mm, compared with uniform clonogen density (UD) in the CTV

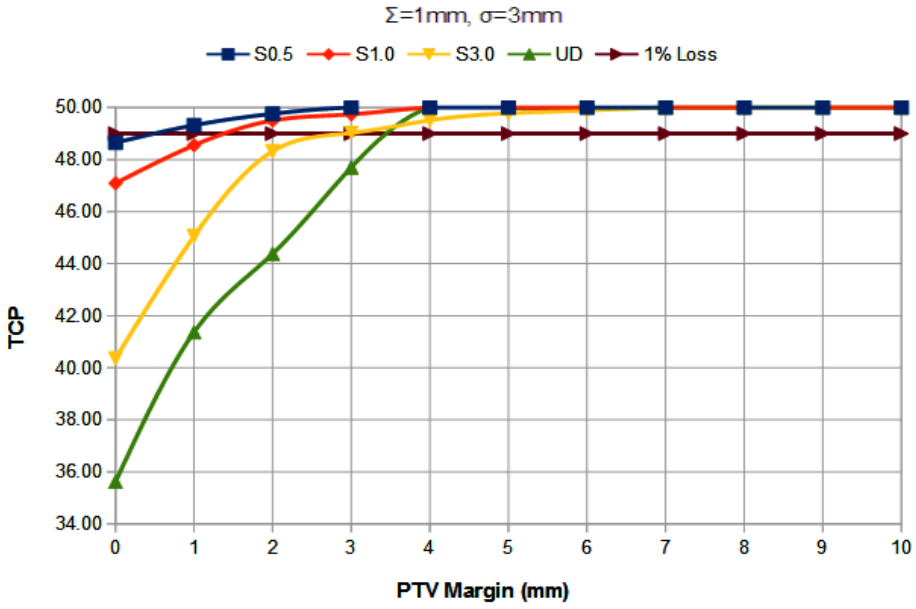

Figure 5.4: $\overline{TCP}_{pop}$ vs PTV margin for Σ=1mm and σ=3mm, compared with uniform clonogen density (UD) in the CTV

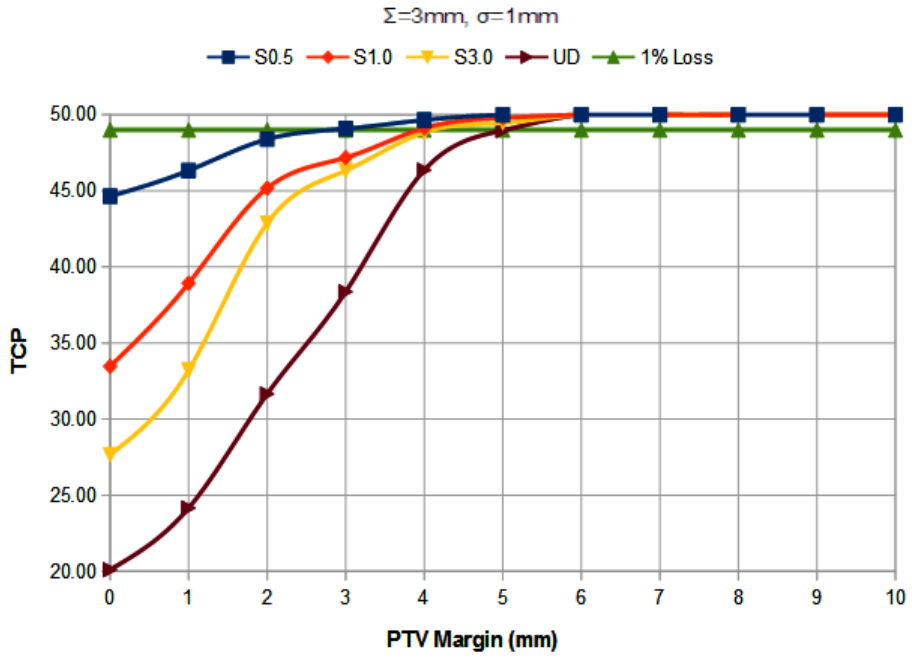

Figure 5.5: $\overline{TCP}_{pop}$ vs PTV margin for Σ=3mm and σ=1mm, compared with uniform clonogen density (UD) in the CTV

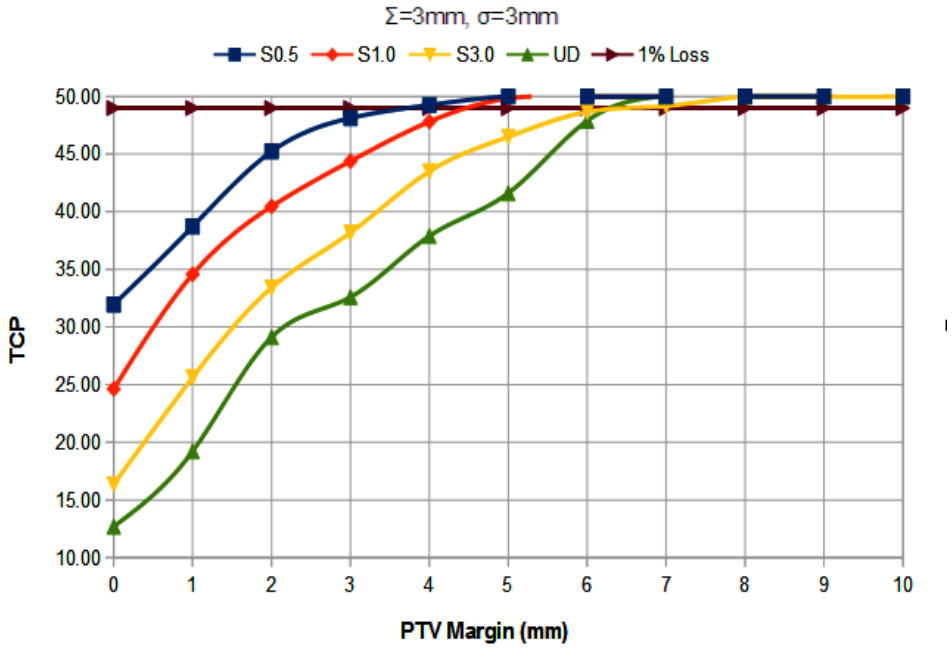

Figure 5.6: $\overline{TCP}_{pop}$ vs PTV margin for Σ=3mm and σ=3mm, compared with uniform clonogen density (UD) in the CTV

5.3 Risk of using smaller PTV margins

To demonstrate the risk of using smaller PTV margins in IGRT treatments where CTV extent is not precisely known, a cosine clonogen distribution is assumed. A cosine

distribution is chosen because the density of the clonogens can be made zero at the edge of the CTV whereas it is non-zero in a exponential case. The cosine distribution is calculated using equation 5.2. The resulting distribution for GTV-CTV distances of 5, 10 and 15 mm are shown in figure 5.7. Two different scenarios are assumed a)Treatment where the systematic (Σ) and random (σ) errors are both 1 mm with a PTV margin of 2mm as might be used with IGRT b)Conventional treatment with standard imaging protocol with Σ and σ of 3mm with a PTV margin of 8 mm. A GTV-CTV distance of 5 mm is assumed and the cosine clonogen density is calculated for the corresponding voxels using equation 5.2.

$$\rho_{cl}(r) = \cos(-r/d(\pi/2)) \tag{5.2}$$

where ρ_{cl} is the clonogen density, r is the distance from the GTV edge, d is the distance between the GTV and CTV.The prescription dose for both scenarios were set to achieve 50% for the static cases. Mean population TCP ($\overline{TCP}_{pop}$) was calculated inclusive of geometric uncertainties as described previously. Later, the CTV size is increased to 26, 27 and 28 mm. The PTV margins were kept same for both conventional and IGRT treatments. The resulting TCP loss relative to the static case are shown in figure 5.8.It is evident from figure 5.8 that the TCP loss is greater in IGRT treatments with smaller margins if the CTV extent is inaccurate, whereas in conventional treatments where large margins are employed the uncertainty in CTV definition can be accounted by the PTV margins. For the conventional case for a 3 mm larger CTV the TCP loss is $\sim$3% whereas it is $\sim$9% for the IGRT. The TCP loss in conventional case is gradual but it is abrupt in case of IGRT. This demonstrates the importance of accurate CTV definition to achieve high local control of tumour where smaller margins are employed. Heemsbergen *et al* [115] have shown that rectangular fields are associated with lower risk of local tumour progression compared to patients treated with conformal fields in high risk prostate patients. This raises the question whether the poorly known microscopic disease is not defined accurately in the conformal fields or the microscopic disease is incidentally eradicated by the large rectangle fields. In another study Witte *et al* [65] have shown incidental dose in regions where microscopic spread could be expected is found to be the reason in patients without local failure in high risk prostate patients. It should be noted that the potential margin reduction using IGRT is limited by the accuracy of the CTV definition. Accurately detecting microscopic disease is impossible, for instance even positron emission tomography (PET) has a resolution of 5 mm whereas the microscopic disease can be much smaller than this. Thus, even with the latest functional imaging it is impossible to detect microscopic disease accurately. There are other issues with CTV definition such as inter and intra observer variation in delineating the CTV. The same radiation oncologist will delineate the CTV differently on the same CT image at different occasions. As mention in an editorial article by

Marcel van Herk [116] IGRT has the potential to greatly reduce the uncertainties in treatment delivery but it cannot reduce the biological uncertainties. Hence, any margin reduction should be carefully evaluated and smaller margins should be employed with caution.

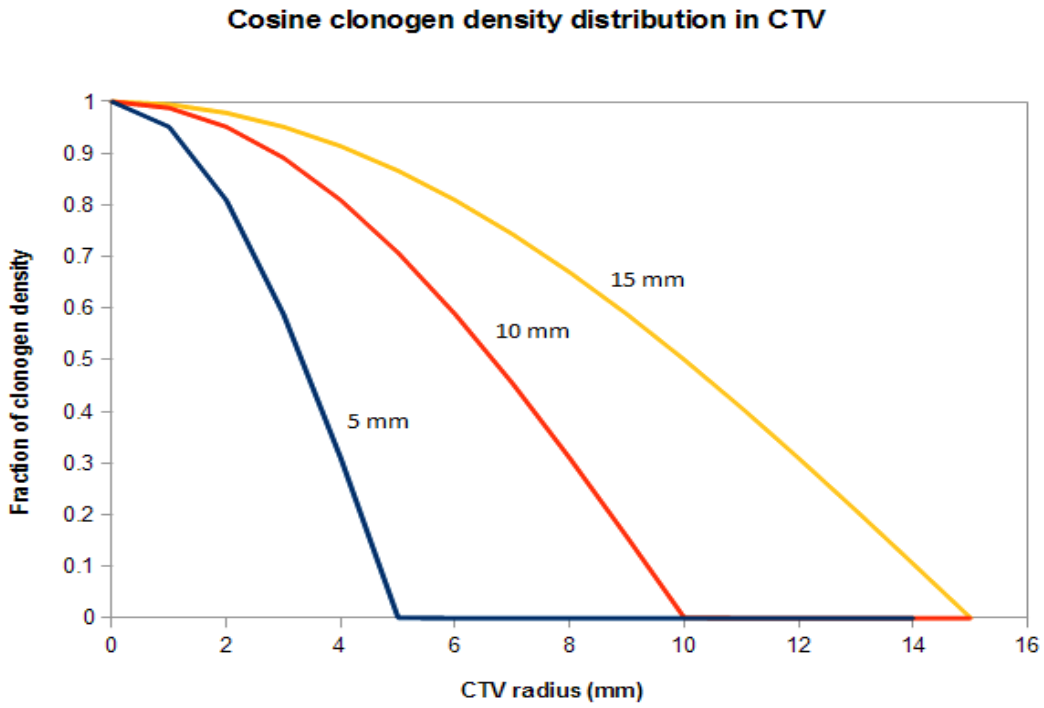

Figure 5.7: Cosine clonogen distribution in a CTV shell of 5, 10 and 15 mm radius

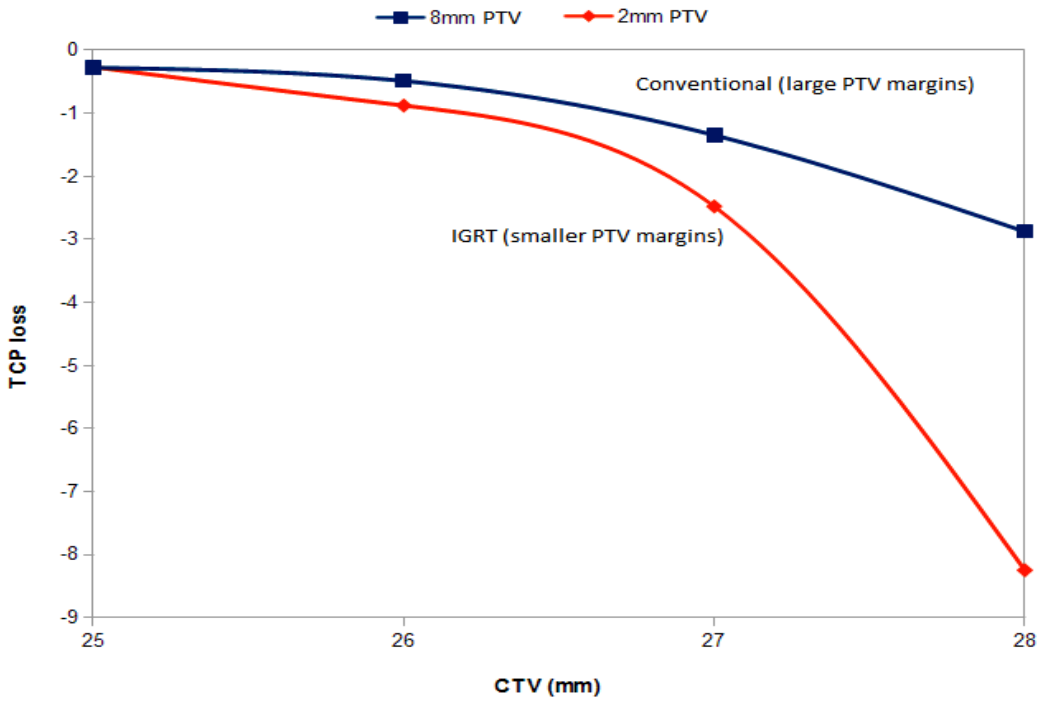

Figure 5.8: TCP loss for different CTV sizes in conventional and IGRT scenarios

5.4 Extra CTV islets and TCP

To study the effect of extra-CTV tumour islets on TCP and dose-response curve an anonymized prostate IMRT treatment plan with five fields is used. Figure 5.9 show the chosen plan with axial dose distribution and the CTV. Five tumour islets were randomly distributed outside the CTV within a margin of 3 cm. The diameter of the each islet is 3mm. These values are taken from van Loon *et al* [63]. A random instance of five islets distributed around the CTV is shown in figure 5.10. The clonogen density of each islet is calculated using the exponential form given in equation 5.1 using the distance between the centre of the islet to the closest edge of the CTV with a exponential factor of 0.5. The prescription dose was rescaled to 32 Gy and the TCP was calculated using an average dose-response slope (σ_α=0.07 Gy^{-1}). The TCP calculation was repeated 10 times to get an average TCP by randomly distributing the islets. The dose was then increased up to 102 Gy in steps of 5 Gy to obtain the dose-response curve with extra-CTV islets. Obtained dose-response curves for both with and without islets are shown in figure 5.11.

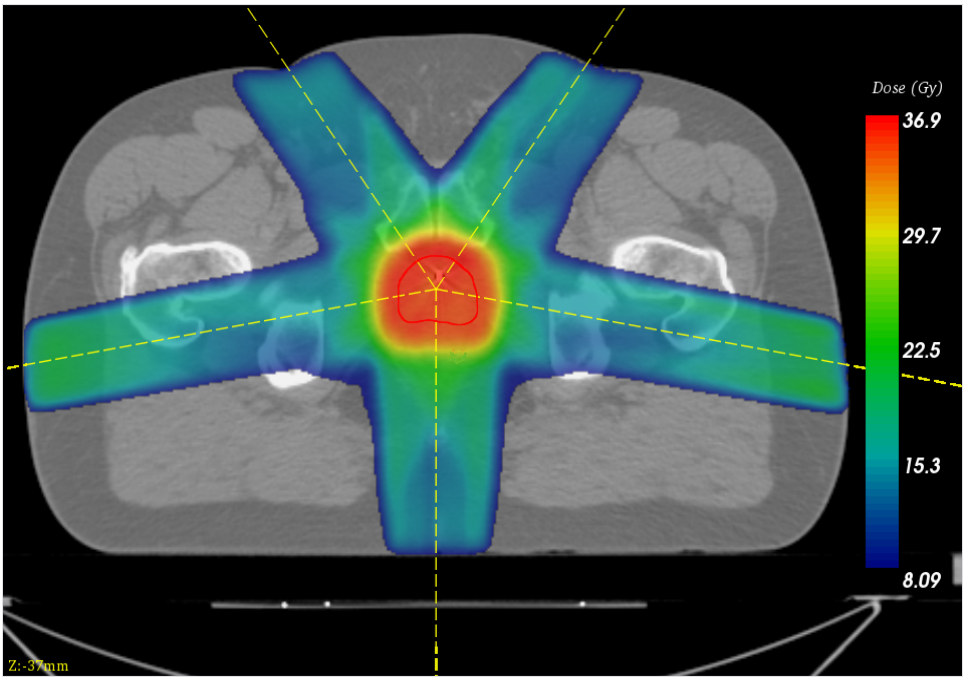

Figure 5.9: IMRT plan with axial dose distribution and the CTV used for simulating the effect of extra-CTV islets on dose-response curve

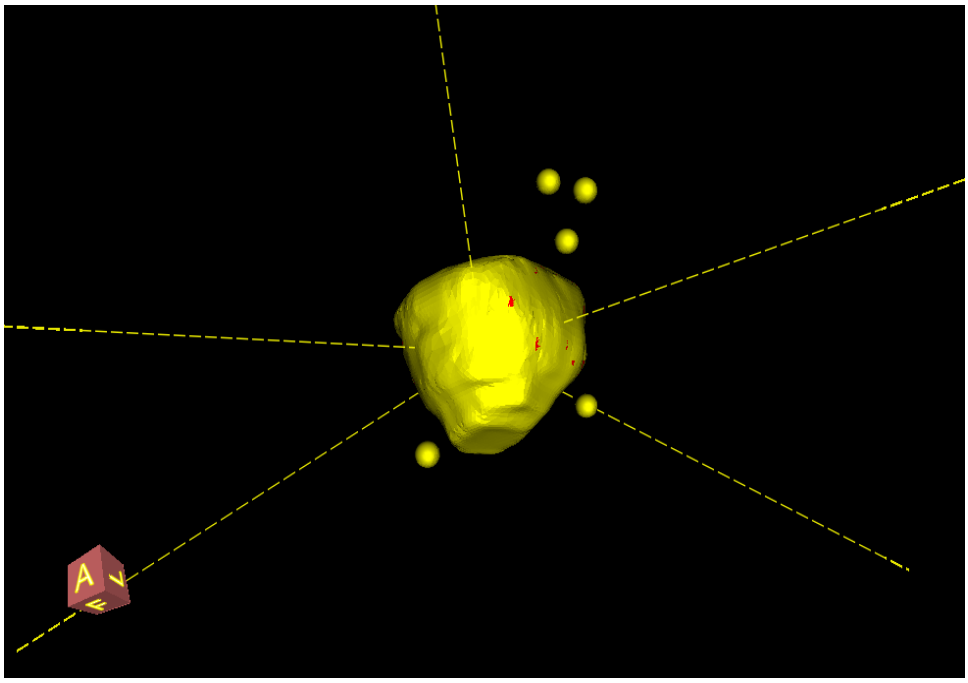

Figure 5.10: Randomly distributed islets outside CTV shown along with the CTV

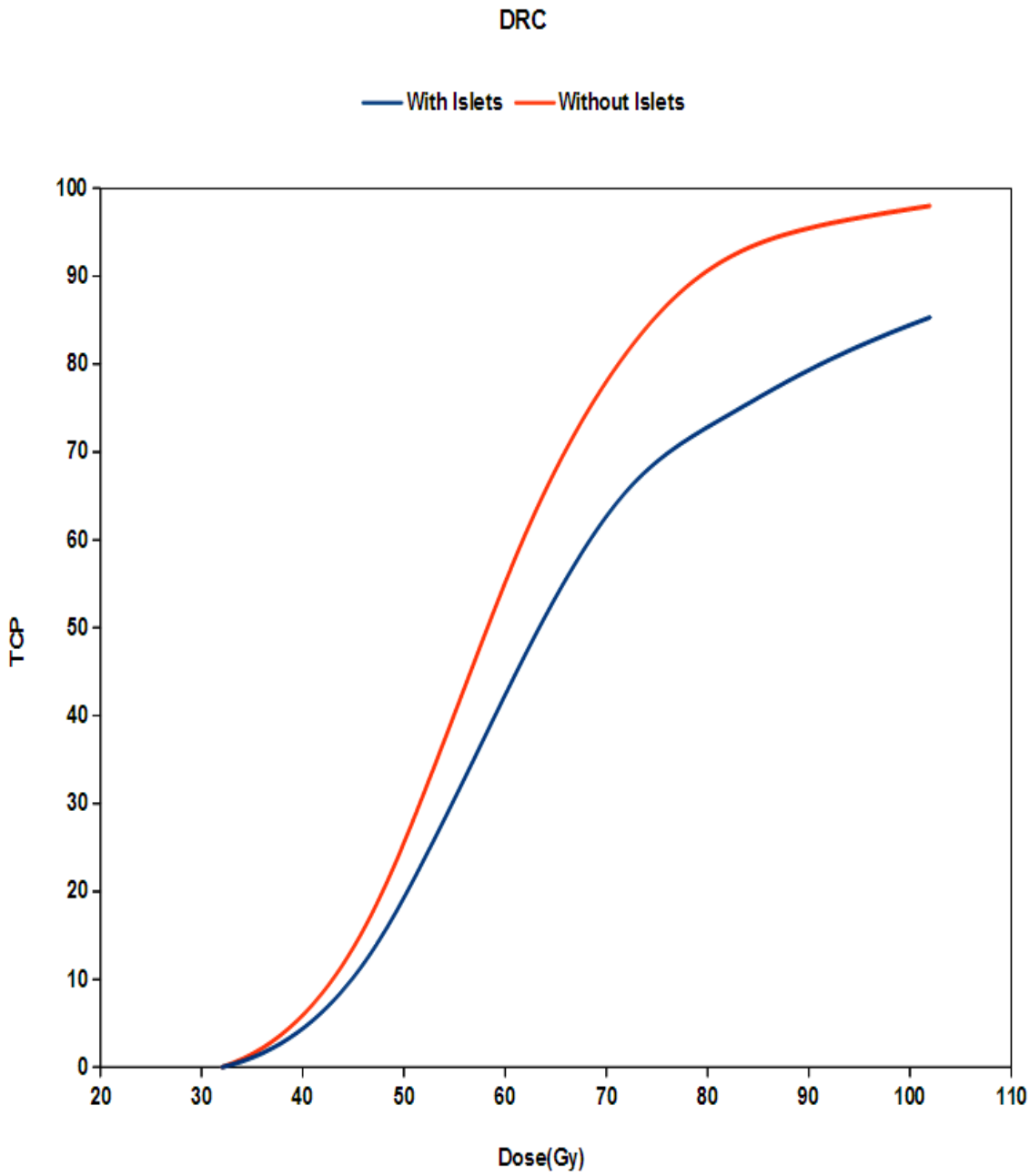

Figure 5.11: Dose-response curve with and without islets outside the CTV.

The dose-response curve observed with islets showed a normal sigmoid shape, however the dose-response curve with islets showed a biphasic sigmoidal shape (i.e. combination of two sigmoidal curves). In some cases where extra-CTV islets are found, it is possible to eradicate the islets by escalating the prescription dose which in turn will increase the dose outside the PTV (incidental dose). If by chance these islets are in the beam path ways close to the CTV, they can be killed by the incidental dose. On the other hand, if these islets are found some where out of beam paths, 100% TCP cannot be achieved by simply escalating the dose. This opens up a debate on how this concern of microscopic disease affects other treatment modalities such as VMAT, Cy-

berknife and proton therapies which have a much more conformal and have steep dose gradients than conventional photon beam irradiation. VMAT treatments have a more uniform dose fall off (spherically symmetric) than static field IMRT and hence VMAT treatments are more likely to eradicate microscopic tumour islets within the vicinity of the tumour. However, there are other factors such as number of beams, their gantry angles, dose constraints and their priorities used in the optimization process which decides the dose fall off in a given region in space. As far as Cyberknife is concerned, it is mostly used for lower stage and well localized diseases. In such cases, the probability of microscopic disease is very less and is of less concern for local control. Coming to protons and other ion beam therapies which are more conformal and have the capability to produce steeper dose gradients than photon beams, the risk of lowering the local control is higher compared to photon beam therapy if the CTV is not accurately defined. Its too early to derive to a conclusion on this issue as there are too may factors which determine the effect of microscopic disease on local control in different treatment techniques. Therefore a much more detailed studies are required, either insilico simulations or retrospective clinical analysis of these issues such as Heemsbergen *et al* [115] and Witte *et al* [65]. Nevertheless, it is clear that higher conformal treatments require greater attention to biological uncertainties than conventional treatments which has taken care of these biological uncertainties up to some extent by generous PTV margins used. Dose escalation is also beneficial only if the microscopic disease is accurately known.

Chapter 6

4D Radiobiological modelling of the interplay effect in conventionally and hypo-fractionated lung tumour IMRT

6.1 Introduction

6.1.1 Lung motion

Lung is responsible for transporting oxygen from the atmosphere into the bloodstream and carbon dioxide from bloodstream to the atmosphere, a process called as respiration. Respiration is an involuntary action, however individuals can have control over the frequency, displacements and breath hold. There are several other organs including esophagus, liver, breast, kidneys, pancreas and prostate known to move with breathing. Patients' breathing patterns have been shown to vary in magnitude, period and regularity from time to time (i.e., may be different between imaging and treatment delivery) [117–120]). However, studies have shown that the respiration reproducibility can be improved by audio-visual biofeedback [119–121]. The magnitude of tumour motion has been shown to be independent of tumour size, its location and pulmonary functioning suggesting that tumour motion should be assessed individually for each patient [122]. There is an extensive list of publications which have reported lung motion using numerous imaging modalities including ultrasound [123–125], CT [19, 126–128], MR [129] and fluroscopy [130–136]. The findings of some of these studies are given in table 6.1.

Table 6.1: Range of lung motion observed in different studies in different parts of the lung with mean (min- max) in mm (*left blank where information was not reported*)

Observer	SI	AP	LR	Imaging modality
Roos *et al* [19] (*upper lobe*)	-	1(0-5)	1(0-3)	CT
Roos *et al* [19] (*middle lobe*)	-	0(0-5)	9(0-16)	CT
Roos *et al* [19] (*lower lobe*)	-	1(0-4)	10.5(0-13)	CT
Barnes *et al* [131] (*lower lobe*)	18.2(9-32)	-	-	fluroscopy
Barnes *et al* [131] (*middle,upper lobe*)	7.5(2-11)	-	-	fluroscopy
Seppenwoolde *et al* [137]	5.8(0-25)	2.5(08)	1.5(0-3)	fluroscopy
Sixel *et al* [134]	(0-13)	(0-5)	(0-4)	fluroscopy
Grills *et al* [135]	(2-30)	(0-10)	(0-6)	fluroscopy
Murphy *et al* [133]	7(2-15)	-	-	fluroscopy
Chen *et al* [130]	(0-50)	-	-	fluroscopy
Plathow *et al* [129] (*upper lobe*)	4.3(2.6-7.1)	2.8(1.2-5.1)	3.4(1.3-5.3)	MR
Plathow *et al* [129] (*middle lobe*)	7.2(4.3-10.2)	4.3(1.9-7.5)	4.3(1.5-7.1)	MR
Plathow *et al* [129] (*lower lobe*)	9.5(4.5-16.4)	6.1(2.5-9.8)	6.0(2.9-9.8)	MR

The results from the literature leads to the conclusion that every patient's breathing pattern is unique and no biomathematical models can predict the motion of lung tumours prior to observing their motion. Many patient characteristics involved in breathing of a particular patient such as quiet vs deep, chest vs abdominal and patient general health condition makes it unpredictable using mathematical models. It should also be noted that most of the lung tumour displacements (with an exception to Seppenwoolde *et al* [137] where the displacements are measured using implanted gold markers) reported in the literature are measured using tumour surrogates such as diaphragm motion or infrared markers placed on the patient chest or abdomen. The displacements measured using surrogate markers do not correlate with the actual lung tumour motion.

6.1.2 Respiration and interplay effect

Respiration-induced organ motion represents a serious challenge regarding the accuracy of dose delivery in radiotherapy and its impact on clinical outcome. Lung tumours are the most common tumours affected by respiration-induced motion, and local failure (approx. 70% of the cases) is considered as a major cause of tumour-related death. Studies have highlighted the importance of dose escalation for improving local control in non-small-cell lung tumours (NSCLC) [138, 139]. Since intensity-modulated radiotherapy (IMRT) has the potential to deliver higher doses with fewer normal tissue

complications [140], IMRT is often used nowadays to treat lung tumours. Moreover, hypofractionated treatments have been shown to result in better clinical outcomes for medically inoperable early-stage lung tumours [57, 141–143]. Better targeting accuracy coupled with superior normal tissue sparing and higher dose conformality especially with smaller treatment fields used in stereotactic treatments, allows clinicians to prescribe extremely high doses in very few fractions ($\sim$ 3). With the advent of image-guided radiotherapy (IGRT) this type of treatment is becoming increasingly common for lung radiotherapy. However in MLC-based IMRT delivery, the '*interplay*' between the respiration-induced tumour motion and the movement of MLC leaves can result in undesired motion artifacts in dose delivery [38, 144]. Consequently motion management or correction techniques such as tumour tracking or gating have been suggested for treating moving tumours with IMRT [145–148]. It should also be noted that lung tumours have one of the steepest dose-response curves ($\gamma_{50} = 3.9$) [104] which means that a small change in dose results in a relatively large change in TCP. Although motion management techniques are currently available, it may not be possible to use such techniques for each patient either due to time or resource constraints. Thus it is important to understand and quantify the effect of tumour motion in IMRT treatments i.e. the 'interplay' effect, in the absence of tumour tracking or gating. By quantify we mean not only in terms of absorbed dose, a purely physical quantity, but more importantly in terms of changes in the probability of local tumour control.

Several studies have investigated the effect of respiration-induced tumour motion on IMRT treatments [38–45]. Jiang *et al* [39] have investigated the effect of interplay for three different modes of IMRT delivery (step-and-shoot with 10 and 20 intensity levels, sliding window) using a 0.6cc farmer chamber positioned at the centre of the tumour in a moving phantom. They found that the mean dose to the moving tumour for all the fields varies $< 2-3\%$, but it could be as high as 30% for a single field. They have also shown that the variation in dose is insensitive to the mode of delivery and the dose differences due to interplay decrease as the number of treatment fractions becomes large (~ 30). This has been previously emphasized by Bortfeld *et al* [38] who showed by statistical analysis that the mean dose to a moving tumour is insensitive to the delivery technique and the standard deviation in dose for a 30-fraction treatment is generally $< 1\%$ of the mean dose. However, the conclusion derived from point-dose measurements by Jiang *et al* does not provide a complete picture of the interplay effect to the overall tumour volume. Using 2D film measurements, Berbeco *et al* [149] have shown that the standard deviation of the dose to a pixel inside the target volume can be as high as $2-4\%$ for single fraction treatments which correspond to stereotactic radiosurgery, although the effect is reduced to 0.4-0.7% with 30 fractions. According to their measurements, the maximum dose in the target varies $< 1\%$ while the minimum dose varies up to $\sim 6\%$. This indicates that there could be considerable underdosage of the target volume even for treatments with large number of fractions and the effect of interplay is significant

for hypofractionated treatments. In a recent study by Zhao *et al* [150] in a 3 fraction treatment, the results showed that the CTV could be considerably underdosed due to the interplay effect in a Cyberknife treatment (Accuray, Sunnyvale, A). Furthermore, Seco *et al* [151] have emphasized that reduced dose errors due to interplay effect in many-fraction treatments will not apply to hypofractionated treatments.

While there are numerous studies addressing the issues of interplay effects in terms of *dose* variation in the tumour, studies quantifying the *clinical* significance of these dose variations are much rarer. Use of tumour control probability (TCP) as a metric would provide a more valuable insight into the true significance of the interplay effect. As mentioned by Niemierko [152], it would be interesting to know the clinical significance of "x" amount of dose error and "y" amount of geometric error rather than mere variation in the dose. Duan *et al* [42] have done a TCP analysis using a moving phantom and found the TCP changes to be 2.3% and 4.3% for five- and single- fraction treatments. However, the volume of the target used in their study is fixed (4.5 cm diameter sphere). TCP values could significantly differ with the volume of the target even for the same prescribed dose. Moreover, the TCP values provided were not calculated from a large number of simulations, which raises concern over its applicability for a population of patients.

In this study we use real patient datasets (3D CT image, plan information) covering a range of tumour volumes (31cc to 172 cc) and a 4D dose model which provides 3D voxel-by-voxel dose accumulation in the target volume inclusive of intrafraction organ motion for step-and-shoot IMRT. This dose model takes into account the number of treatment fractions, and radiobiological characteristics of lung tumours (γ_{50}) for TCP calculations. Though the dose computation algorithm is fairly simple, it is robust enough to simulate the interplay effect in patient geometry. Moreover, a population mean TCP ($\overline{TCP}_{pop}$) calculated from large number of simulations for each plan, is used in this study and provides more statistically reliable TCP values. To obtain the final dose to a particular voxel, the dose computation is performed for each fraction for each beam segment. Inhomogeneity and scatter effects have been ignored to enable the dose computation algorithm to accumulate the dose in each voxel over a fractionated treatment in a reasonable time. The methodology described here is easy to extend to other delivery techniques and could also be extended to account for scatter and for heterogeneous tissue density using more sophisticated dose calculation algorithms such as the one provided by Yang *et al* [153].

6.2 Material and Methods

A 20-fraction, 3-fraction and an extremely hypofractionated case of one-fraction treatment were considered for the analysis. MUs for the single and 3-fraction treatment were scaled from the 20 fraction plan to give a TCP around 50% (within the linear

portion of the dose-response curve, in order to be in the steepest portion of the TCP curve). This is around 8 Gy for single fraction, because the volume of target volumes differed between patients. So a different dose was required or each patient to get 50 % TCP. Since we are not aiming for ¿90% TCP as achieved in SABR a low dose was sufficient to achieve 50% TCP. A simulation is the total dose distribution obtained by the accumulation of dose over the course of full fractionated treatment for a given patient. Several simulations are performed per patient to calculate individual TCP.

6.2.1 Lung tumour motion simulation

Lung tumours tend to move in an elliptical path [137] rather in a one-dimensional cranio-caudal (CC) direction. As mentioned before patient breathing pattern is complex and varied from patient to patient. It can neither be predicted before observing the breathing pattern of an individual patient's breathing using either fluroscopy or 4D CT. Hence a one-dimensional lung motion with a sinusoidal pattern in the CC direction which is a good approximation is assumed here. The position of tumour at time t is given by equation 6.1.

$$P(t) = Asin(wt + \phi) \tag{6.1}$$

where A is the peak deviation from the centre position of the tumour, w the angular frequency and ϕ is the phase in radians at which breathing starts.

A clockwise-delivery is assumed to map the tumour position for each beam and segment. Since breathing is involuntary and uninterrupted while leaves change their position to the next segment or gantry moves to the next beam angle, the time elapsed during these processes is accounted for while calculating the tumour position for each segment for the given beam angle. A gantry speed of $60s$ for full rotation and a time duration of $1s$ between segments is assumed. Even though breathing motion is continuous, dose calculation is done using a discretized (1 position/segment) time-averaged position $P(\bar{t})$ using equation 6.2. The parameters used for the tumour motion calculation are given in table 6.2. The range of tumour displacement in the cranio-caudal direction reported in the literature ranges from 4.3 [129] to 18.2 [131] mm, hence an average of these which is close to 10 mm is used in this study. However, this can be varied in the model to simulate the real patient breathing pattern if known.

$$\bar{t} = \frac{t_{start} + t_{end}}{2} \tag{6.2}$$

where t_{start} and t_{end} are the start and end time for the given segment. If the segment has MU greater than 50 (corresponds to 1 respiratory cycle for the breathing parameters and doserate assumed), the dose is calculated by splitting the segment every 50 MU.

Table 6.2: Parameters used for motion simulation

Parameter	value
Amplitude (A)	10 mm
Period (T)	5 s
Dose rate	600 MU/min
Segment interval	1 s
Gantry speed	0.166 s/degree

The field arrangement for a representative lung IMRT plan is shown in 6.1. Splitting of beam into several segments for dose calculation including tumour intra-fraction movement is shown in figure 6.2. The beams are first sorted in a clockwise direction.

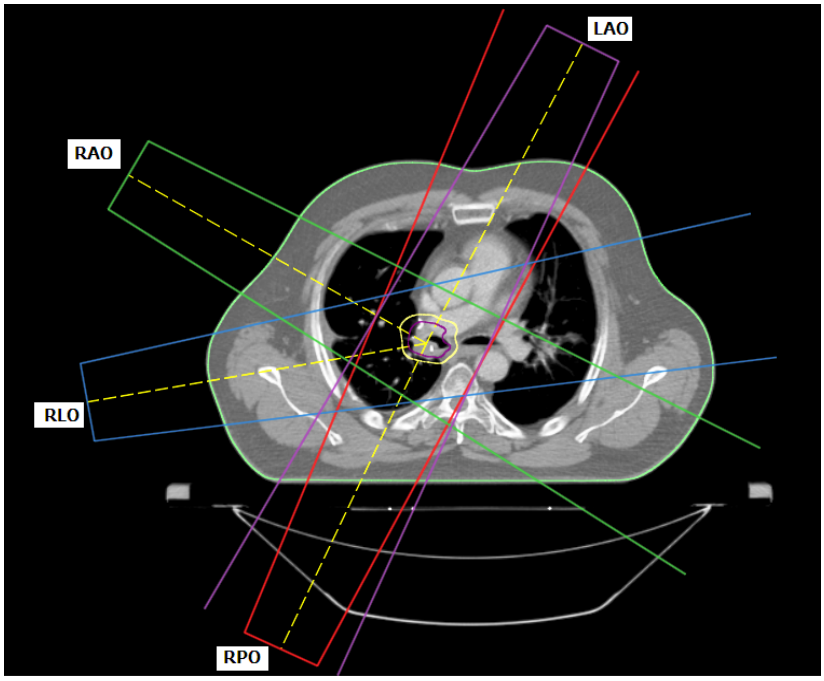

Figure 6.1: Beam arrangement for a four-field IMRT plan with CTV and PTV contours

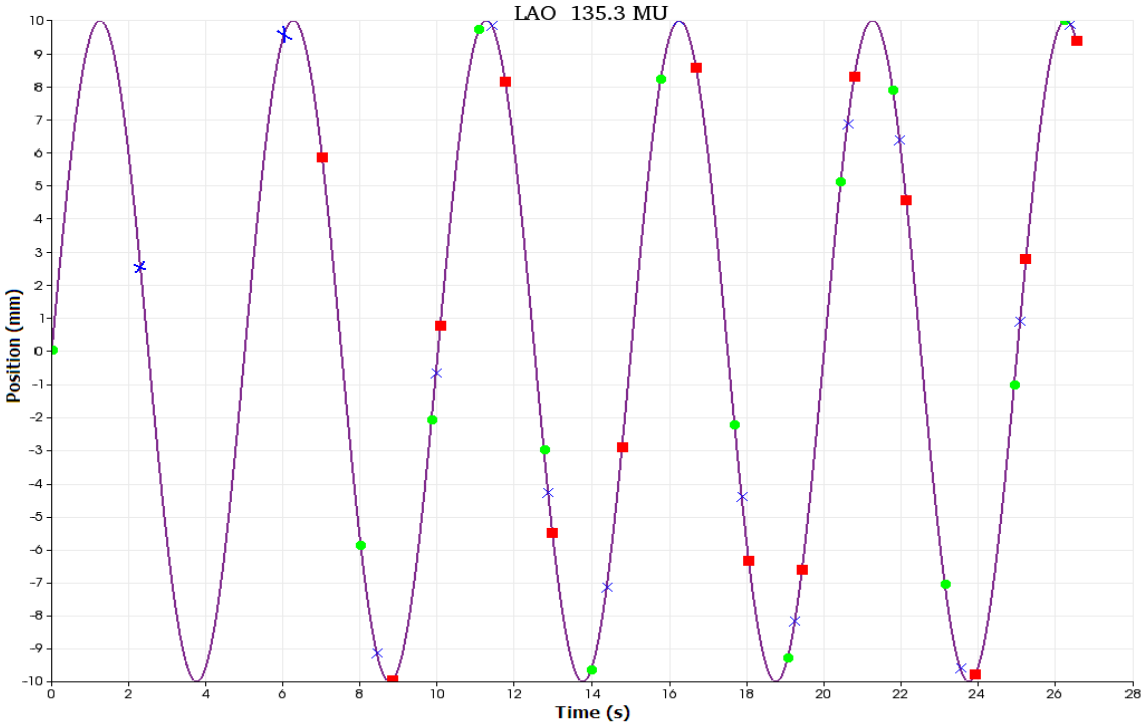

Figure 6.2: Mapping of mean tumour position $P(\bar{t})$ (indicated with a cross marker) for each segment for beam LAO. The green and red markers indicate beam' on' and 'off' respectively.

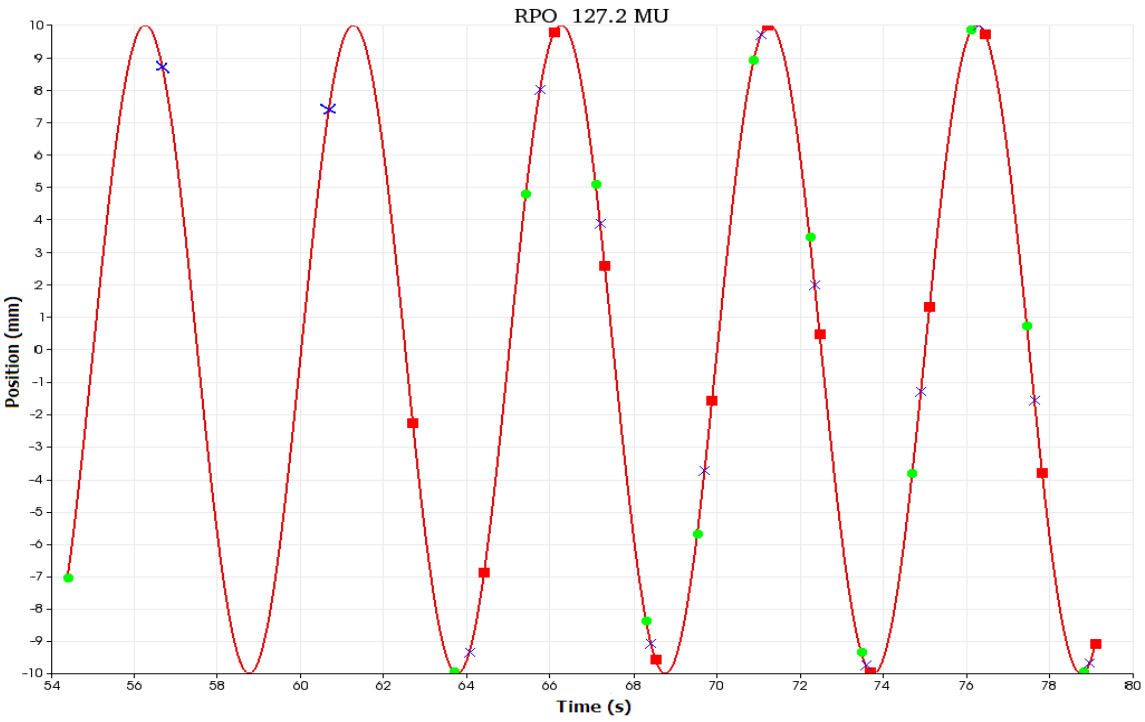

Figure 6.3: Mapping of mean tumour position for beam RPO

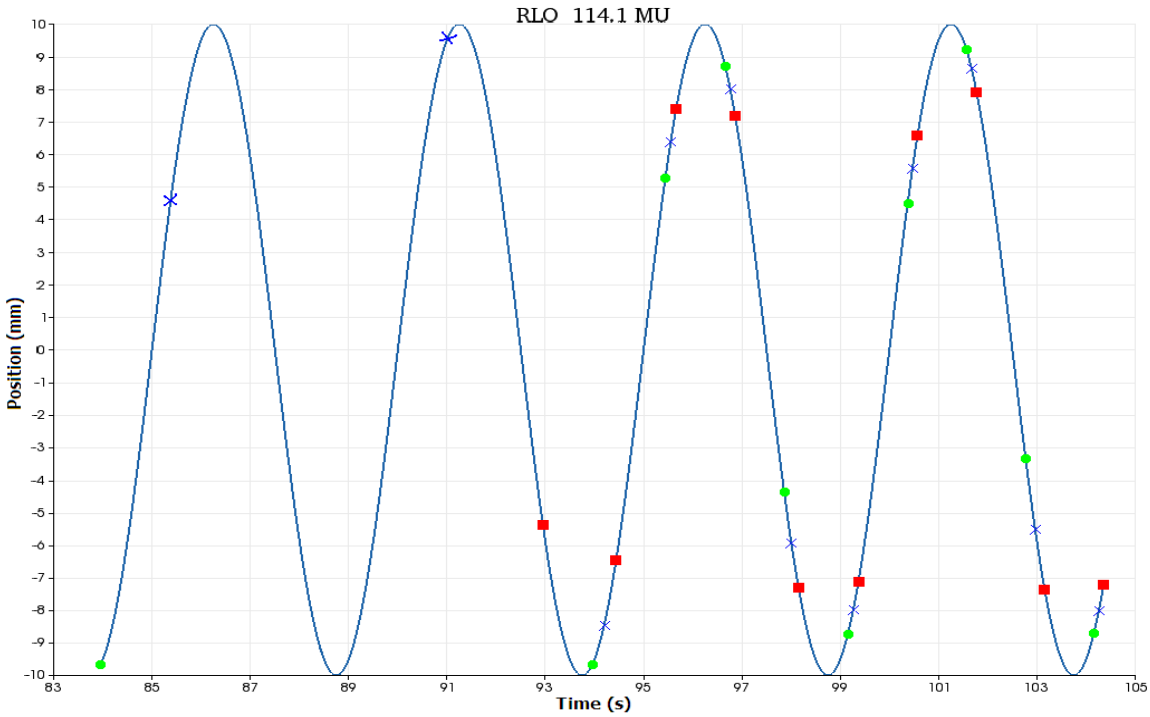

Figure 6.4: Mapping of mean tumour position for beam RLO

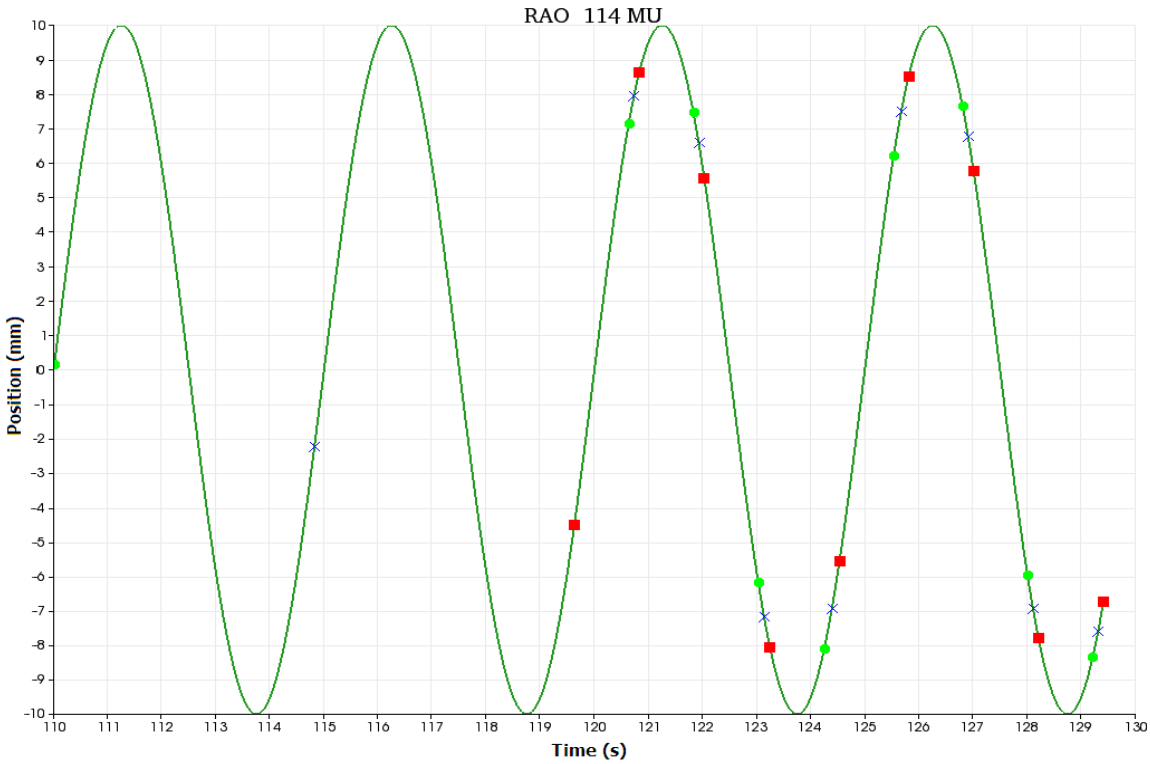

Figure 6.5: Mapping of mean tumour position for beam RAO

6.2.2 DICOM RT Plans

An in-house developed software is used to read the DICOM objects including CT, RT structures, RT dose, and RT plans. Three step-and-shoot IMRT plans generated using Eclipse's Dose-volume optimizer (DVO)(Varian Medical Systems, Palo, Alto) and three using Pinnacle's Direct machine parameter optimization (DMPO) (Philips Medical Systems, Madison) in a 6MV Varian 2100C/D with 120 leaf Millennium MLC are used for the analysis. Default number of 10 intensity levels is used for the Eclipse IMRT plans and the default value of 50 maximum number of total segments for the plan was used in Pinnacle's DMPO. The prescription dose was 55 Gy in 20 fractions for all the plans and the dose-volume constraints for the target and critical structures were set according to the clinical protocols in use at our centre. The PTV margin was 1 cm in all directions which is sufficient to account for 2 cm peak-to-peak tumour motion in the CC direction.

6.2.3 Radiological path length calculation

Ray tracing is widely used in computer graphics for virtual reality rendering. The same concept is used in radiotherapy applications for calculating the exact radiological path length (RPL). A patient 3D model is generally obtained from a set of greyscale 2D CT slices. The greyscale values which represent Hounsfield units (HU) of the voxels can be used to calculate the RPL by using the relationship between HU and relative electron density (RED). The HU is defined in equation (6.3).

$$HU = \left(\frac{\mu_{tissue} - \mu_{water}}{\mu_{water}}\right)1000 \tag{6.3}$$

where the μ_{tissue} and μ_{water} are the linear attenuation coefficient of tissue of interest and water respectively.

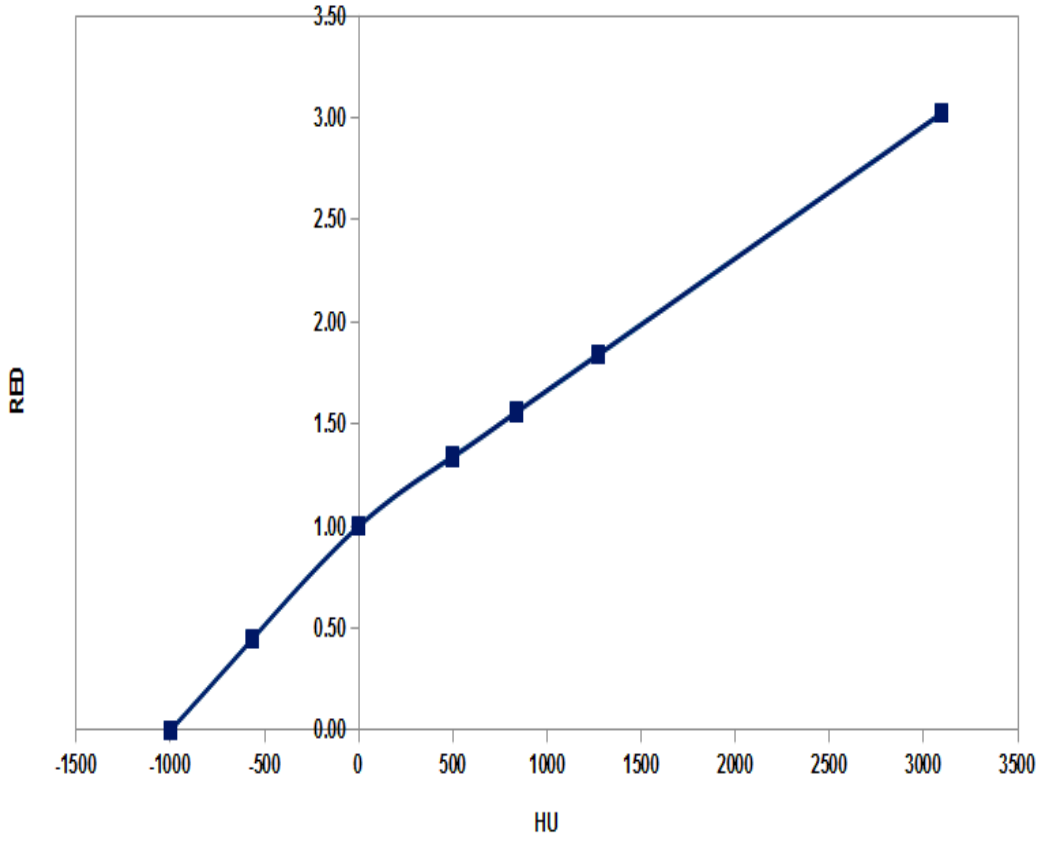

Figure 6.6: Relationship between HU and RED

Siddon's [154] ray tracing algorithm is widely used in radiotherapy for calculating RPL. A class named "RayTracer" has been developed for calculating the RPL based on Siddon's raytracing algorithm in Biosim. The relationship between HU and RED is shown in figure 6.6(*values are taken from the Pinnacle TPS for the CT scanner used at our institute*).

The raytracing algorithm treats a 3D CT image array as a set of orthogonally placed parallel planes with uniform spacing as shown in figure 6.7. By finding the ray line intersections in [X,Y,Z] planes, the voxel indices [*i,j,k*] through which the ray passes can be obtained. The length through the ray passed is given by $RPL_{voxel} = length_{voxel} * RED_{voxel}$. The total RPL for a ray vector can be obtained by summing the individual voxel RPLs through which the ray passes.

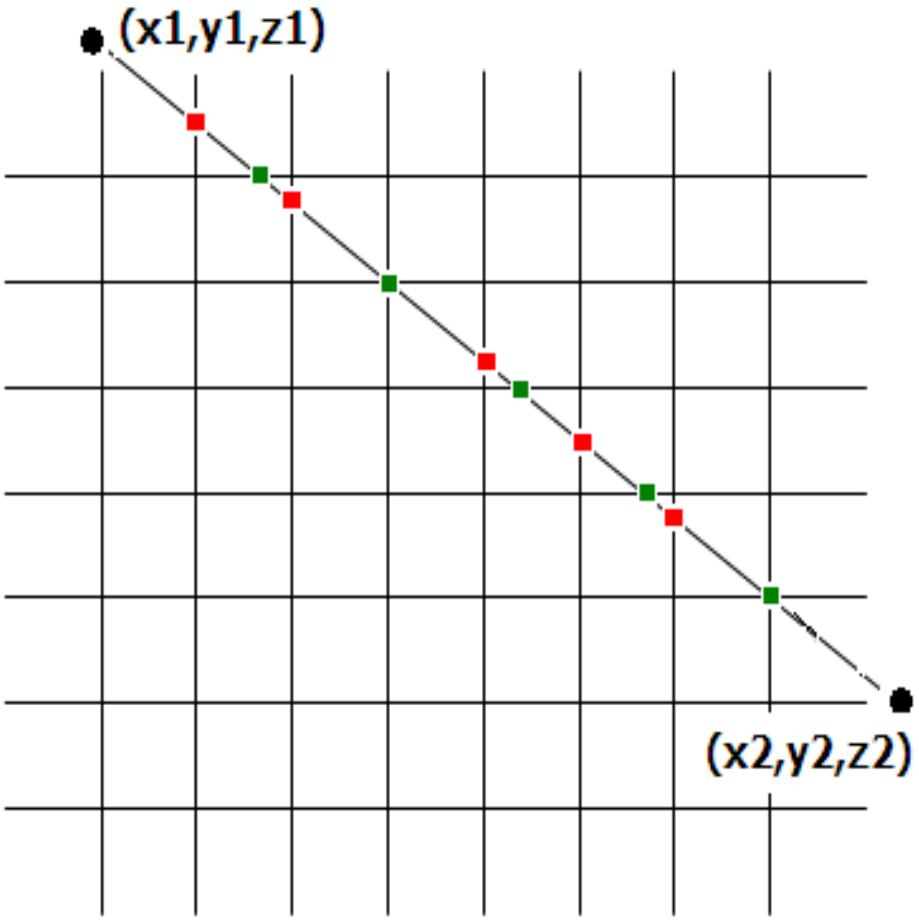

Figure 6.7: Raytracing through a set of orthogonal planes. Though the CT image is 3D, for the sake of simplicity only a 2D depiction is shown here. The red squares represent intersection with vertical and the green squares represent intersection with horizontal planes.

A ray can be parametrically represented as shown in equations (6.4).

$$x = x_1 + \alpha(x_2 - x_1) \tag{6.4a}$$

$$y = y_1 + \alpha(y_2 - y_1) \tag{6.4b}$$

$$z = z_1 + \alpha(z_2 - z_1) \tag{6.4c}$$

$\{x_1, y_1, z_1\}$ and $\{x_2, y_2, z_2\}$ are the position of the ray at source and the centre of the voxel of interest. α (*not to be confused with the radiobiological term*) is the distance traveled divided by the source-to-voxel distance. Now the image dataset can

be expressed in terms of α as shown in equation (6.5). Capital letters (X,Y,Z) indicate plane indices and d_x, d_y, d_z represent voxel spacing in the x,y and z axes. $\{x_0, y_0, z_0\}$ are the plane indices at $(i, j, k) = 0$.

$$X_i = X_0 + id_x \tag{6.5a}$$

$$Y_j = Y_0 + jd_y \tag{6.5b}$$

$$Z_k = Z_0 + kd_z \tag{6.5c}$$

Using equations (6.4) and (6.5) the α value at a ray-plane intersection can be calculated. Substituting (6.5) in (6.4) for x, the α value at a plane index can be calculated as shown in equations (6.6).

$$\alpha_x(i) = \frac{X_0 + id_x - x_1}{(x_2 - x_1)} \tag{6.6a}$$

$$\alpha_y(j) = \frac{Y_0 + jd_y - y_1}{(y_2 - y_1)} \tag{6.6b}$$

$$\alpha_z(k) = \frac{Z_0 + kd_z - z_1}{(z_2 - z_1)} \tag{6.6c}$$

Equation in (6.6) can be recursively written as shown in (6.7).

$$\alpha_x(i) = \alpha_x(i-1)\Delta\alpha_x \tag{6.7a}$$

$$\alpha_y(j) = \alpha_y(j-1)\Delta\alpha_y \tag{6.7b}$$

$$\alpha_z(k) = \alpha_z(k-1)\Delta\alpha_z \tag{6.7c}$$

Using (6.7) α can be calculated for all ray-plane intersections from the source and the target voxel. These are calculated individually for each axis and the set of α is stored as an array as shown in equation (6.8).

$$\{\alpha_x\} = \{\alpha_x(i_{min}).....\alpha_x(i_{max})\} \tag{6.8a}$$

$$\{\alpha_y\} = \{\alpha_y(j_{min}).....\alpha_y(j_{max})\} \tag{6.8b}$$

$$\{\alpha_z\} = \{\alpha_z(k_{min}).....\alpha_z(k_{max})\} \tag{6.8c}$$

where "min" and "max" are the first and last intersections of the ray with the orthogonal planes. Each term in the sets corresponds to a particular plane. Intersection of the ray will the voxels can be found from the merged dataset $\{\alpha\}$ which would become

$$\{\alpha\} = \{\alpha_{min}, merge[\{\alpha_x\}, \{\alpha_y\}, \{\alpha_z\}], \alpha_{max}\} \tag{6.9}$$

Two consecutive terms in $\{\alpha\}$ is associated with entering and leaving a voxel. Thus the length traveled in a voxel is given by (6.10).

$$l(m) = [\{\alpha\}(m+1) - \{\alpha\}(m)]d_{12} \tag{6.10}$$

where l(m) is the length traveled in voxel "m" and d_{12} is the distance from source to the target voxel calculated using equation (6.11).

$$d_{12} = \sqrt{(x_2 - x_1)^2 + (y_2 - y_1)^2 + (z_2 - z_1)^2} \tag{6.11}$$

The voxel indices through which the ray passes can be calculated using the α values as shown in (6.12)

$$i(m) = \left[\frac{x_1 + \alpha_{mid}(x_2 - x_1) - X_0}{d_x}\right] \tag{6.12a}$$

$$j(m) = \left[\frac{y_1 + \alpha_{mid}(y_2 - y_1) - Y_0}{d_y}\right] \tag{6.12b}$$

$$k(m) = \left[\frac{z_1 + \alpha_{mid}(z_2 - z_1) - Z_0}{d_z}\right] \tag{6.12c}$$

where α_{mid} can be calculated as

$$\alpha_{mid} = \left[\frac{\{\alpha\}(m) + \{\alpha\}(m-1)}{2}\right] \tag{6.13}$$

The RPL is finally calculated using equation (6.14), where ρ is the relative electron density of the voxel.

$$\mathbf{RPL} = \mathbf{d_{12}} \sum_{\mathbf{m=1}}^{\mathbf{m=n}} \rho[\mathbf{i(m)j(m)k(m)}](\{\alpha\}(\mathbf{m+1}) - \{\alpha\}(\mathbf{m})) \tag{6.14}$$

6.2.4 Dose calculation to a moving target

The field and MLC details are defined for zero degree gantry angle in machine coordinate system irrespective of the beam angle used in the DICOM RT plan whereas the RT structures are defined in patient coordinate system. The source position, segment and field shapes were first generated for the zero degree gantry angle in the patient coordinate system and then transformed using a 4x4 transformation matrix according to their respective gantry, collimator and couch angles (α, β, γ) as shown in equation 6.15.

$$\begin{vmatrix} x_t \\ y_t \\ z_t \\ 1 \end{vmatrix} = \begin{vmatrix} cos(\alpha) & -sin(\alpha) & 0 & 0 \\ sin(\alpha) & cos(\alpha) & 0 & 0 \\ 0 & 0 & 1 & 0 \\ 0 & 0 & 0 & 1 \end{vmatrix} \begin{vmatrix} cos(\beta) & 0 & sin(\beta) & 0 \\ 0 & 1 & 0 & 0 \\ -sin(\beta) & 0 & cos(\beta) & 0 \\ 0 & 0 & 0 & 1 \end{vmatrix} \begin{vmatrix} cos(\gamma) & -sin(\gamma) & 0 & 0 \\ sin(\gamma) & cos(\gamma) & 0 & 0 \\ 0 & 0 & 1 & 0 \\ 0 & 0 & 0 & 1 \end{vmatrix} \begin{vmatrix} x_0 \\ y_0 \\ z_0 \\ 1 \end{vmatrix} \tag{6.15}$$

Where $\{x_0, y_0, z_0\}$ and $\{x_t, y_t, z_t\}$ are points for zero degree gantry and transformed according to their corresponding collimator ,gantry, and couch angles (α, β and γ) respectively. Since all the beam objects like jaw, gantry, collimator, MLC rotates about the isocenter and not the image (CT) origin, a *translate-rotate-translate* approach, where all the beam objects are translated to the origin, rotated and translated back to the isocenter, is used for all transformations.The target structure of interest (CTV) is divided into voxels of 3x3x3 mm^3. Each MLC segment outline (ψ) is generated as mentioned before using the leaf position details in the DICOM RT plan. A sufficiently long ray is traced from the source position through each target voxel and a ray-segment intersection check is performed as depicted in figure 6.9. Depending on whether the ray is inside the segment or not and how close it is to the segment edge, the dose to the target voxel is calculated using equations 6.16-6.21. The distance between the segment edge and ray is calculated at the isocenter plane as shown in figure 6.10. A linear penumbra model is used for the dose calculation. The radiological path length is calculated using Siddon's raytracing algorithm [154] assuming uniform water equivalent density inside the patient.Dose-per-segment method is used, so that target voxels can be shifted for each segment to mimic organ motion and the calculated doses in individual voxels are summed for all segments and beams for all fractions. Since the starting phase of breathing for a particular fraction is unpredictable, a random phase-shift is applied to the organ motion calculation for each fraction in the interval $0 \leq \phi \leq 2\pi$. Figure 6.8 shows the variation of breathing traces due to nature of treatment startup at random phases.

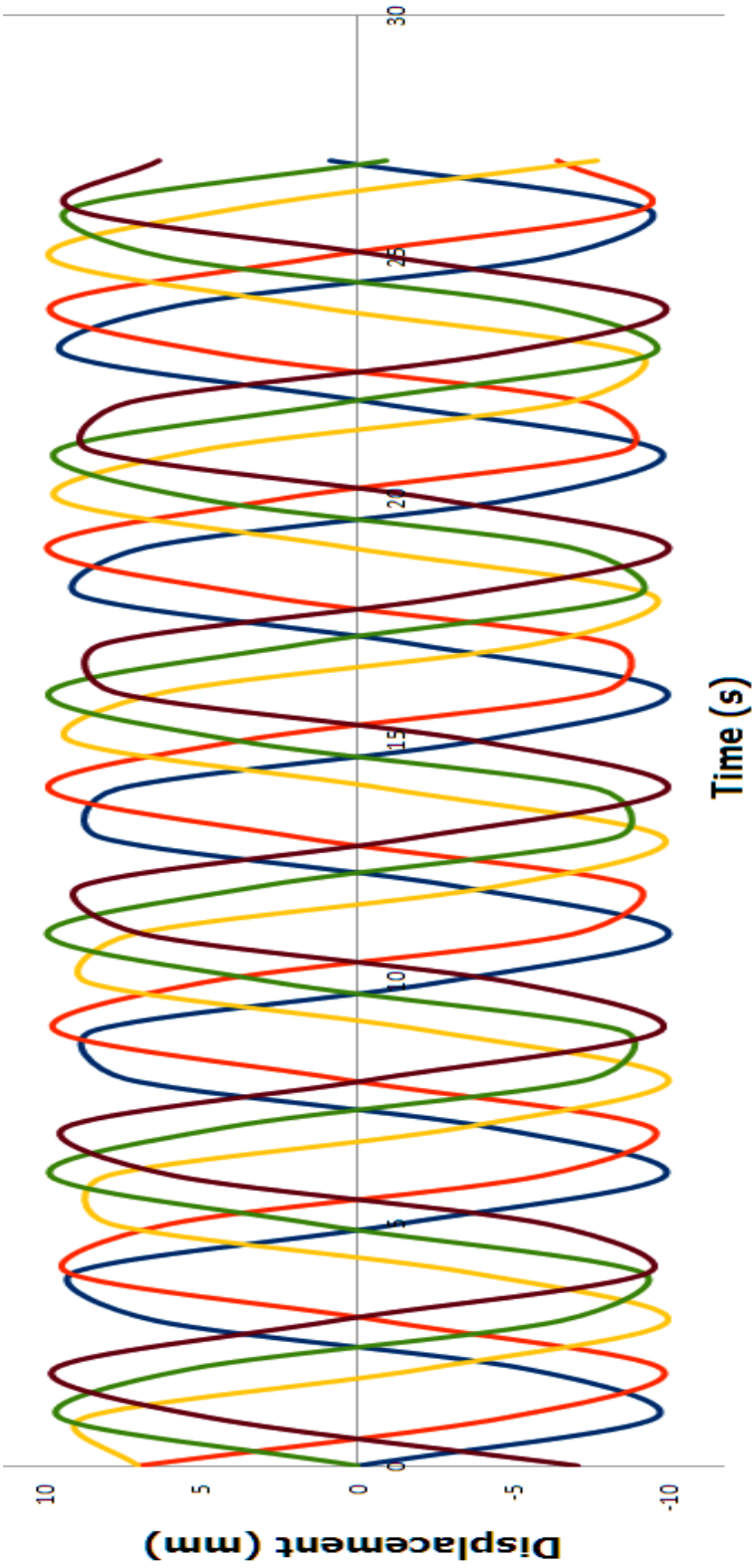

Figure 6.8: Random phase shift at different fractions

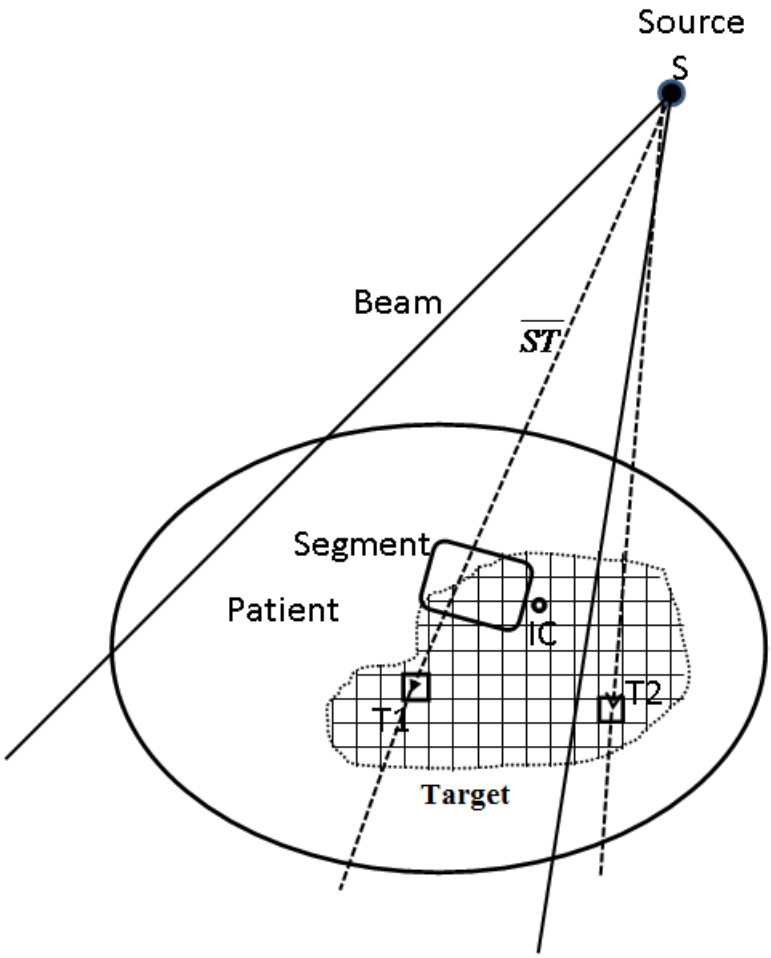

Figure 6.9: Ray-segment intersection, where ray $\overline{ST}$ contributes to voxel T_1 but not to T_2

$$D(x,y,z) = \sum_{f=1}^{f=n} \sum_{i=1}^{i=n_b} \sum_{j=1}^{j=n_s} MU_{i,j} F_{i,j} \tag{6.16}$$

where n_b and n_s are the number of beams and segments in beam i and n is the number of treatment fractions. $F_{i,j}$ is the dose correction factor for segment j in beam i. $F_{i,j}$ is calculated using equation 6.17 using the tissue-maximum ratios (TMR) values taken from BJR25 [92] for a 6 MV linac. Since scatter is ignored in our dose model the output factor is set to unity for all segments. the TMR values for corresponding field sizes at a water equivalent depth (wed) is used.

$$F_{i,j} = TMR(wed(x,y,z), ESF) * cf * SADfactor * pf \tag{6.17}$$

Where ESF is the equivalent field size calculated using equation 6.18, cf is the calibration factor of the linac (1 cGy/MU), pf is the penumbra factor.The SAD factor and the p_f are calculated according to equations 6.19 and 6.20 respectively.

$$ESF = \frac{2ab}{(a+b)} \tag{6.18}$$

$$SADfactor = \left(\frac{1000}{1000 - (d_{IC} - d)}\right)^2 \tag{6.19}$$

d_{IC} is the depth of isocenter and d is the water equivalent depth of voxel of interest in mm.

$$pf = \begin{cases} 1, & \text{if } \overline{ST} \in \psi \ \& \ \ d_{edge} \geq 5mm \\ pf_{in}, & \text{if } \overline{ST} \in \psi \ \& \ d_{edge} < 5mm \\ 0.016, & \text{if } \overline{ST} \ni \psi \ \& \ \ d_{edge} \geq 5mm \\ pf_{out}, & \text{if } \overline{ST} \ni \psi \ \& \ \ d_{edge} < 5mm \end{cases} \tag{6.20}$$

$$pf_{in} = 1.0 - ((5.0 - d_{edge})/10.0) \tag{6.21}$$

$$pf_{out} = 0.5 - (d_{edge}/10.0) \tag{6.22}$$

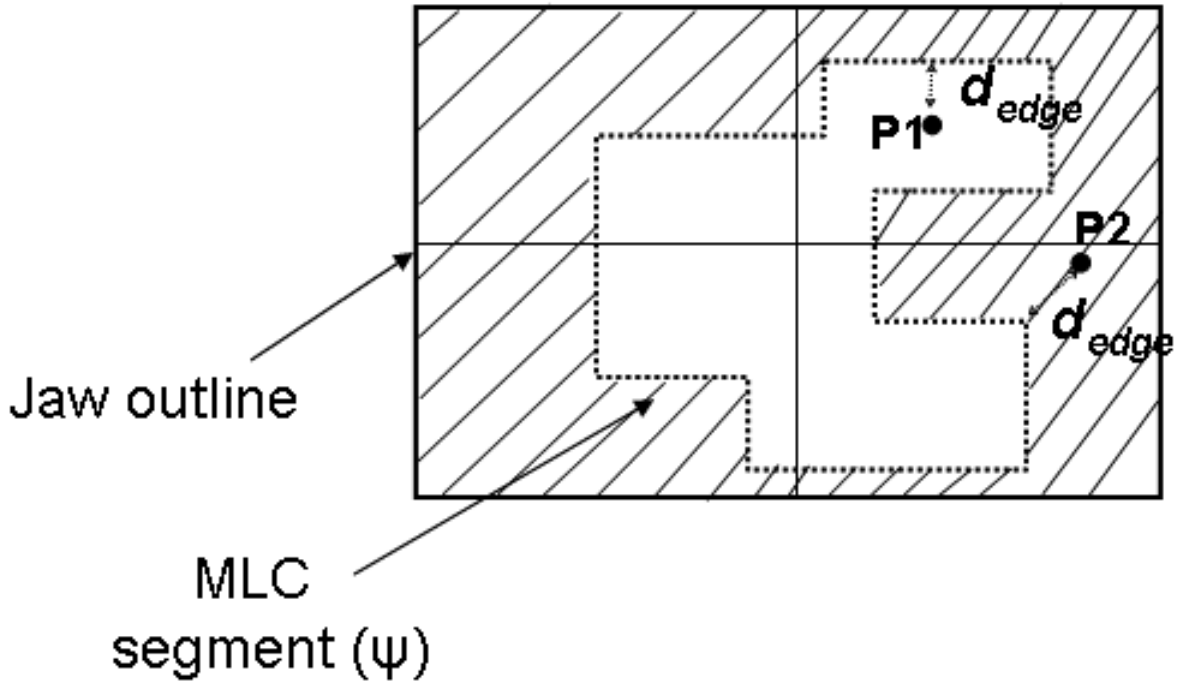

Figure 6.10: MLC outline at the isocenter level with points inside (P1) and outside (P2) the segment. d_{edge} is calculated from the closest edge of the segment to the ray

.

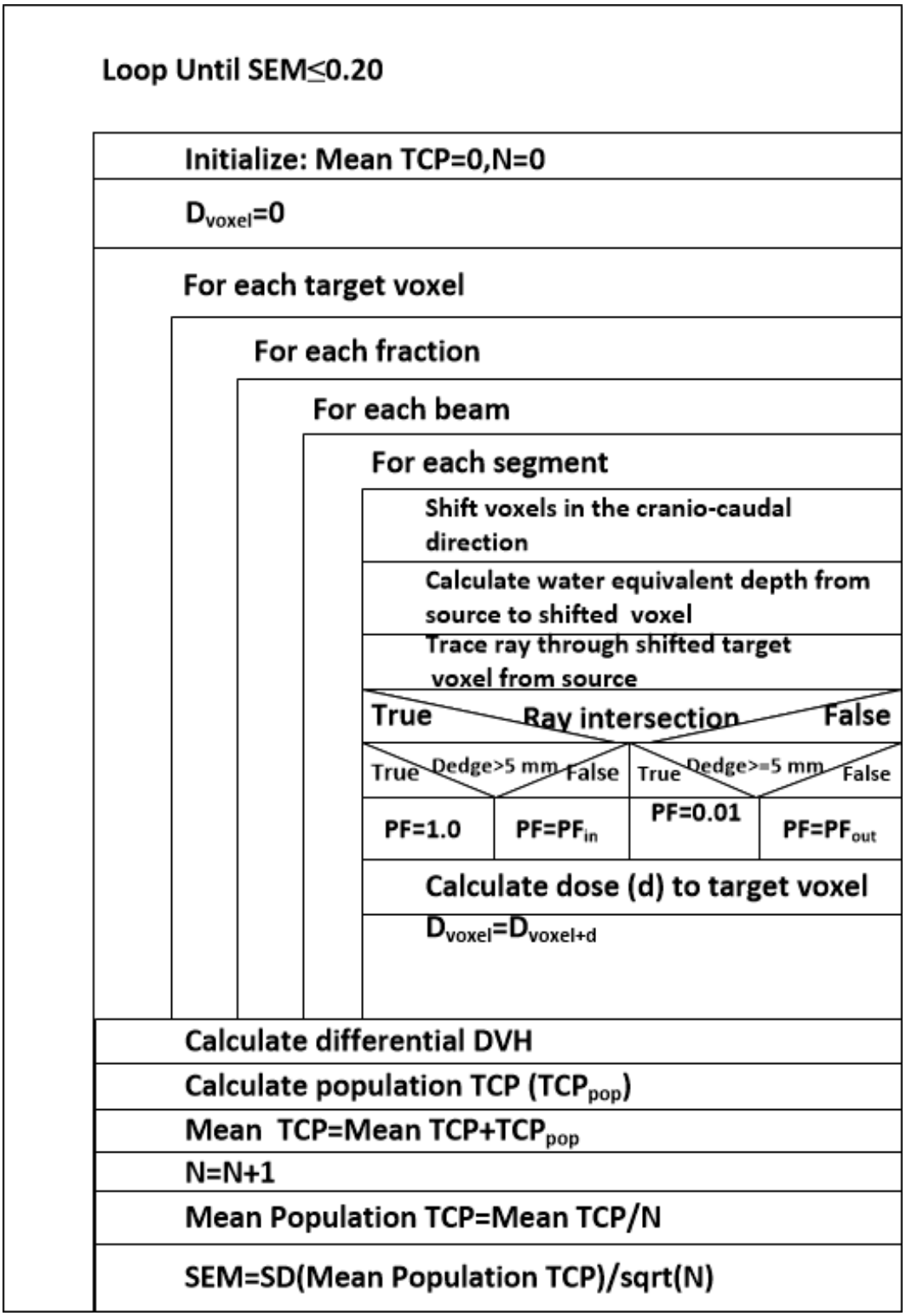

Figure 6.11: Nassi-Shneiderman diagram of the simualtion process

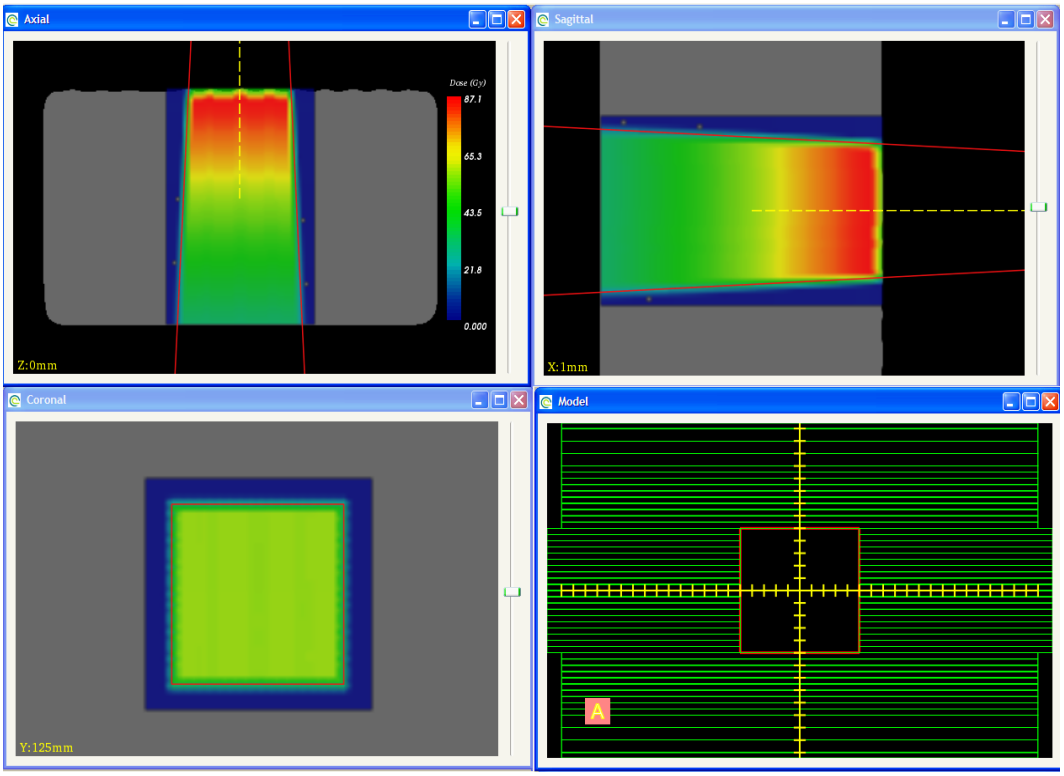

Figure 6.12: Dose color wash for a 5x5 cm^2 anterior field with MLC

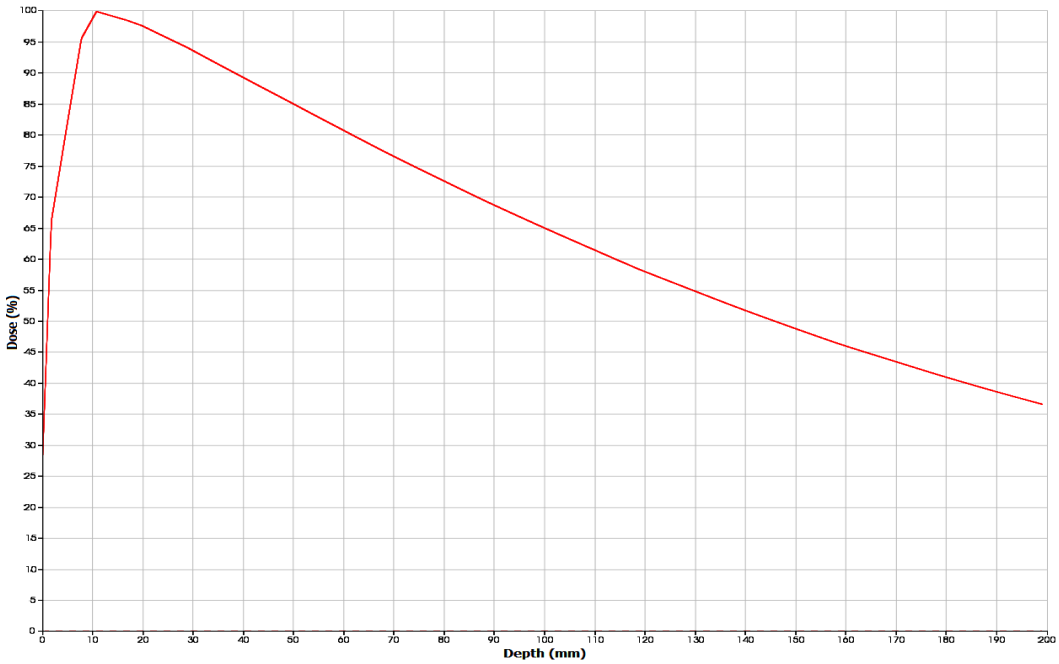

Figure 6.13: Percentage depth dose calculated in a water phantom for 10x10 cm^2 fieldsize

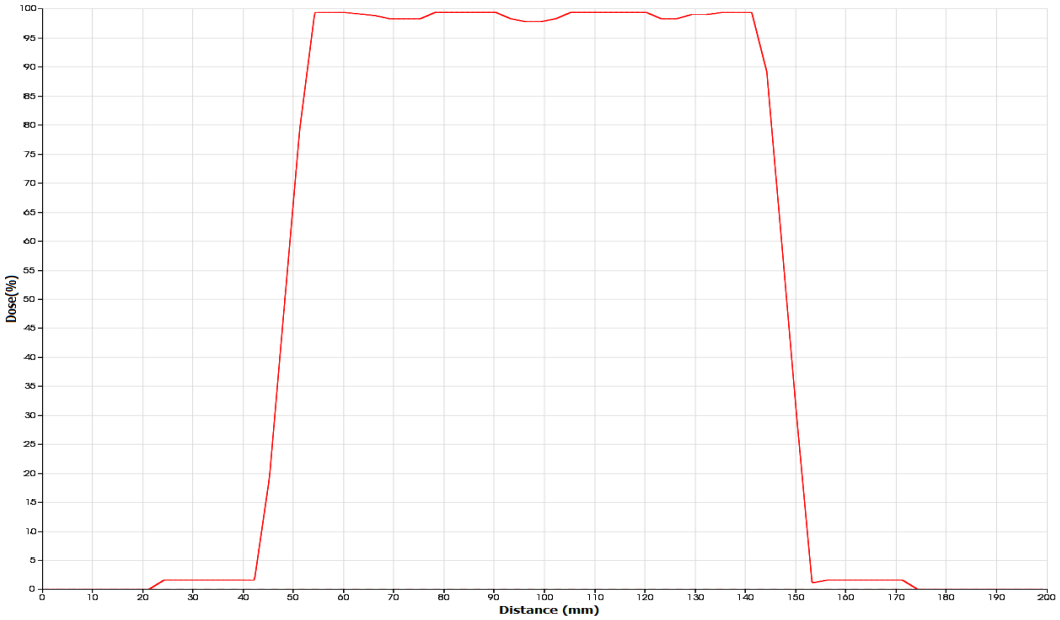

Figure 6.14: Cross profile calculated in a water phantom for 10x10 cm^2 fieldsize

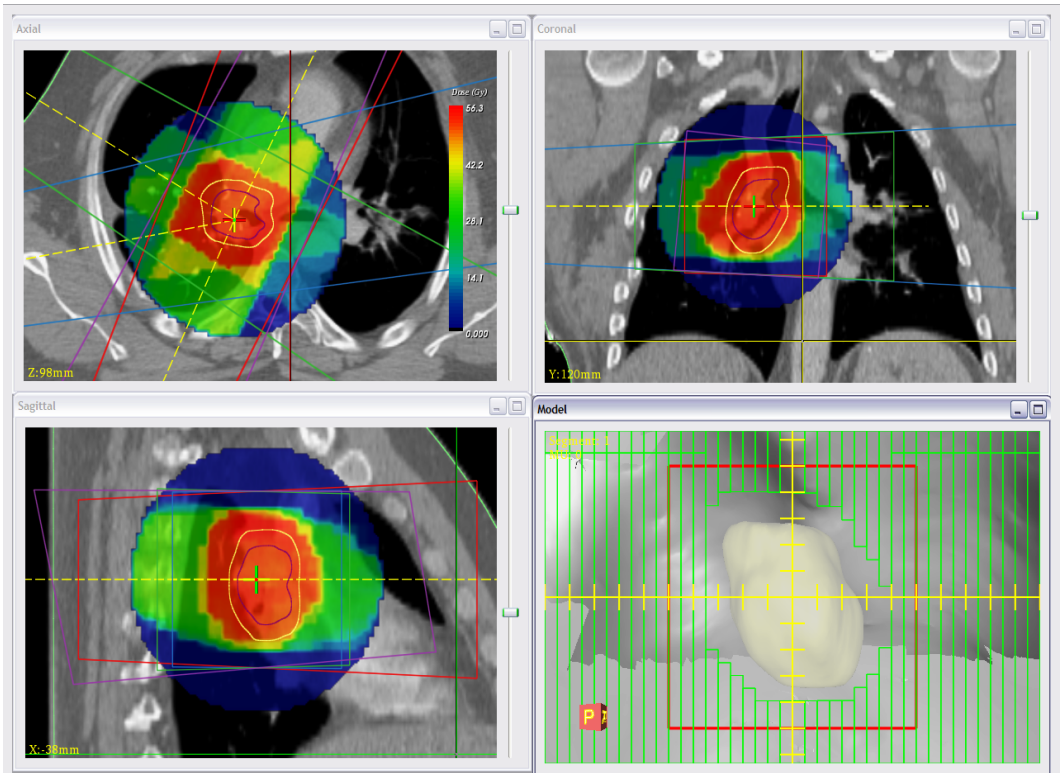

Figure 6.15: Dose distribution calculated with the simple beam model in a spherical VOI

The dose distribution calculated using the beam model in a spherical volume-of-interest is shown in figure 6.15 with imported structures and beams and the corresponding cumulative and differential DVH for CTV in figure 6.17.

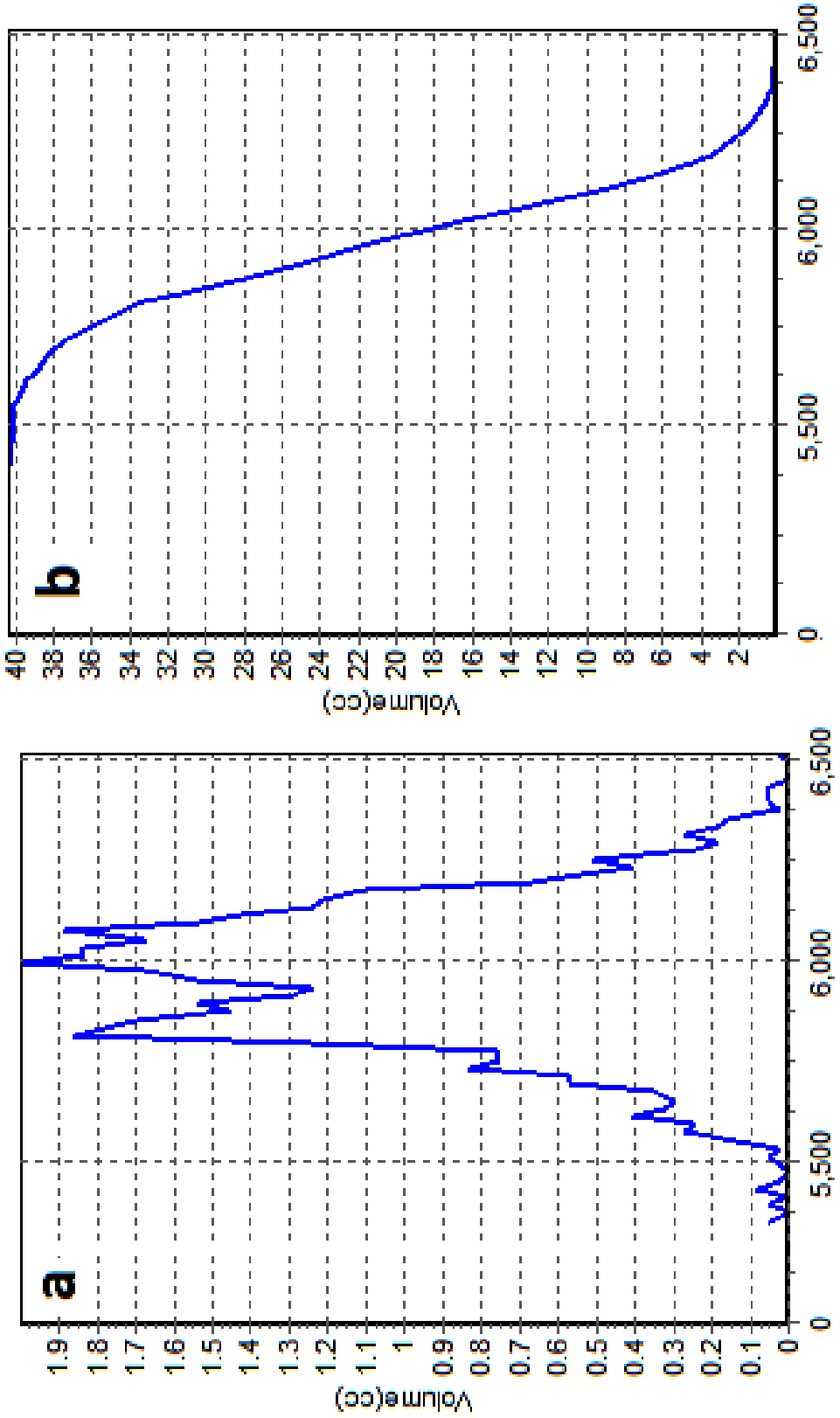

Figure 6.16: Cumulative and differential DVH calculated for static CTV using the simple beam model (please note the expanded scale in x-axis)

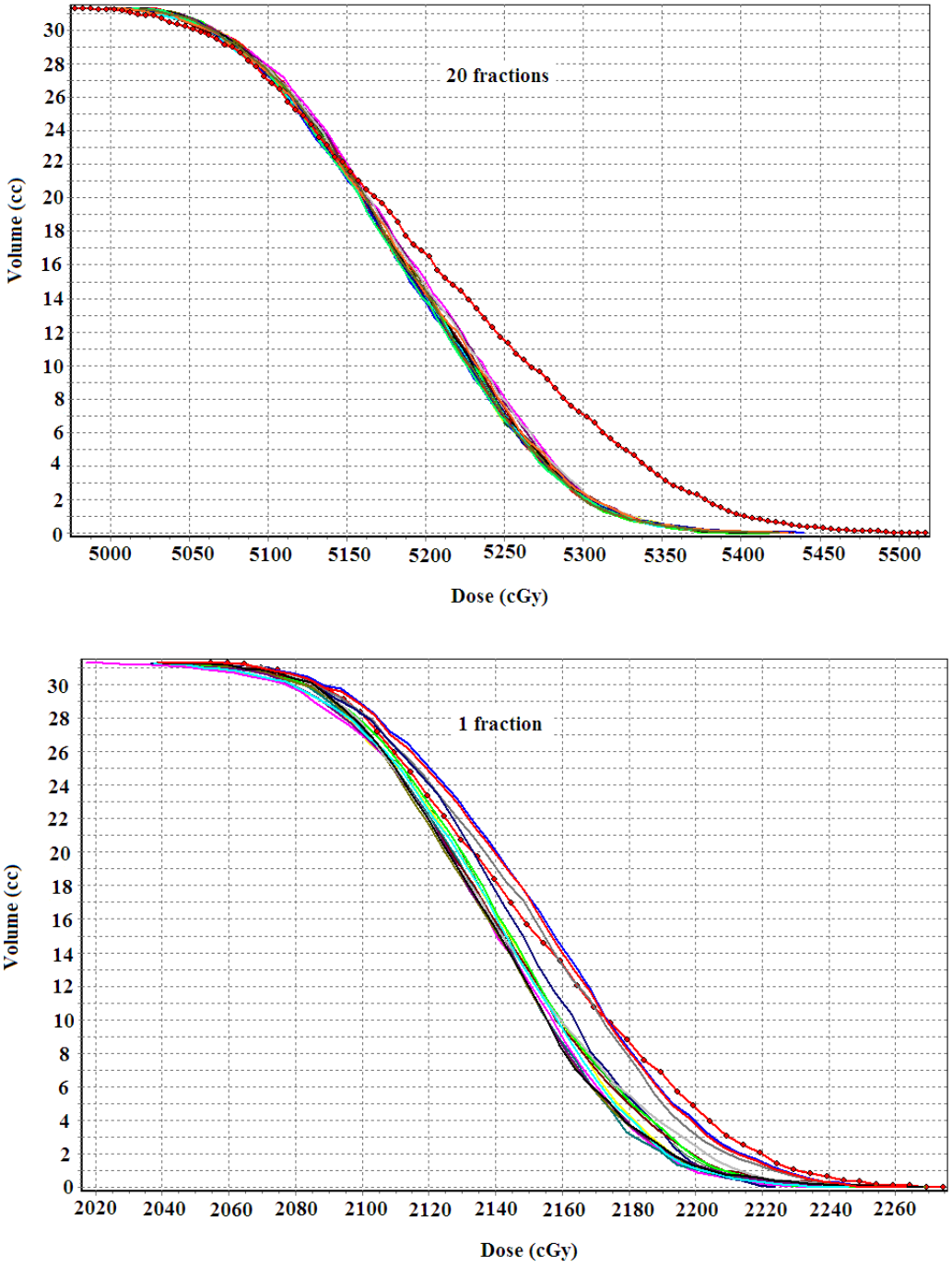

Figure 6.17: Representative cumulative DVHs for 20 fractions and 1 fraction with interplay effect and their corresponding static case (shown with marker) for a representative case.

6.2.5 Population TCP calculation

The population mean TCP ($\overline{TCP}_{pop}$) is calculated using the enhanced "Marsden" model [71] as shown in equation 6.23. σ_α value of 0.037 which corresponds to NSCLC is used [112]. $\overline{\alpha}$ value of 0.30 Gy^{-1} and a clonogen density (ρ_{cl}) is set to 1E7 cells/cc. The number of simulations were repeated until the standard error is ≤ 0.20.

$$\overline{TCP}_{pop} = \frac{1}{n}\sum_{1}^{n} TCP \tag{6.23}$$

where n is the number of simulations.

6.3 Results and discussion

The TCP values for 20 and three fraction treatments are calculated based on the final accumulated dose (D_{voxel}) in each individual voxels over the course of treatment. This assumes that each voxel receives a dose of D_{voxel}/n each fraction, which is an approximation. In fact the dose to each voxel for each fraction in the presence of the interplay effect will be different from the mean D_{voxel}/n [155]. Thus the biological effect of non-uniform dose is also a concern in interplay effect where some voxels receive very less dose while some other voxels receive a very high dose in a particular fraction. However, for a fractionated treatment Bortfeld *et al* [38] have shown that the radiobiological differences are negligible for tissues with high α/β ratio and the differences are large only for tissues with lesser α/β ratio. Since tumours have a high α/β ratio(10 Gy) and the treatments are fractionated, the effect of non-uniform dose to voxels on TCP should be negligible. This concern disappears for single fraction treatments.

The spatial variation of dose (accumulated dose) due to interplay effect is shown in figure 6.18 for one plan used in the study. For comparison, the dose for the single fraction plan is set equal to the 20 fraction plan (i.e., the dose that produces 50% TCP in the 20- fraction plan). In this case a significant underdosage can be observed for the single fraction plan but this just for one treatment and could be opposite for other treatments.

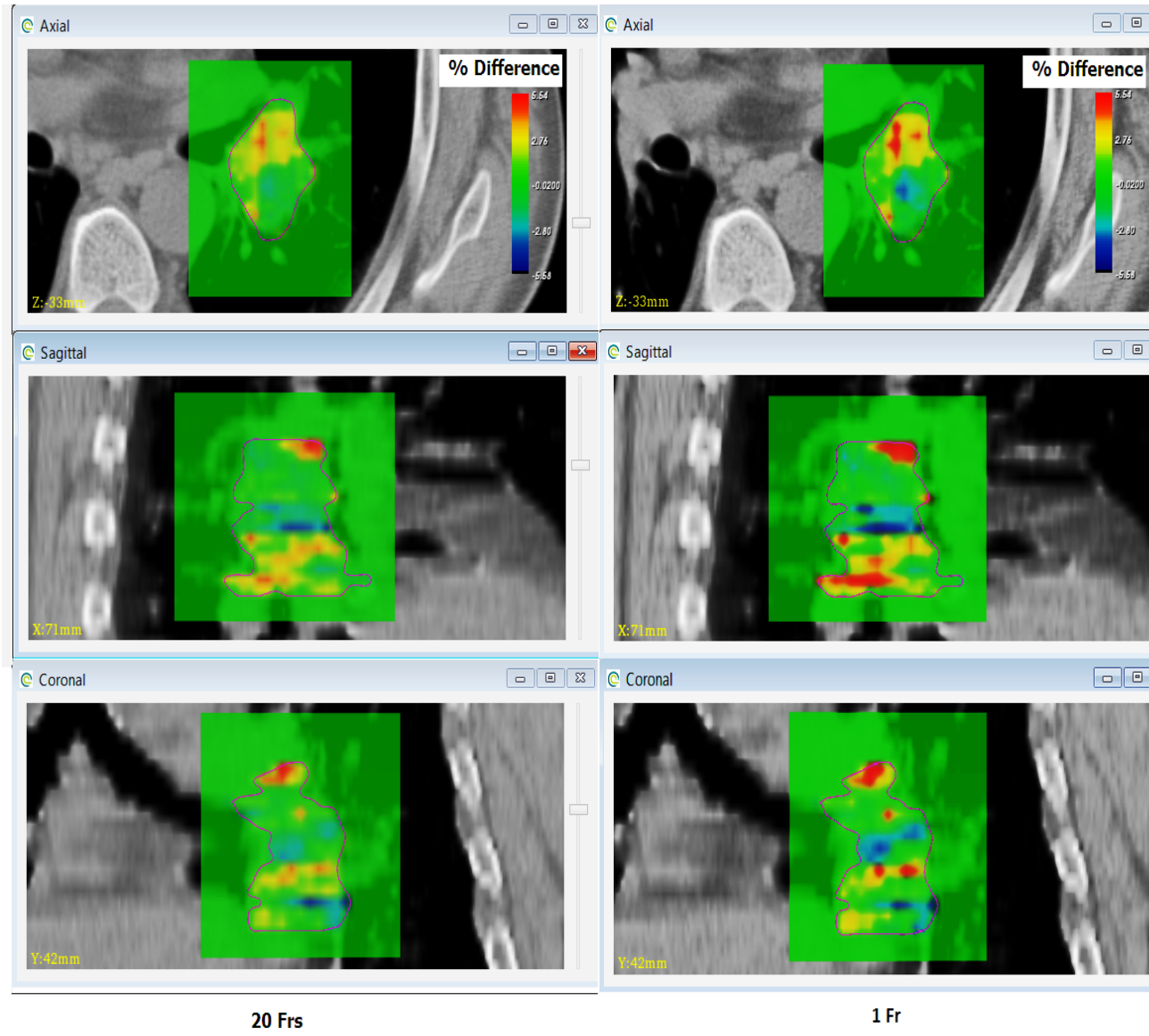

Figure 6.18: Axial, sagittal and coronal dose difference comparison on isocentre plane for 20-fraction and 1-fraction treatment with the static case. Blue represent no change in the dose and darker red represents greater difference with the static case.

The percentage variation in population minimum ($\%\bar{D}_{min}$), maximum($\%\bar{D}_{max}$) and mean($\%\bar{D}_{mean}$) dose relative to the static tumour are shown in figure 6.19. The mean values $\%\bar{D}_{min}$, $\%\bar{D}_{max}$, $\%\bar{D}_{mean}$ are calculated from the mean of the individual plan values. These values are given in table 6.3 along with their standard deviations. The population mean of $\%\bar{D}_{min}$, $\%\bar{D}_{max}$ and $\%\bar{D}_{mean}$ are $< 1\%$ for the 20 and three fractions treatments but larger for the single fraction treatments. However, the standard deviation of the three fraction treatment is considerably more than 20 fractions treatment, which indicates that individual patients will experience larger variations in dose values for a three fractions treatment compared to 20 fractions treatment. The standard deviations for the single fraction treatments are even higher than that of three and 20 fractions treatment. This very well corroborates the finding of Seco *et al* [151],

who showed that reduced dose errors in many-fraction treatment will not work for hypo-fractionated treatments. Although the effect of interplay on dose variations for conventionally and hypofractionated treatments provides some understanding on the nature of interplay effect, it is more useful to know the clinical significance of these dose variations. Obviously for tumours, TCP will be a more meaningful indicator of clinical outcome. The variation in TCP due to these dose variations caused by interplay effect is shown in figure 6.21.

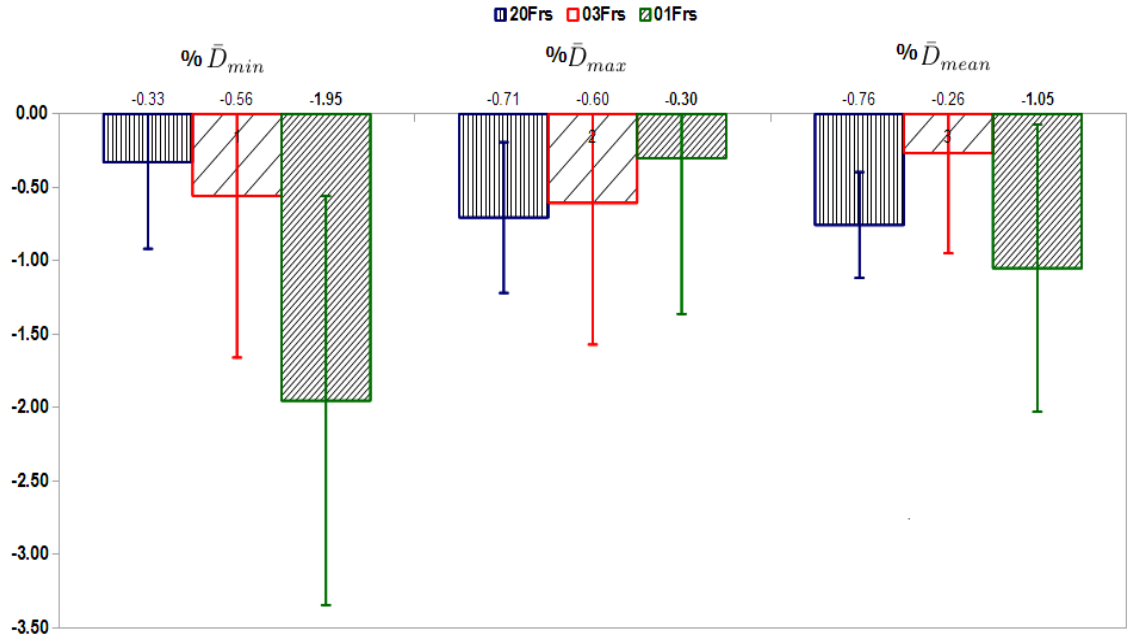

Figure 6.19: % change in population minimum, maximum and mean dose for 20, 3 and 1 fraction treatments. The values shown are average (obtained through several runs of simulation for each plan) change in dose values. The error bars represent mean standard deviation obtained from individual standard deviations $\left(\sqrt{(\frac{\sigma_1^2+...+\sigma_n^2}{n}}\right)$.

Table 6.3: Percentage variation in population $\%\bar{D}_{min}$, $\%\bar{D}_{max}$ and $\%\bar{D}_{mean}$ dose relative to the static tumour with standard deviations for different fractions.

Fractions	$\%\bar{D}_{min}$	$\%\bar{D}_{max}$	$\%\bar{D}_{mean}$
20	-0.33±0.59	-0.71±0.51	-0.76±0.36
03	-0.56±1.10	-0.96±0.97	-0.26±0.68
01	-1.95±1.39	-0.30±1.06	-1.05±0.98

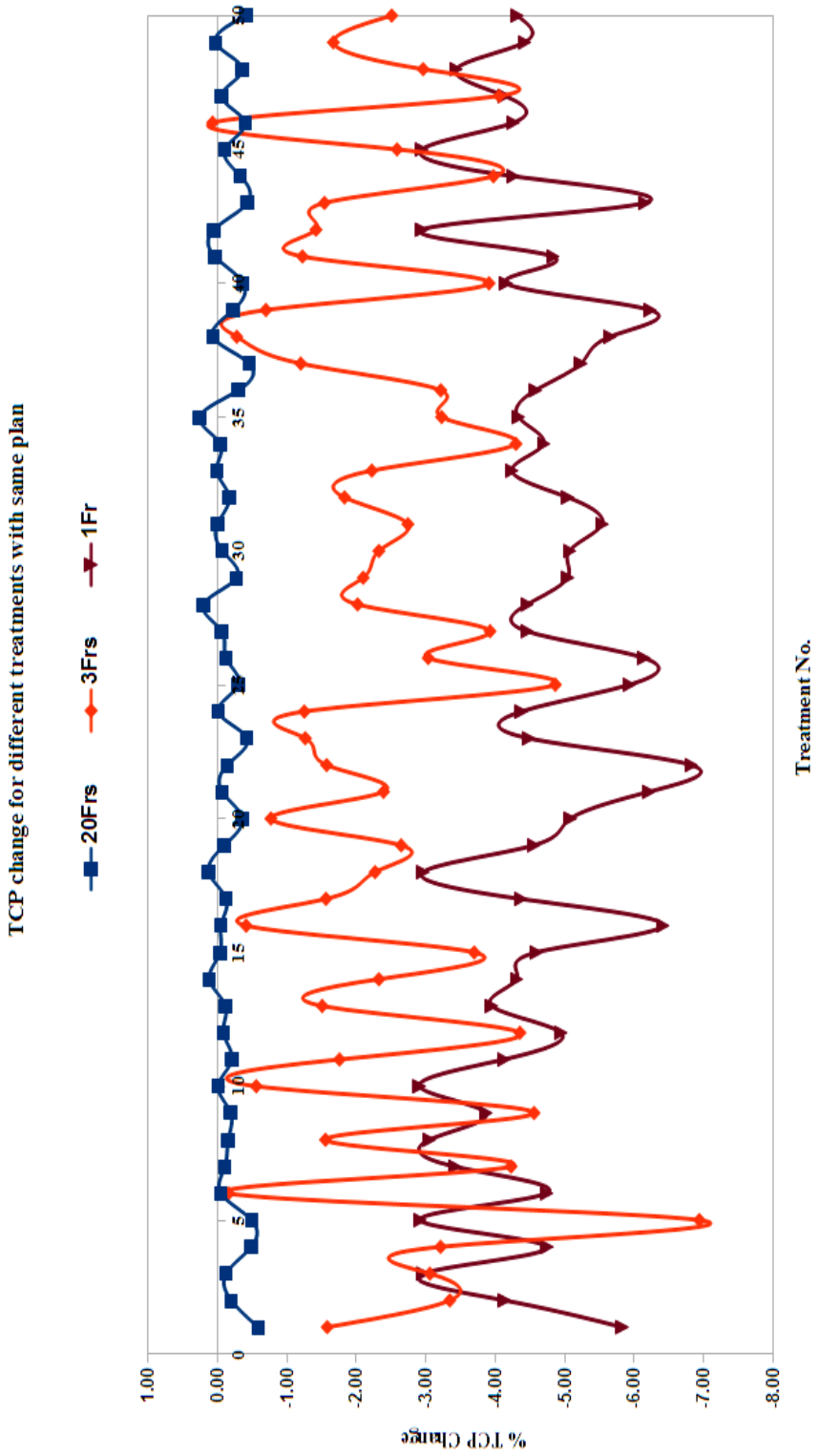

Figure 6.20: % TCP change compared to static tumour for 20, 3 and 1 fraction treatments.

As shown in figure 6.20, the variation in TCP for 20 fractions treatment with interplay effect is almost equal to the TCP value for the static tumour. This shows that for treatments with large number of fractions, the dose errors will be small and thus

the effect of interplay on TCP is negligible. This is mainly due to the underdosing and overdosing of same voxels in different fractions (with many fractions) which lead to the convergence of voxel doses similar to the static case. The degree of variation in dose and TCP between patients for a given fractionation differs strongly as reported by Rao *et al* [156], which indicates that the effect of interplay is dependent on the shape of the tumour as tumours which are larger in the cranio caudal axis will experience greater impact of interplay. In addition to that the fluence pattern is unique for each beam and the gradient of the fluence will have a strong impact on the interplay, with the effect of interplay increasing with the gradient of the beam fluence. But a large variation can be observed for 3 and single fractions, mostly in the negative direction. It is interesting to note that few patients could gain from the interplay effect as a result of a majority of the voxels being overdosed, thus also increasing the TCP. However, it is impossible to find out this small percentage of patients who would benefit from interplay effect in reality. Though the TCP loss is unacceptably high for single and 3 fraction treatments, it's within acceptable limit ($\sim$1%) for the 20 fractions treatment. The mean of the population average TCP values calculated for each patient ($\overline{TCP}_{pop}$) provides a general idea on how the interplay affects $\overline{TCP}_{pop}$. The $\overline{TCP}_{pop}$ is shown in figure 6.21 for six plans for different fractionations along with the mean of all plans. As with the standard deviation of the dose values, the standard deviation of the $\overline{TCP}_{pop}$ are also significantly different from the static case for the hypofractionated and single-fraction treatments. This indicates that individual patient TCP values will experience large variations in hypofractionated treatments compared to the static tumour. This can be observed from figure 6.21 that in conventional fractionation the effect of interplay on $\overline{TCP}_{pop}$ is very marginal or within acceptable limit ($-1.05 \pm 0.39\%$), but for hypofractionated and single fraction treatments such as radiosurgeries it is considerably high, namely $-2.82 \pm 1.68\%$ and $-3.95 \pm 2.84\%$ respectively. This clearly indicates that motion management methods are inevitable for hypofractionated treatments to avoid significant loss in population TCP (though a small percentage of patients would benefit from interplay effect) for IMRT of lung treatments. In contrast to our findings, Ong *et al* [157] found that for single fraction RapidArc treatments the difference in dose to the tumour is not significantly higher. However, these findings were based on 2D dose measurements with films in the coronal plane which will not provide a complete picture of the effect of dose to the tumour including interplay. While hypofractionated treatments are subject to a lot of variability in the dose delivered to a moving tumour, their increased delivery time (due to higher dose per fraction) makes the dose delivered over many breathing cycles. Delivery of dose by each segment over multiple breathing cycles would cancel out the dose differences which takes place across multiple fractions for conventional treatments. This effect can reduce the dose errors up to some extent in hypofractionated and single-fraction treatments where higher doses are delivered per fraction.

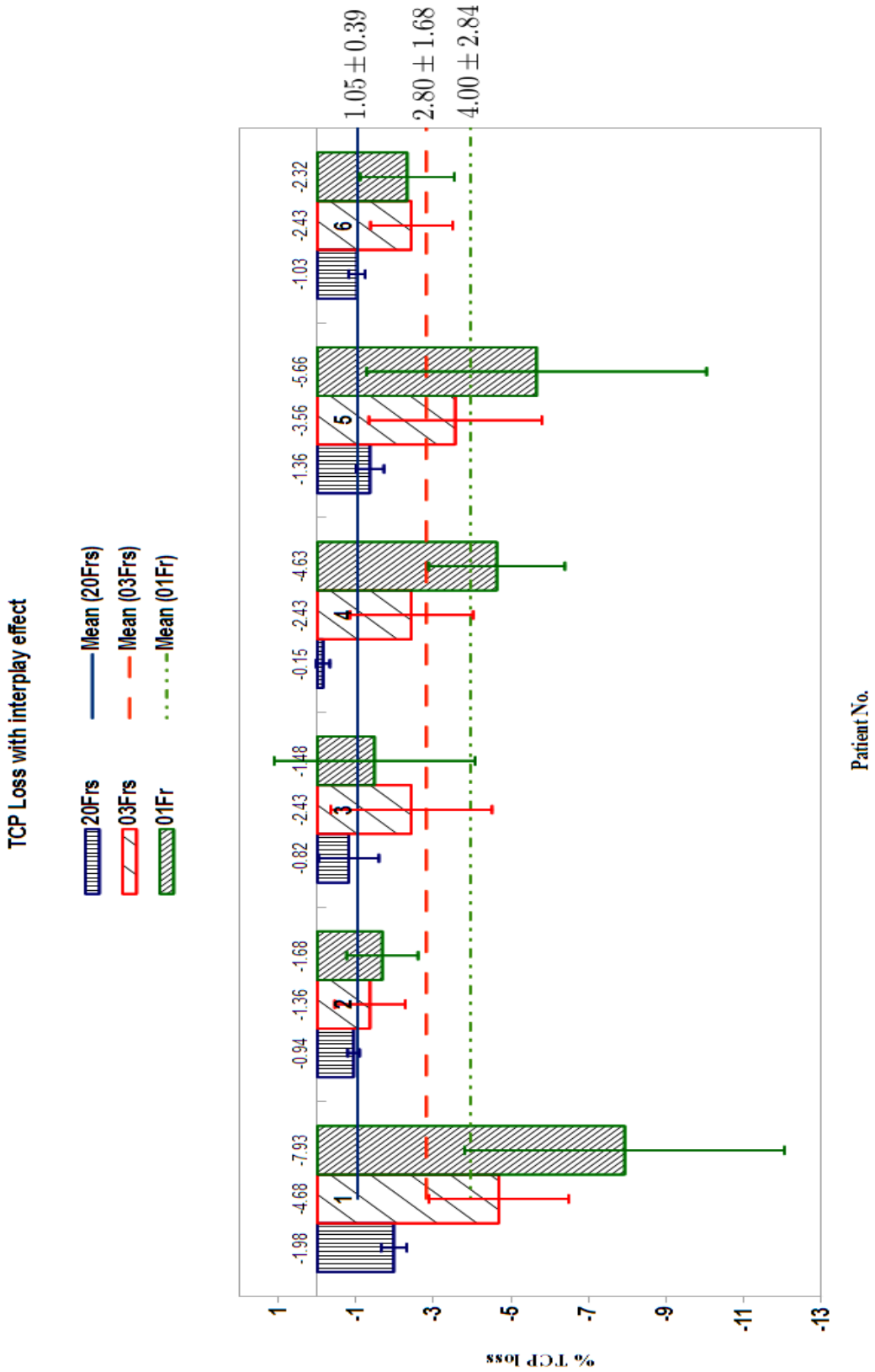

Figure 6.21: % TCP change for 20,3 and 1 fraction treatments with standard deviation.

The effect of dose rate on TCP due to interplay is studied for single fraction treatments with 300 and 600 MU/min. The results are shown in shown in figure 6.22. From

the figure, it is evident that dose delivery over multiple breathing cycles by reducing the dose rate would reduce the interplay effect. On an average the TCP reduction due to interplay effect was reduced $\sim$ 1.5% with 300 MU/min compared to 600 MU/min. This indicates that reduced dose rate is beneficial for treating moving targets while no motion management techniques are used. A similar finding has been reported by Court *et al* [158] using a 2D ion chamber matrix for various dose rates in dynamic IMRT plans.

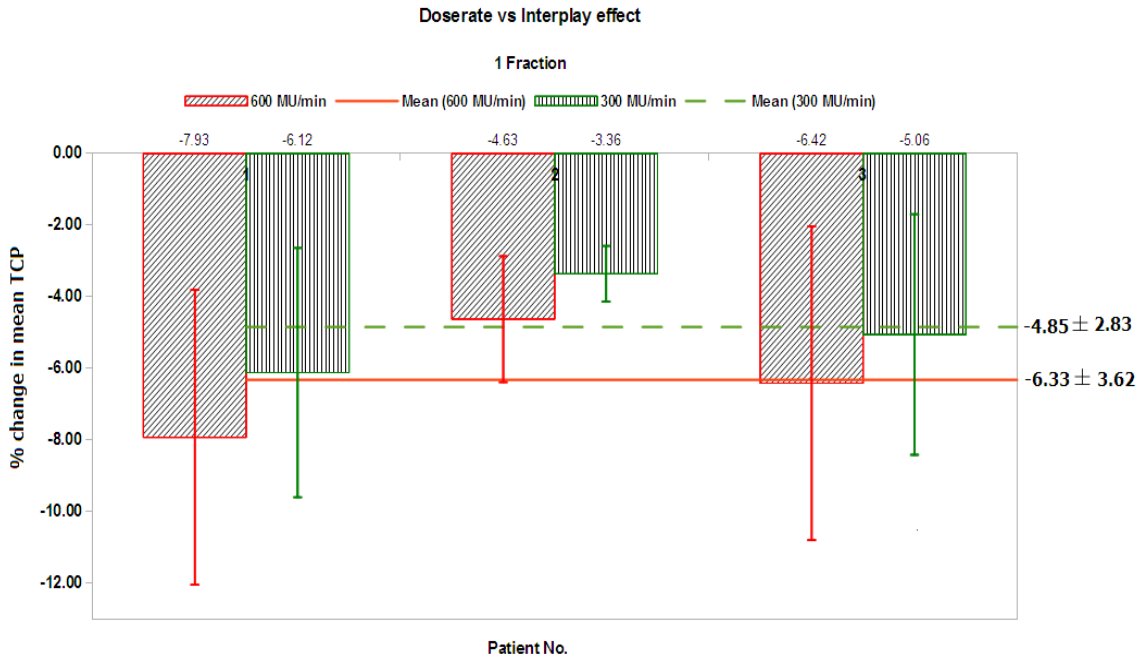

Figure 6.22: Effect of dose rate on interplay for a single fraction treatment with standard deviation.

As in other studies there are several assumptions made in this study.It should be noted that real patient's breathing is very different from the sinusoidal assumption. In fact the breathing may continuously change amplitude and period making it is difficult to model mathematically [159]. Another important point is that the lung tumour is surrounded by a tissue of lower density and the density of this spongy tissue may vary continuously during breathing which could have significant effect on the dose delivered to the tumour. Further, the inhomogeneity and scatter corrections are ignored in this study, which would actually influence the results slightly but the trend of the results should remain same. As mentioned by Duan et al [42] the random positioning errors during each fraction (isocenter offset, which would give actual position of segment relative to the tumour position) should be accounted in order to study the exact dose delivered to the tumour inclusive of interplay effect.

Though the dose model presented in this work does not account for scatter and inhomogeneity, the methodology presented here to simulate the interplay effect can be

easily extended to account for scatter and tissue inhomogeneity. Moreover systematic and random errors can be incorporated into the simulation as the final displacement of target voxels will be the sum of the three vectors namely, systematic, random and cranio-caudal shifts. This model can also be used for dynamic treatments as well. The simulation time to obtain the $\overline{TCP}_{pop}$ with a reasonable standard error can be greatly reduced by calculating the dose for some fractions ($\sim$ 50) individually with random phase-shifts and add them randomly (by randomly choosing the required number of fractions from the 50 fractions) to get the final accumulative dose for n fractions.

Chapter 7

Conclusions

Margins based on TCP is found to be lesser than dose-based recipes except for hypofractionated treatments and tumours with steep dose-response curve. The margins are also found to be dependent on dose-response curve and number of treatment fractions. For the hypofractionated treatments, the effect of random errors too become as detrimental as systematic errors as the assumption of dose blurring of random errors is not valid for treatments with fewer fractions. The margins required based on TCP loss is studied for spherical and four field dose distribution. For the four field treatment with small geometric uncertainties ($\Sigma, \sigma = 1$ mm) and large number of treatment fractions the margins are close to zero, but this assumes the CTV is accurately defined. Comparison of the results with the widely used van Herk recipe *et al* [52] revealed that dose-based recipes overestimate the margins for tumours with shallow dose-response curve and underestimates for tumours with steep dose-response curve and hypofractionated treatments. The dose conformity was also found to have a strong influence on choice of margins irrespective of tumour radiobiological characteristics.

The Monte Carlo method to simulate geometric uncertainties presented in this thesis and the software framework developed can simulate the effect of geometric uncertainties for a given plan with additional parameters such as number of fractions, tumour radiobiological characteristics and estimates of systematic and random errors. Implementation of such a method into treatment planning systems would be a great tool to determine the margin sufficiency for a given plan with the dose distribution and the radiobiological characteristics for the tumour of interest. Although the TCP based margins are found to be smaller than dose based recipes, careful attention should be paid to the biological uncertainties in the target volume such as the microscopic disease extension, where they are present, what density it is of. The margin determination in this thesis assumes that the microscopic disease is well contained with in the CTV. In case the extent of CTV is not accurately known then the margin reduction would increase the risk of local failure. However, if the knowledge of microscopic disease is known from microscopic analysis of surgical specimen, reduced margins could be used

which will greatly improve the therapeutic ratio.

Knowledge of microscopic disease is poorly known and is one of the major limiting factor in harnessing the full potential of IGRT. It is also shown in chapter 4 that patients with tiny tumour islets present around the tumour (which can only be detected by microscopic analysis) does not benefit from dose escalation. The impact of these microscopic disease on various treatment techniques such as VMAT, Cyberknife, Tomotherapy and protons is not clearly known. Hence, employing smaller margins is always associated with an increased risk of missing the tumour. Clinical trials are needed to validate the influence of these factors on tumour control. Margin determination should be evidence based rather than just technology driven as all the uncertainties in radiotherapy is not know.

Respiration induced tumour motion and the interplay between MLC movement is found to have negligible impact on TCP for conventionally fractionated treatments. However, it found to have substantial impact on hypofractionated and single fraction treatments such as streotactic ablative radiotherapy and streotactic radiosurgery. Hence motion management techniques such as tumour tracking or gating should be used to maintain TCP loss within acceptable limits. The impact of dose rate is also studied for two different dose rates namely 300 and 600 MU/min for hypofractionated treatments and using a lower dose rate is found to mitigate the effects of interplay. Hence, when no motion management techniques are used a reduced dose rate can be used to minimize the impact of interplay. One of the major limitations of the dose model presented in this thesis is that it does not account for scatter and tissue heterogeneity which are dominant in lung radiotherapy. However the results are compared to the dose distribution of the static tumour computed from the same dose model and hence the differences should be minimal. But the dose model is flexible to account for these effects and the patient's real breathing can be used instead of a sinusoidal wave form.

7.1 Future work

Margin determination studied in this thesis assumes either highly conformal symmetrical or a four field dose distribution, which are far from real dose distributions achieved in the clinic. Margins are also found to be very much dependent on dose conformity and the beam orientations. It would be very useful to determine margins for a given planing protocol including beam orientations, dose conformity, tumour radiobiological characteristics with the known systematic and random errors for the given treatment using the Monte Carlo method presented in this thesis. This can be achieved by generating plans with different margins and to find the TCP loss for each plan. By doing this for different geometric uncertainties and tumour types for each technique would enable us to generate a lookup table of PTV margins.

The impact of microscopic disease on tumour control is complicated and less studied as mentioned before. As we move towards higher and higher conformal treatments, the importance of accurate target volume definition increases. If the target definition is not accurate the benefit of these sophisticated and highly expensive treatments are of not much use. The effect of microscopic disease in this thesis is studied only in the phantom geometry assuming an exponential clonogen distribution and randomly distributing the tiny tumour islets outside the CTV. In reality, dose distribution resulting from treatment plans depend on numerous factors such as treatment technique, dose constraints, delivery method (fixed or rotational). Hence the amount and distribution of the incidental dose is different for different techniques. The effect of microscopic disease on different techniques has not been reported and poorly understood. One reason for lack of such studies is that it requires precise knowledge of the clonogen distribution or the number of islets and their location, which can be obtained only through extensive microscopic analysis of surgical specimens. Nevertheless, assuming an exponential clonogen distribution and using the dicom datasets of few patients treated by various treatments such as static field IMRT, VMAT, Cyberknife and proton therapies with the dose distribution obtained from treatment planing systems would shed light on the importance of accurate CTV delineation in image guided conformal radiotherapy.

The interplay dose model presented assumes several simplifications in order to speed up the calculation time. It also assumes a sinusoidal breathing pattern although the real breathing pattern is slightly different and also varies from patient o patient. It is possible to obtain the breathing pattern of an individual patient either using a respiratory position management system (RPM) or a 4D CT. The model also doesn't account for dose scatter or heterogeneities. However the model presented in this thesis is flexible enough to account for these. Methods used in IMRT dose verification algorithms can be used to account for scatter and tissue heterogeneities with slight modification of the current dose model hence it is also based on ray tracing. Moreover, the patient's breathing pattern with the actual amplitude and frequency can be used instead of a sinusoidal pattern. These modifications will greatly improve the accuracy of the dose model to quantify the effect of interplay on dose distribution and TCP. The dose model can also be extended to rotational delivery techniques such as VMAT/RapidArc.

Bibliography

[1] ICRU Report 50. Prescribing, recording, and reporting photon beam therapy. Technical report, International Commission on Radiation Units and Measurements,Bethesda, MD., 1993.

[2] ICRU Report 62. Prescribing, recording, and reporting photon beam therapy (supplement to icru report 50). Technical report, International Commission on Radiation Units and Measurements,Bethesda, MD., 1999.

[3] MM Urie, M Goitein, and K Doppke et al. The role of uncertainty analysis in treatment planning. *Int J Radiat Oncol Biol Phys*, 21:91–107, 1991.

[4] JM Links, LS Beach, and B Subramaniam et al. Edge complexity and partial volume effects. *J Comput Assist Tomogr*, 22:450–458, 1998.

[5] DF Dubois, BR Prestidge, LA Hotchkiss, JJ Prete, and WS Bice. Intraobserver and interobserver variability of mr imaging-and ct-derived prostate volumes after transperineal interstitial permanent prostate brachytherapy. *Radiology*, 207(3):785–789, 1998.

[6] C Fiorino, M Reni, A Bolognesi, GM Cattaneo, R Calandrino, et al. Intra-and inter-observer variability in contouring prostate and seminal vesicles: implications for conformal treatment planning. *Radiotherapy and oncology: journal of the European Society for Therapeutic Radiology and Oncology*, 47(3):285, 1998.

[7] RK Ten Haken, AF Thornton, HM Sandler, ML LaVigne, DJ Quint, BA Fraass, ML Kessler, and DL McShan. A quantitative assessment of the addition of mri to ct-based, 3-d treatment planning of brain tumors. *Radiotherapy and Oncology*, 25(2):121–133, 1992.

[8] G Leunens, J Menten, C Weltens, J Verstraete, and E Van der Schueren. Quality assessment of medical decision making in radiation oncology: variability in target volume delineation for brain tumours. *Radiotherapy and Oncology*, 29(2):169–175, 1993.

[9] C Weltens, J Menten, M Feron, E Bellon, P Demaerel, F Maes, W Van den Bogaert, E van der Schueren, et al. Interobserver variations in gross tumor volume

delineation of brain tumors on computed tomography and impact of magnetic resonance imaging. *Radiotherapy and oncology*, 60(1):49, 2001.

[10] C Rasch, I Barillot, P Remeijer, A Touw, M van Herk, JV Lebesque, et al. Definition of the prostate in ct and mri: a multi-observer study. *International Journal of Radiation Oncology Biology Physics*, 43(1):57, 1999.

[11] JG Armstrong, MJ Zelefsky, SA Leibel, C Burman, C Han, LB Harrison, GJ Kutcher, and ZY Fuks. Strategy for dose escalation using 3-dimensional conformal radiation therapy for lung cancer. *Annals of Oncology*, 6(7):693–697, 1995.

[12] LS Broderick, RD Tarver, and DJ Conces. Imaging of lung cancer: old and new. In *Seminars in oncology*, volume 24, page 411, 1997.

[13] JG Armstrong. Target volume definition for three-dimensional conformal radiation therapy of lung cancer. *British Journal of Radiology*, 71(846):587–594, 1998.

[14] P Giraud, M Antoine, A Larrouy, B Milleron, P Callard, Y De Rycke, MF Carette, JC Rosenwald, JM Cosset, M Housset, et al. Evaluation of microscopic tumor extension in non–small-cell lung cancer for three-dimensional conformal radiotherapy planning. *International Journal of Radiation Oncology Biology Physics*, 48(4):1015–1024, 2000.

[15] A. Diaz, M. Roach, C. Marquez, L. Coleman, B. Pickett, J.S. Wolfe, P. Carroll, and P. Narayan. Indications for and the significance of seminal vesicle irradiation during 3d conformal radiotherapy for localized prostate cancer. *International Journal of Radiation Oncology* Biology* Physics*, 30(2):323–329, 1994.

[16] L Ekberg, O Holmberg, L Wittgren, G Bjelkengren, and T Landberg. What margins should be added to the clinical target volume in radiotherapy treatment planning for lung cancer? *Radiotherapy and oncology*, 48(1):71–77, 1998.

[17] A Tinger, JM Michalski, A Cheng, DA Low, R Zhu, WR Bosch, JA Purdy, CA Perez, et al. A critical evaluation of the planning target volume for 3-d conformal radiotherapy of prostate cancer. *International journal of radiation oncology, biology, physics*, 42(1):213, 1998.

[18] CW Hurkmans, P Remeijer, JV Lebesque, and BJ Mijnheer. Set-up verification using portal imaging; review of current clinical practice. *Radiotherapy and Oncology*, 58(2):105–120, 2001.

[19] CS Ross, DH Hussey, EC Pennington, W Stanford, and DJ Fred. Analysis of movement of intrathoracic neoplasms using ultrafast computerized tomography. *International Journal of Radiation Oncology* Biology* Physics*, 18(3):671–677, 1990.

[20] JC Roeske, JD Forman, CF Mesina, T He, CA Pelizzari, E Fontenla, S Vijayakumar, GT Chen, et al. Evaluation of changes in the size and location of the prostate, seminal vesicles, bladder, and rectum during a course of external beam radiation therapy. *International journal of radiation oncology, biology, physics*, 33(5):1321, 1995.

[21] CJ Beard, P Kijewski, M Bussire, R Gelman, D Gladstone, K Shaffer, M Plunkett, P Castello, CN Coleman, et al. Analysis of prostate and seminal vesicle motion: implications for treatment planning. *International journal of radiation oncology, biology, physics*, 34(2):451, 1996.

[22] JA Antolak, II Rosen, CH Childress, GK Zagars, and A Pollack. Prostate target volume variations during a course of radiotherapy. *International Journal of Radiation Oncology* Biology* Physics*, 42(3):661–672, 1998.

[23] CL Creutzberg, VGM Althof, M de Hoog, AG Visser, H Huizenga, A Wijnmaalen, and PC Levendag. A quality control study of the accuracy of patient positioning in irradiation of pelvic fields. *International Journal of Radiation Oncology* Biology* Physics*, 34(3):697–708, 1996.

[24] J Hanley, MA Lumley, GS Mageras, J Sun, MJ Zelefsky, SA Leibel, Z Fuks, and GJ Kutcher. Measurement of patient positioning errors in three-dimensional conformal radiotherapy of the prostate. *International Journal of Radiation Oncology* Biology* Physics*, 37(2):435–444, 1997.

[25] D Yan, J Wong, F Vicini, J Michalski, C Pan, A Frazier, E Horwitz, A Martinez, et al. Adaptive modification of treatment planning to minimize the deleterious effects of treatment setup errors. *International journal of radiation oncology, biology, physics*, 38(1):197, 1997.

[26] C Weltens, K Kesteloot, G Vandevelde, and W Van den Bogaert. Comparison of plastic and orfit masks for patient head fixation during radiotherapy: Precision and costs. *International Journal of Radiation Oncology* Biology* Physics*, 33(2):499–507, 1995.

[27] GJ Kutcher, GS Mageras, and SA Leibel. Control, correction, and modeling of setup errors and organ motion. In *Seminars in radiation oncology*, volume 5, pages 134–145. Elsevier, 1995.

[28] GS Mageras, GJ Kutcher, SA Leibel, MJ Zelefsky, E Melian, R Mohan, and Z Fuks. A method of incorporating organ motion uncertainties into three-dimensional conformal treatment plans. *International Journal of Radiation Oncology* Biology* Physics*, 35(2):333–342, 1996.

[29] AE Lujan, EW Larsen, JM Balter, and RK Ten Haken. A method for incorporating organ motion due to breathing into 3d dose calculations. *Medical physics*, 26:715, 1999.

[30] WA Beckham, PJ Keall, and JV Siebers. A fluence-convolution method to calculate radiation therapy dose distributions that incorporate random set-up error. *Physics in medicine and biology*, 47(19):3465, 2002.

[31] G Ozyigit, T Yang, and KSC Chao. Intensity-modulated radiation therapy for head and neck cancer. *Current treatment options in oncology*, 5(1):3–9, 2004.

[32] A Eisbruch. Clinical aspects of imrt for head-and-neck cancer. *Medical dosimetry: official journal of the American Association of Medical Dosimetrists*, 27(2):99, 2002.

[33] A Eisbruch. Intensity-modulated radiotherapy of head-and-neck cancer: encouraging early results. *International journal of radiation oncology, biology, physics*, 53(1):1–3, 2002.

[34] JA Pengaricano and N Papanikolaou. Intensity-modulated radiotherapy for carcinoma of the head and neck. *Current oncology reports*, 5(2):131–139, 2003.

[35] MW Munter, C Thilmann, H Hof, B Didinger, B Rhein, S Nill, W Schlegel, M Wannenmacher, and J Debus. Stereotactic intensity modulated radiation therapy and inverse treatment planning for tumors of the head and neck region: clinical implementation of the step and shoot approach and first clinical results. *Radiotherapy and oncology*, 66(3):313–321, 2003.

[36] J Debus, D Zierhut, B Didinger, W Schlegel, and M Wannenmacher. Inverse planning and intensity-modulated radiotherapy in patients with prostate cancer. *Frontiers of radiation therapy and oncology*, 36:25–34, 2002.

[37] MJ Zelefsky, Z Fuks, and SA Leibel. Intensity-modulated radiation therapy for prostate cancer. In *Seminars in radiation oncology*, volume 12, pages 229–237. Elsevier, 2002.

[38] T. Bortfeld, K. Jokivarsi, M. Goitein, J. H. Kung, , and S. Jiang. Effect of intrafractioon motion on imrt dose delivery: statistical analysis and simulation. *Phys. Med. Biol.*, 47:2203–2220, 2002.

[39] S. Jiang, C. Pope, K. M. Al Jarrah, J. H. Kung, T. Bortfeld, , and T. Y. Chen. An experimental investigation on intra-fractional organ motion effects in lung imrt treatments. *Phys. Med. Biol.*, 48:17731784, 2003.

[40] CS Chui, E Yorke, and L Hong. The effects of intra-fraction organ motion on the delivery of intensity-modulated field with a multileaf collimator. *Med. Phys.*, 30:17361746, 2003.

[41] M Schaefer, MW Minter, C Thilmann, F Sterzing, P Haering, SE Combs, and J Debus. Influence of intra-fractional breathing movement in step-and-shoot imrt. *Phys. Med. Biol.*, 49:N175–N179, 2004.

[42] J Duan, S Shen, JB Fiveash, AR Popple, and IA Brezovich. Dosimetric and radiobiological impact of dose fractionation on respiratory motion induced imrt delivery errors: A volumetric dose measurement study. *Med.Phys*, 33:1380–1387, 2006.

[43] S Vedam, A Docef, M Fix, M Murphy, and P Keall. Dosimetric impact of geometric errors due to respiratory motion prediction on dynamic multileaf collimator-based four-dimensional radiation delivery. *Medical physics*, 32:1607, 2005.

[44] GD Hugo, N Agazaryan, and TD Solberg. The effects of tumor motion on planning and delivery of respiratory-gated imrt. *Medical physics*, 30:1052, 2003.

[45] SB Jiang, C Pope, KM Al Jarrah, JH Kung, T Bortfeld, and GTY Chen. An experimental investigation on intra-fractional organ motion effects in lung imrt treatments. *Physics in medicine and biology*, 48(12):1773, 2003.

[46] PJ Keall, GS Mageras, JM Balter, RS Emery, KM Forster, SB Jiang, JM Kapatoes, DA Low, MJ Murphy, BR Murray, et al. The management of respiratory motion in radiation oncology report of aapm task group 76. *Medical physics*, 33:3874, 2006.

[47] A Bel, M Van Herk, JV Lebesque, et al. Target margins for random geometrical treatment uncertainties in conformal radiotherapy. *Medical physics*, 23(9):1537, 1996.

[48] JA Antolak and II Rosen. Planning target volumes for radiotherapy: How much margin is needed? *International Journal of Radiation Oncology* Biology* Physics*, 44(5):1165–1170, 1999.

[49] AL McKenzie, M van Herk, and B Mijnheer. The width of margins in radiotherapy treatment plans. *Physics in medicine and biology*, 45(11):3331, 2000.

[50] BC Parker, AS Shiu, MH Maor, FF Lang, HH Liu, RA White, and JA Antolak. Ptv margin determination in conformal srt of intracranial lesions. *Journal of Applied Clinical Medical Physics*, 3(3):176–189, 2002.

[51] JC Stroom, HC de Boer, H Huizenga, and AG Visser. Inclusion of geometrical uncertainties in radiotherapy treatment planning by means of coverage probability. *Int. J. Radiat. Oncol. Biol., Phys.*, 43:905, 1999.

[52] M Van Herk, P Remeijer, and JV Lebesque. Inclusion of geometric uncertainties in treatment plan evaluation. *Int. J. Radiat. Oncol. Biol., Phys.*, 52:1407, 2002.

[53] M Van Herk, M Witte, J van der Geer, C Schneider, and JV Lebesque. Biologic and physical fractionation effects of random geometric errors. *Int J Radiat Oncol Biol Phys.*, 57:1460, 2003.

[54] JY Jin, FM Kong, D Liu, L Ren, H Li, H Zhong, B Movsas, and IJ Chetty. A tcp model incorporating setup uncertainty and tumour cell density variation in microscopic extension to guide treatment planning. *Med Phys*, 38:439, 2011.

[55] The Royal College of Radiologist. On target: ensuring geometric accuracy in radiotherapy. Technical report, Institute of Physics and Engineering in Medicine, 2008.

[56] A Brahme. Dosimetric precision requirements in radiation therapy. *Acta Oncologica*, 23(5):379–391, 1984.

[57] J Nymana, J Karl-Axel, and H Ulla. Stereotactic hypofractionated radiotherapy for stage-1 non-small cell lung cancer: Mature results for medically inoperable patients. *Lung Cancer*, 51:97–103, 2006.

[58] KS Chao, AI Blanco, and JF Dempsey. A conceptual model integrating spatial information to assess target volume coverage for imrt treatment planning. *International Journal of Radiation Oncology* Biology* Physics*, 56(5):1438–1449, 2003.

[59] R Holland, SHJ Veling, M Mravunac, and JHCL Hendriks. Histologic multifocality of tis, t1–2 breast carcinomas implications for clinical trials of breast-conserving surgery. *Cancer*, 56(5):979–990, 2006.

[60] JY Jin, M Ajlouni, Q Chen, FMS Kong, S Ryu, and B Movsas. Quantification of incidental dose to potential clinical target volume (ctv) under different stereotactic body radiation therapy (sbrt) techniques for non-small cell lung cancer–tumor motion and using internal target volume (itv) could improve dose distribution in ctv. *Radiotherapy and Oncology*, 85(2):267–276, 2007.

[61] L Zhao, M Chen, RT Haken, I Chetty, O Chapet, JA Hayman, and FM Kong. Three-dimensional conformal radiation may deliver considerable dose of incidental nodal irradiation in patients with early stage node-negative non-small cell lung cancer when the tumor is large and centrally located. *Radiotherapy and oncology*, 82(2):153–159, 2007.

[62] HR Withers, LJ Peters, JM Taylor, et al. Dose-response relationship for radiation therapy of subclinical disease. *International journal of radiation oncology, biology, physics*, 31(2):353, 1995.

[63] J van Loon, C Siedschlag, J Stroom, H Blauwgeers, S van Robert-Jan, J Knegjens, M Rossi, A van Baardwijk, L Boersma, H Klomp, et al. Microscopic disease extension in three dimensions for non-small-cell lung cancer: Development of a prediction model using pathology-validated positron emission tomography and computed tomography features. *Int. J. Radiat. Oncol. Biol., Phys.*, 82(1):448–456, 2012.

[64] C Siedschlag, L Boersma, J van Loon, M Rossi, A van Baardwijk, K Gilhuijs, and J Stroom. The impact of microscopic disease on the tumor control probability in non-small-cell lung cancer. *Radiotherapy and Oncology*, 100(3):344–350, 2011.

[65] MG Witte, WD Heemsbergen, R Bohoslavsky, FJ Pos, A Al-Mamgani, JV Lebesque, and M van Herk. Relating dose outside the prostate with freedom from failure in the dutch trial 68 gy vs. 78 gy. *Int J Radiat Oncol Biol Phys*, 77(1):131–138, 2010.

[66] JF Fowler. The linear quadratic formula and progress in fractionated radiotherapy. *Br. J. Radiol.,*, 62:679–694, 1989.

[67] JD Chapman. The single-hit mechanism of tumor cell killing by radiation. *Int. J. Radiat. Biol*, 79:71–81, 2003.

[68] G Steel. *Basic clinical radiobiology for radiation oncologists, chapter 10*. Arnold, London, 2002.

[69] A Niemierko and M Goitein. Implementation of a model for estimating tumor control probability for an inhomogeneously irradiated tumor. *Radiother Oncol*, 29:140–147, 1993.

[70] S Webb and AE Nahum. A model for calculating tumour control probability in radiotherapy including the effects of inhomogeneous distributions of dose and clonogenic cell density. *Phys Med Biol*, 38:653–666, 1993.

[71] B Sanchez-Nieto B and AE Nahum. The delta-tcp concept: A clinically useful measure of tumour control probability,. *Int. J. Radiat. Oncol. Biol. Phys.,*, 44,:369, 1999.

[72] R Morrison. The results of treatment of cancer of the bladder-a clinical contribution to radiobiology. *Clin. Radiol.*, 26:67–75, 1975.

[73] JJ Batterman, AAM Hart, and K Breur. Dose-effect relations for tumour control and complication rate after fast neutron therapy for pelvic tumours. *Br. J. Radiol.*, 54:899–904, 1981.

[74] JV Moore, JH Hendry, and RD Hunter. Dose incidence curves for tumor control and normal tissue injury in relation to the response of clonogenic cells. *Radiother. Oncol.*, 1:143–157, 1983.

[75] G Hanks, KL Martz, and JJ Diamond. The effect of dose on local control of prostate cancer,. *Int. J. Radiat. Oncol.Biol. Phys.*, 15:1299–1305, 1988.

[76] RG Stock, NN Stone, A Tabert, C Iannuzzi, and JK DeWyngaert. A dose-response study for i-125 prostate implants. *Int. J. Radiat. Oncol. Biol. Phys.*,, 41:101–108, 1998.

[77] MK Martel, T Haken, RK Hazuka, MB Kessler, and ML Strawderman et al. Estimation of tumor control probability parameters from 3-d dose distributions of non-small cell lung cancer patients. *Lung Cancer*, 24:31–37, 1999.

[78] R Jacob, AL Hanlon, EM Horwitz, B Movsas, RG Uzzo, and A Pollack. Role of prostate dose escalation in patients with greater than 15risk of pelvic lymph node involvement,. *Int. J. Radiat. Oncol. Biol. Phys.*, 61:695–701, 2005.

[79] GK Zagars, TE Schultheiss, and LJ Peters. Inter-tumour heterogeneity and radiation dose-control curves. *Radiother. Oncol.*, 8:353–362, 1987.

[80] RJ Yaes. The slope of the sigmoid dose response curve for tumor control. *Int. J. Radiat. Oncol. Biol. Phys.*, 44:470–471, 1999.

[81] J Deacon, MJ Peckham, and GG Steel. The radioresponsiveness of human tumours and the initial slope of the cell survival curve,. *Radiother.Oncol.*, 2,:317–323, 1984.

[82] AL Boyer and T Schultheiss. Effects of dosimetric and clinical uncertainty on complication-free local tumor control. *Radiother. Oncol.*, 11:65–71, 1988.

[83] J Dutreix, M Tubiana, and A Dutreix. An approach to the interpretation of clinical data on the tumour control probability-dose relationship. *Radiother. Oncol.*, 11:239–248, 1988.

[84] T Bortfeld and H Paganetti. The biologic relevance of daily dose variations in adaptive treatment planning. *Int J Radiat Oncol Biol Phys*, 65:899, 2006.

[85] DJ Brenner and EJ Hall. Fractionation and protraction for radiotherapy of prostate carcinoma. *International Journal of Radiation Oncology* Biology* Physics*, 43(5):1095–1101, 1999.

[86] DJ Brenner, A Martinez, GK Edmundson, C Mitchell, HD Thames, and EP Armour. Direct evidence that prostate tumors show high sensitivity to fractionation (low α/β ratio), similar to late-responding normal tissue. *International Journal of Radiation Oncology* Biology* Physics*, 52(1):6–13, 2002.

[87] K Hausterman and JF Fowler. A comment on proliferation rates in human prostate cancer. *International journal of radiation oncology, biology, physics*, 48(1):303–303, 2000.

[88] JZ Wang, M Guerrero, and A Li. How low is the α/β ratio for prostate cancer? *International Journal of Radiation Oncology* Biology* Physics*, 55(1):194–203, 2003.

[89] J Blanchette and M Summerfield. *C++ gui programming with qt 4, second edition.* Prentice Hall Press Upper Saddle River, NJ, USA, 2008.

[90] M Mathieu. *GDCM Reference Manual*, first edition, 2008.

[91] W Schroeder, KM Martin, and WE Lorensen. *The visualization toolkit (2nd ed.): an object-oriented approach to 3D graphics.* Prentice-Hall, Inc. Upper Saddle River, NJ, USA, 1998.

[92] BJR Supplement25. Central axis depth dose data for use in radiotherapy. Technical report, Joint working party of the British Institute of Radiology and the Hospital Physicists. Association, London: British Institute of Radiology., 1996.

[93] J Bijhold, VL Joos, AA Hart, and RE Vijlbrief. Maximizing setup accuracy using portal images as applied to a conformal boost technique for prostatic cancer. *Radiother Oncol.*, 24:261, 1992.

[94] M Van Herk, P Remeijer, C Rasch, and JV Lebesque. The probability of correct target dosage: dose-population histograms for deriving treatment margins in radiotherapy. *Int J Radiat Oncol Biol Phys*, 47:1121, 2000.

[95] T Craig, J Battista, V Moiseenko, and J Van Dyk. Considerations for the implementation of target volume protocols in radiotherapy. *Int J Radiat Oncol Biol Phys.*, 49:241, 2001.

[96] BC Cho, M van Herk, BJ Mijnheer, and H Bartelink. The effect of set-up uncertainties, contour changes and tissue inhomogeneities on target dose-volume histograms. *Med Phys.*, 29:2305, 2002.

[97] SD McCarter and WA Beckham. Evaluation of the validity of a convolution method for incorporating tumour movement and set-up variations into the radiotherapy treatment planning system. *Phy Med Biol.*, 45:923, 2000.

[98] AE Lujan, EW Larsen, JM Balter, and RK Ten Haken. A method for incorporating organ motion due to breathing into 3d dose calculations. *Med Phys.*, 26:715, 1999.

[99] M Van Herk. Errors and margins in radiotherapy. *Semin. Radiat. Oncol.*, 14:52, 2004.

[100] W Song, J Battista, and J Van Dyk. Limitations of a convolution method for modeling geometric uncertainties in radiation therapy: the radiobiological dose-per-fraction effect. *Med Phys.*, 31:3034, 2004.

[101] J Leong. Implementation of random positioning error in computerised radiation treatment planning systems as a result of fractionation. *Phy Med Biol*, 32:327, 1987.

[102] JF Fowler, RJ Chappell, and MA Ritter. The prospects for new treatments for prostate cancer. *Int J Radiat Oncol Biol Phys.*, 52:3, 2002.

[103] DJ Brenner and EJ Hall. Fractionation and protraction for radio-therapy of prostate carcinoma. *Int J Radiat Oncol Biol Phys.*, 43:1095, 1999.

[104] AE Nahum, J Uzan, P Jain, ZI Malik, JD Fenwick, and C Baker. Quantitative tumour control predictions for the radiotherapy of non-small-cell lung tumours. *Med Phys*, 38:3641, 2011.

[105] JO de Xivry, P Castadot, G Janssens, JA Lee, X Geets, V Grgoire, and B Macq. Evaluation of the radiobiological impact of anatomic modifications during radiation therapy for head and neck cancer: Can we simply summate the dose? *Radiother Oncol.*, 96:131, 2010.

[106] J Stroom, A Schlief, T Alderliesten, H Peterse, H Bartelink, and K Gilhuijs. Using histopathology breast cancer data to reduce clinical target volume margins at radiotherapy. *Int J Radiat Oncol Biol Phys.*, 74:898, 2009.

[107] IS Grills, DL Fitch, N Goldstein, DC Yan, GW Chmielewski, RJ Welsh, and LL Kestin. Clinicopathologic analysis of microscopic extension in lung adenocarcinoma: De?ning clinical target volume for radiotherapy. *Int J Radiat Oncol Biol Phys.*, 69:334, 2007.

[108] KK Chao et al. Clinicopathologic analysis of extracapsular extension in prostate cancer: Should the clinical target volume be expanded posterolaterally to account for microscopic extension? *Int J Radiat Oncol Biol Phys.*, 65:999, 2006.

[109] S Apisarnthanarax. Determining optimal clinical target volume margins in head-and-neck cancer based on microscopic extracapsular extension of metastatic neck nodes. *Int J Radiat Oncol Biol Phys*, 64:678, 2006.

[110] M Goitein and TE Schultheiss. Strategies for treating possible tumour extension: some theoretical considerations. *Int J Radiat Oncol Biol Phys.*, 11:1519, 1985.

[111] K Yoda and K Nakagawa. Extension of van herk's treatment margin model for anisotropic systematic positioning errors in cartesian coordinate system. *Med Phys.*, 38:3913, 2011.

[112] C Baker, M Chandrasekaran, J Uzan, and A Nahum. Tumour control probability demands parameters consistent with the treatment planning dose algorithm. *Radiother Oncol.*, 103:S362, 2012.

[113] MS Hoffman, S Gunesakaran, H Arango, S DeCesare, JV Fiorica, M Parsons, and D Cavanagh. Lateral microscopic extension of squamous cell carcinoma of the vulva. *Gynecologic oncology*, 73(1):72–75, 1999.

[114] CF Njeh. Tumor delineation: The weakest link in the search for accuracy in radiotherapy. *Journal of medical physics/Association of Medical Physicists of India*, 33(4):136, 2008.

[115] WD Heemsbergen, A Al-Mamgani, MG Witte, M van Herk, and JV Lebesque. Radiotherapy with rectangular fields is associated with fewer clinical failures than conformal fields in the high-risk prostate cancer subgroup: Results from a randomized trial. *Radiotherapy and Oncology*, 107:134–139, 2013.

[116] M Van Herk. Will igrt live up to its promise? *Acta Oncologica*, 47(7):1186–1187, 2008.

[117] Y Seppenwoolde, H Shirato, K Kitamura, S Shimizu, M van Herk, J Lebesque, and K Miyasaka. Precise and real-time measurement of 3d tumor motion in lung due to breathing and heartbeat, measured during radiotherapy. *International Journal of Radiation Oncology* Biology* Physics*, 53(4):822–834, 2002.

[118] SS Vedam, VR Kini, PJ Keall, V Ramakrishnan, H Mostafavi, and R Mohan. Quantifying the predictability of diaphragm motion during respiration with a noninvasive external marker. *Medical physics*, 30:505, 2003.

[119] T Neicu, H Shirato, Y Seppenwoolde, and SB Jiang. Synchronized moving aperture radiation therapy (smart): average tumour trajectory for lung patients. *Physics in medicine and biology*, 48(5):587, 2003.

[120] R George, SS Vedam, TD Chung, V Ramakrishnan, and PJ Keall. The application of the sinusoidal model to lung cancer patient respiratory motion. *Medical physics*, 32:2850, 2005.

[121] VR Kini, SS Vedam, PJ Keall, S Patil, C Chen, and R Mohan. Patient training in respiratory-gated radiotherapy. *Medical Dosimetry*, 28(1):7–11, 2003.

[122] CW Stevens, RF Munden, KM Forster, JF Kelly, Z Liao, G Starkschall, S Tucker, and R Komaki. Respiratory-driven lung tumor motion is independent of tumor size, tumor location, and pulmonary function. *International Journal of Radiation Oncology* Biology* Physics*, 51(1):62–68, 2001.

[123] I Suramo, M Paivansalo, and V Myllyla. Cranio-caudal movements of the liver, pancreas and kidneys in respiration. *Acta radiologica: diagnosis*, 25(2):129, 1984.

[124] SC Davies, AL Hill, RB Holmes, M Halliwell, and PC Jackson. Ultrasound quantitation of respiratory organ motion in the upper abdomen. *British Journal of Radiology*, 67(803):1096–1102, 1994.

[125] PJ Bryan, S Custar, JR Haaga, and V Balsara. Respiratory movement of the pancreas: an ultrasonic study. *Journal of Ultrasound in Medicine*, 3(7):317–320, 1984.

[126] J Hanley, MM Debois, D Mah, GS Mageras, A Raben, K Rosenzweig, B Mychalczak, HL Schwartz, PJ Gloeggler, W Lutz, et al. Deep inspiration breath-hold technique for lung tumors: the potential value of target immobilization and reduced lung density in dose escalation. *International Journal of Radiation Oncology* Biology* Physics*, 45(3):603–611, 1999.

[127] S Shimizu, H Shirato, K Kagei, T Nishioka, X Bo, H Dosaka-Akita, S Hashimoto, H Aoyama, K Tsuchiya, and K Miyasaka. Impact of respiratory movement on the computed tomographic images of small lung tumors in three-dimensional (3d) radiotherapy. *International Journal of Radiation Oncology* Biology* Physics*, 46(5):1127–1133, 2000.

[128] P Giruad, Y De Rycke, B Dubray, S Helfre, D Voican, L Guo, JK Rosenwald, K Keraudy, M Housset, E Touboul, et al. Conformal radiotherapy (crt) planning for lung cancer: analysis of intrathoracic organ motion during extreme phases of breathing. *International Journal of Radiation Oncology* Biology* Physics*, 51(4):1081–1092, 2001.

[129] C Plathow, S Ley, C Fink, M Puderbach, W Hosch, A Schmahl, J Debus, and H Kauczor. Analysis of intrathoracic tumor mobility during whole breathing cycle by dynamic mri. *International Journal of Radiation Oncology* Biology* Physics*, 59(4):952–959, 2004.

[130] Q Chen, MS Weinhous, FC Deibel, JP Ciezki, and RM Macklis. Fluoroscopic study of tumor motion due to breathing: facilitating precise radiation therapy for lung cancer patients. *Medical physics*, 28:1850, 2001.

[131] EA Barnes, BR Murray, DM Robinson an LJ Underwood, J Hanson, and HY Wilson. Dosimetric evaluation of lung tumor immobilization using breath hold at

deep inspiration. *International Journal of Radiation Oncology* Biology* Physics*, 50(4):1091–1098, 2001.

[132] S Shimizu, H Shirato, S Ogura, H Akita-Dosaka, K Kitamura, T Nishioka, K Kagei, M Nishimura, and K Miyasaka. Detection of lung tumor movement in real-time tumor-tracking radiotherapy. *International Journal of Radiation Oncology* Biology* Physics*, 51(2):304–310, 2001.

[133] MJ Murphy, D Martin, R Whyte, J Hai, C Ozhasoglu, and Q Le. The effectiveness of breath-holding to stabilize lung and pancreas tumors during radiosurgery. *International Journal of Radiation Oncology* Biology* Physics*, 53(2):475–482, 2002.

[134] KE Sixel, M Ruschin, R Tirona, and CF Patrick. Digital fluoroscopy to quantify lung tumor motion: potential for patient-specific planning target volumes. *International Journal of Radiation Oncology* Biology* Physics*, 57(3):717–723, 2003.

[135] IS Grills, Y Di, A Martinez, FA Vicini, JW Wong, and LL Kestin. Potential for reduced toxicity and dose escalation in the treatment of inoperable non–small-cell lung cancer: A comparison of intensity-modulated radiation therapy (imrt), 3d conformal radiation, and elective nodal irradiation. *International Journal of Radiation Oncology* Biology* Physics*, 57(3):875–890, 2003.

[136] SC Erridge, Y Seppenwoolde, SH Muller, M van Herk, K De Jaeger, J Belderbos, JL Boersma, and JV Lebesque. Portal imaging to assess set-up errors, tumor motion and tumor shrinkage during conformal radiotherapy of non-small cell lung cancer. *Radiotherapy and oncology*, 66(1):75–85, 2003.

[137] Y Seppenwoolde, H Shirato, K Kitamura, and et al. Precise and real-time measurement of 3d tumor motion in lung due to breathing and heartbeat, measured during radiotherapy. *Int J Radiat Oncol Biol Phys*, 53:822–834, 2002.

[138] NCH Choi and JA Doucette. Improved survival of patients with unresectable non-small-cell bronchogenic carcinoma by an innovated high-dose en-bloc radiotherapeutic approach. *Cancer*, 48(1):101–109, 2006.

[139] M Mehta, R Scrimger, R Mackie, B Paliwal, R Chappell, and J Fowler. A new approach to dose escalation in non–small-cell lung cancer. *International Journal of Radiation Oncology* Biology* Physics*, 49(1):23–33, 2001.

[140] Intensity Modulated Radiation Therapy CollaborativeWorking Group. Intensity-modulated radiotherapy: current status and issues of interest. *Int. J. Radiat. Oncol. Biol. Phys.*, 51:880–914, 2001.

[141] FJ Lagerwaard, CJA Haasbeek, EF Smit, BJ Slotman, and S Senan. Outcomes of risk-adapted fractionated stereotactic radiotherapy for stage i non–small-cell lung cancer. *International Journal of Radiation Oncology* Biology* Physics*, 70(3):685–692, 2008.

[142] RD Timmerman, BD Kavanagh, LC Cho, L Papiez, and L Xing. Stereotactic body radiation therapy in multiple organ sites. *Journal of clinical oncology*, 25(8):947–952, 2007.

[143] J Wulf, K Baier, G Mueller, and MP Flentje. Dose-response in stereotactic irradiation of lung tumors. *Radiotherapy and oncology*, 77(1):83–87, 2005.

[144] XY Cedric, DA Jaffray, and JW Wong. The effects of intra-fraction organ motion on the delivery of dynamic intensity modulation. *Physics in medicine and biology*, 43(1):91, 1999.

[145] HD Kubo and BC Hill. Respiration gated radiotherapy treatment: a technical study. *Phys. Med. Biol.*, 41:8391, 1996.

[146] PJ Keall, VR Kini, SS Vedam, and R Mohan. Motion adaptive x-ray therapy: a feasibility study. *Phys. Med.Biol.*, 46:110, 2001.

[147] H Shirato et al. Physical aspects of a realtime tumor-tracking system for gated radiotherapy. *Int. J. Radiat. Oncol.Biol. Phys.*, 48:1187–95, 2000.

[148] A Schweikard, G Glosser, M Bodduluri, MJ Murphy, and JR Adler. Robotic motion compensation for respiratory movement during radiosurgery. *Comput. Aided Surg.*, 5:263–77, 2000.

[149] RI Berbeco, CJ Pope, and SB Jiang. Measurement of the interplay effect in lung imrt treatment using edr2 films. *Journal of Applied Clinical Medical Physics*, 7(4):33–42, 2006.

[150] B Zhao, Y Yang, T Li, X Li, DE Heron, and MS Huq. Dosimetric effect of intrafraction tumor motion in phase gated lung stereotactic body radiotherapy. *Medical physics*, 39(11):6629, 2012.

[151] J Seco, GC Sharp, J Turcotte, D Gierga, T Bortfeld, and H Paganetti. Effects of organ motion on imrt treatments with segments of few monitor units. *Medical physics*, 34(3):923, 2007.

[152] A Niemierko. Quality assurance and validation of individual imrt treatment plans before delivery. *Medical Physics*, 31:421, 2004.

[153] Y Yang, L Xing, JG Li, J Palta, Y Chen, G Luxton, and A Boyer. Independent dosimetric calculation with inclusion of head scatter and mlc transmission for imrt. *Med.Phys.*, 30:2937–2947, 2003.

[154] RL Siddon. Fast calculation of the exact radiological path for a three-dimensional ct array. *Med Phys*, 12:252–255, 1985.

[155] D Yan and D Lockman. Organ/patient geometric variation in external beam radiotherapy and its effects. *Med. Phys*, 28:593602, 2001.

[156] M Rao, J Wu, D Cao, J Ye, F Chen, T Wong, V Mehta, and D Shepard. Mo-d-brb-02: Investigation of the interplay effect between field segments and tumor motion during vmat and imrt delivery. *Medical Physics*, 37:3339, 2010.

[157] O Chinloon, FAR Wilko, PC Cuijpers, BJ Slotman, and S Senan. Dosimetric impact of interplay effect on rapidarc lung stereotactic treatment delivery. *Int. J. Radiat. Oncol. Biol., Phys.*, 79:305–311, 2011.

[158] L Court, M Wagar, M Bogdanov, D Ionascu, D Schofield, A Allan, R Berbeco, and T Lingos. Use of reduced dose rate when treating moving tumors using dynamic imrt. *Journal of Applied Clinical Medical Physics*, 12(1):28–34, 2011.

[159] C Ozhasoglu and MJ Murphy. Issues in respiratory motion compensation during external-beam radiotherapy. *Int. J. Radiat. Oncol. Biol. Phys.*, 52:1389–99, 2002.